

**NEW APPROACHES TO CHALCOGENIDE MATERIALS FOR  
THERMOELECTRICS: LEAD TELLURIDE-BASED NANOSTRUCTURES AND  
FACILE SYNTHESIS OF TETRAHEDRITE AND DOPED DERIVATIVES**

by

**DERAK JAMES**

**DISSERTATION**

Submitted to the Graduate School

of Wayne State University,

Detroit, Michigan

in partial fulfillment of the requirements

for the degree of

**DOCTOR OF PHILOSOPHY**

2015

MAJOR: CHEMISTRY (Inorganic)

Approved by:

---

Advisor

Date

---

---

---

---

ProQuest Number: 3735125

All rights reserved

INFORMATION TO ALL USERS

The quality of this reproduction is dependent upon the quality of the copy submitted.

In the unlikely event that the author did not send a complete manuscript and there are missing pages, these will be noted. Also, if material had to be removed, a note will indicate the deletion.



ProQuest 3735125

Published by ProQuest LLC (2015). Copyright of the Dissertation is held by the Author.

All rights reserved.

This work is protected against unauthorized copying under Title 17, United States Code  
Microform Edition © ProQuest LLC.

ProQuest LLC.  
789 East Eisenhower Parkway  
P.O. Box 1346  
Ann Arbor, MI 48106 - 1346

## **DEDICATION**

To my family, who have been a continual source of inspiration and support.

## **ACKNOWLEDGEMENTS**

This work would not be possible without my advisor, Dr. Stephanie Brock. She not only exemplifies scholarship as a scientist, but stands out for her ability to multi-task, managing the various students and projects in her research group with great insight and expertise. Beyond her depth and breadth of knowledge, her passion for research leads her to always look a little bit deeper, questioning results and findings to explore any subject for new insights. Her analytical abilities are paired with professionalism and interpersonal skills. She treats her students as people first, focusing on their development as independent scientists and guiding them towards their individual goals. As a mentor, she defines herself as an educator first, patiently prioritizing the professional development of her students as members of the scientific community above the need to just publish. Looking back on my experiences and accomplishments under her leadership, I am filled with gratitude and pride.

I would like to thank my committee members Dr. Claudio Verani, for always being there as someone to talk to as well as for his thoughtful insights, Dr. H. Bernhard Schlegel, for bringing such a positive attitude and disposition along with his unique perspective, and Dr. Zhixian Zhou for his questions and educating me in his excellent material and device characterizations class. These professors have made time in their hectic schedules to help me graduate, and I thank them. I owe a debt of gratitude to my collaborators, Dr. Xu Lu and Dr. Donald Morelli for not only testing my materials, but the feedback on our results and thoughtful discussion of our work. Dr. Xu Lu introduced me to thermoelectric characterization methods and had me practicing solid state methods at Dr. Morelli's laboratory at MSU. Dr. Morelli applies a wealth of information and experience to the field of thermoelectric materials, and we started to develop a solvothermal route to tetrahedrite at his request.

I offer my thanks to Dr. Mary Frances Barber and Melissa Barton, who ran orientation for me at Wayne State University. They taught me how to teach, and I thank Dr. Barber and Dr. Barbara Monk for the opportunity to be a teaching assistant under them. Melissa Barton wears many hats in helping the graduate students keep ahead of administrative requirements and deadlines throughout their time at Wayne State; she really is a star.

Thank you to all my fellow group members, current and past. From when I first started here, Dr. Shreyashi Ganguly taught me hot-injection solution-phase synthesis. She introduced me to the techniques in the lab, and taught me that graduate school is a marathon, not a sprint. She was always happy to help, and gave me the tools to survive here. Dr. Layan Savithra was a good friend, always happy to talk in or out of the lab. Dr. Lasantha Korala acted as a sounding board for many of my ideas, as I liked to talk out the problems in research and possible solutions to them. Dr. Irina Pala was always cheerful and looking for ways the group could get together for fun. She really took on a leadership role in holding the group together. Dr. Yanhua Zhang was our shutterbug, always taking pictures and always with a positive attitude. My current group members, Roshini Pimmachcharige, Ruchira Liyanage, Jessica Davis, Da Li, Indika Hewavitharana, Malsha Hettiarachchi, and Samuel Mutinda, are great coworkers with diverse backgrounds that make for lively discussions and cross-application of skills. Roshini took classes with me from the beginning of my career here, and Ruchira is a friendly and lively lab mate to work next to. Jessica takes it upon herself to set up group activities outside of the lab. Da is always enthusiastic, making friends with everyone and keeping me laughing. Our newer members, Indika and Malsha, are independent and professional. They always have a smile for anyone that talks to them. Samuel, who joined last year, is one of the most driven people I have worked with in graduate school. He reminds me of when I first started here, in a race with

himself to see how quickly he can publish, and he is truly interested in people, learning everything he can about the people he meets. Thank you also to my undergraduate students Alexander Chi Nguyen and Michael Gelfetto. Alex was a joy to work with due to his refreshing enthusiasm to learn. This really gave me a desire to teach him the syntheses and characterization techniques used in my research and keep the project moving so that I always had something new to demonstrate and then have him do. Michael Gelfetto actually came to work on his own ideas and brought a spirit of invention to the lab. Helping him find ways to work around snags in his research challenged me to think broadly and creatively.

Many thanks to all of my past chemistry teachers for feeding my interest and my imagination in visualizing the behavior of matter on the atomic level. First, I would like to thank my former advisor, Dr. Tykhon Zubkov, for taking me as his first graduate student. He helped me make the transition from a college student studying under professors to being in graduate school, working with a professor. We worked together and independently in seeking solutions to the obstacles of research. Meanwhile, he nurtured my problem solving abilities and let me know how much he appreciated my efforts. This was a time of great adjustment and self-discovery for me as I left home to go to Ball State University for my Masters, and I thank the Garners at the college institute for lending an ear when I was nervous, feeling under pressure, or just needed someone to talk to. The comradery with the other students there was like a little bit of home away from home. In addition, I would like to thank Dr. Anita Gnezda, whom I had the pleasure of teaching lab under at Ball State. Many thanks to Dr. Beatriz Cisneros for being my course advisor at Purdue University and running the chemistry resource center there. She tirelessly strives to get students the tools they need to succeed. I would like to thank Dr. Dor Ben Amotz at Purdue University for his physical chemistry class exploring various models of the atom. I

especially thank my first chemistry teacher, Mr. Fitzgerald at Southwestern Middle School, for introducing me to the Bohr model and teaching me to think of matter in terms of electron interactions. By the time I got to high school, I knew that I wanted to be a chemist.

Thank you to the many talented educators I have had the privilege of studying under, and those individuals who have helped me along this journey. In particular, I would like to thank my English teacher Mrs. Paula Wilson at McCutcheon High School for her passion for civil and human rights issues around the world. I further thank her for the eye-opening trip she put together to Italy; it introduced me to a whole world outside of high school. Many thanks to the football program and Coach Shoemaker of the wrestling team at Southwestern Middle School. School sports offered outlets for me, as an introspective kid, to break out of my shell, make new friends, and, sometimes, even get to be a star. Thank you to Coach Kevin O'Shea of my high school football team who always treated me as a valued member, even though my peers seemed to outgrow me, and made arrangements for me to still pursue my passion in music without giving up football. I would like to thank my high school band director, John McCutcheon, for convincing me to take a leadership role in the marching band. Making music was and continues to be a source of great joy in my life, especially when I can share it with others. I would also like to thank my friend Tim here in Detroit. He made sure that I got out of the lab from time to time to see the fun side of the city, cheered me up when I research was slowed, and bragged about me to everyone we met.

Most of all, I thank my parents. My father seems to have passed on to me his analytical mind. This has been a gift to me for use in all of the sciences. I also thank my father for always being eager to spend time with me. I remember the camping and canoeing trips that we went on, and how he took me to work with him. He taught me that when someone needs help for

something they cannot do themselves, and if I can help them, then I should just do it. I know that he is proud of me, and that always meant a lot. I also know that he can relate to me on how challenging graduate school can be. I thank my mother for always believing in me, as far back as I can remember, even when I did not. She just knew that I was capable of great things. I remember that she respected my need to understand why things were the way they were, and would patiently explain to me the reason behind anything she told me to do. She taught me that I could do anything that I put my mind to, it was only a matter of time and effort. She pushed me to go outside of my comfort zone, try new things, and become well-rounded by getting involved in team and social activities. My mother always led by example, working hard so that she could get my brother and I what we needed and spending her free time with us. Her desire for me was always that I would find happiness and fulfillment in life through use of my full potential, and not to sell myself short.

Here is to my next step in this journey, but it is important to take to a moment from time to time to look back at how far I have come. One thing that life has taught me is that persistence is the key to success.

## TABLE OF CONTENTS

Dedication .....	ii
Acknowledgements.....	iii
List of Tables .....	ix
List of Figures .....	x
Chapter 1 Introduction and Thesis Statements .....	1
Chapter 2 Experimental .....	28
Chapter 3 Design of Lead Telluride Based Thermoelectric Materials Through Incorporation of Lead Sulfide Inclusions or Ligand Stripping of Nano-Sized Building Blocks.....	44
Chapter 4 Solvothermal Synthesis of Tetrahedrite: Speeding Up the Process of Thermoelectric Material Generation .....	65
Chapter 5 Tuning the Thermoelectric Properties of Solvothermal Tetrahedrite by Doping In-Situ with Zinc .....	89
Chapter 6 Conclusions and Prospectus .....	113
References.....	127
Abstract.....	140
Biosketch.....	143

## LIST OF TABLES

Table 3.1 Scherrer sizes of lead telluride and lead sulfide crystallites after annealing (a) or hot-pressing (hp), as determined by XRD. Samples include lead telluride that has been iodide stripped (PbTe-I), sulfur stripped (PbTe-S), consecutively sulfur and iodide stripped (PbTe-SI), mixed with lead sulfide (PbTe-PbS), or washed with methanol (PbTe). The sulfur and iodine mole fraction values relative to lead are determined by inductively coupled plasma optical emission spectroscopy (ICP-OES). ....	50
Table 3.2 Average iodine mole percentage for interparticle and intraparticle regions of TEM micrographs of PbTe-I after annealing along with the standard deviations and 95% confidence intervals of the measurements.....	52
Table 3.3 Thermoelectric properties of the hot-pressed samples at room temperature. ....	58
Table 4.1 Room temperature thermoelectric properties determined for solid state tetrahedrite (Solid State), the solid state tetrahedrite mixed with NM (Solid State + NM), the solvothermal tetrahedrite synthesized with 100% molar excess thiourea (Tet.100), the solvothermal tetrahedrite synthesized with 100% molar excess thiourea and mixed with NM (Tet.100 + NM), and the solvothermal tetrahedrite prepared by literature methods alone (Lit. Prep.) and mixed in a 1:1 molar ratio with NM (Lit. + NM) are displayed for comparison.	80
Table 4.2 Compositions of many tetrahedrite products from the solvothermal synthesis with 300% molar excess thiourea as determined by ICP-OES. Mole equivalents of Sb and Cu are scaled to 13 mole equivalents of sulfur. The tetrahedrite products are combined and the weighted average of Sb moles and Cu moles are listed below, along with the mass of the combined samples.....	83
Table 5.1 Compositions for many products from the solvothermal synthesis for production of the $x = 0.79$ zinc-doped tetrahedrite are determined by ICP-MS. Mole equivalents of Sb and Cu are scaled assuming 13 mole equivalents of sulfur. The tetrahedrite products are combined and the weighted average of Cu, Zn, and Sb moles are listed below along with the mass of the combined samples.....	98
Table 5.2 Compositions for many products from the solvothermal synthesis for production of the $x = 1.15$ zinc-doped tetrahedrite are determined by ICP-MS. Mole equivalents of Sb and Cu are scaled assuming 13 mole equivalents of sulfur. The tetrahedrite products are combined and the weighted average of Sb moles and Cu moles are listed below along with the mass of the combined samples.....	99
Table 5.3 Compositions for many products from the solvothermal synthesis for production of the $x = 1.40$ zinc-doped tetrahedrite are determined by ICP-MS. Mole equivalents of Sb and Cu are scaled assuming 13 mole equivalents of sulfur. The tetrahedrite products are combined and the weighted average of Sb moles and Cu moles are listed below along with the mass of the combined samples.....	100

## LIST OF FIGURES

Figure 1.1 Electrons (dark blue) at the hot end of an <i>n</i> -type semiconductor excite to the conductance band by absorption of heat ( $h\nu$ ), resulting in the hole and excited electron, $h^+$ and $e^*$ , respectively, which travel toward the cold end at different rates. ....	2
Figure 1.2 ZT values at operation temperatures for traditional thermoelectric materials $\text{CsBi}_4\text{Te}_6$ , $\text{Bi}_2\text{Te}_3$ , $\text{PbTe}$ , $\text{AgSbTe}_2$ , and $(\text{AgSbTe}_2)_{1-x}(\text{GeTe})_x$ .....	3
Figure 1.4 The solvent-stabilized, surfactant capped PbTe nanoparticle is illustrated. Dangling bonds of lead cations on the surface are passivated by a long chain surfactant, like oleate, and the nonpolar end of the surfactant is solubilized by the long chain solvent. The R and R' are generic carbon chains. ....	11
Figure 1.5 The P=E bond is inserted between the lead and an oleate (Scheme 1). Oleic acid transfers a proton to the electrophile (Scheme 2). ....	13
Figure 1.3 Lattice thermal conductivity and electrical conductivity at 642 K are plotted versus mol% of lead sulfide.....	15
Figure 1.6 Two approaches for PbTe based nanocomposites are displayed. Oleic acid capped PbTe NCs are mixed with oleic acid capped PbS by incipient wetness (Top). Methanol and heat are used consecutively to strip the oleic acid ligands and remove the solvent, resulting in PbTe–PbS. Alternatively, ammonium sulfide $(\text{NH}_4)_2\text{S}$ in methanol is used to strip the ligand, reacting with lead cations on the surface to result in a film of lead sulfide. Heating removes elemental sulfur to result in PbTe NCs held together by PbS at the interfaces. ....	17
Figure 1.7 The unit cell <sup>74</sup> (a) of tetrahedrite, Inorganic Crystal Structure Database code 41753, projected parallel to a triangular plane formed by a Cu atom (blue) with three S atoms (yellow) is displayed. A rectangle is added to point out a region of the cell containing an arrangement of two trigonal pyramidal Sb atoms (brown) above and below the trigonal planar Cu. The unit cell is displayed again in the same orientation (b) for clarity after hiding all atoms not included in this arrangement of two trigonal pyramidal Sb atoms above and below the trigonal planar Cu. ....	18
Figure 1.8 Spin-resolved electronic DOS for $U=0$ of $\text{Cu}_{11.0}\text{TM}_{1.0}\text{Sb}_4\text{S}_{13}$ (TM=Mn (a), Fe (b), Co (c), Ni (d), and Zn (e)). The red area describes the partial DOS for TM. Reprinted with permission from Suekuni, K.; Tomizawa, Y.; Ozaki, T.; Koyano, M., Systematic Study of Electronic and Magnetic Properties for $\text{Cu}_{12-x}\text{TM}_x\text{Sb}_4\text{S}_{13}$ (TM = Mn, Fe, Co, Ni, and Zn) Tetrahedrite. <i>J. Appl. Phys.</i> 2014, <b>115</b> (14), 143702. Copyright 2014, AIP Publishing LLC. ....	25
Figure 2.1 A simple diagram of inner shell electrons (K shell, L shell, and M shell) in an atom. An electron from the electron gun ionizes a K shell electron, and an electron from the L shell relaxes via emission of an X-ray.....	33

Figure 2.2 Interaction of X-rays of $\lambda$ wavelength with a parallel set of planes with lattice spacing $d$ by two different paths and incident angle $\theta$ .....	34
Figure 2.3 A parallelepiped with an area at the end of A and a length of L .....	38
Figure 2.4 The schematic setup for measuring electronic properties of the parallelepiped is displayed. Electrodes for applying current ( $I^+$ and $I^-$ ) and the voltage ( $V^+$ and $V^-$ ) by the four probe method are labeled. Thermocouples are attached at each end. A resistor is used to apply heat.....	40
Figure 3.1 (a) XRD data for lead telluride NCs. Silicon is present as an internal standard. The reference pattern for PbTe is shown (red lines), and the peak indices and $d$ -spacings are indicated. (b) TEM micrograph of lead telluride nanoparticles. The inset shows the presumed 1–2 nm lead oleate clusters. ....	47
Figure 3.2 TEM micrograph of lead sulfide NCs as prepared and dispersed in hexane. The composition of the group of NCs was determined by EDS and is displayed as atomic percentages. ....	49
Figure 3.3 XRD patterns of the iodide stripped (PbTe-I), sulfide stripped (PbTe-S), sulfide and then iodide stripped (PbTe-SI), lead sulfide mixed with lead telluride (PbTe–PbS), and methanol-washed lead telluride (PbTe) samples after annealing shown along with the Powder Diffraction File (PDF) patterns for silicon (internal standard, 27–1402), lead sulfide (78–1057, also indicated by arrows) and lead telluride (77–0246). ....	51
Figure 3.4 TEM micrographs of lead telluride nanoparticles after iodide stripping (PbTe-I) before (a) and after (b) annealing. Compositions, as atomic percentages, are displayed in the insets. ....	51
Figure 3.5 TEM micrographs of the sulfide stripped lead telluride NCs (PbTe-S) before annealing (a), and after annealing (b). EDS results for the images are displayed alongside as atomic percent. Moiré fringes are evident in panel a (circled particles) due to interference patterns from two different lattice dimensions (presumably PbS over PbTe). ....	53
Figure 3.6 TEM micrograph of lead telluride nanoparticles stripped first with sulfide and then with iodide (PbTe-SI) before annealing (a) and after annealing (b). The compositions determined for the images by EDS are displayed as atomic percentages. ....	54
Figure 3.7 TEM micrograph of mixed lead sulfide and lead telluride NCs (PbTe–PbS) after annealing. The EDS-determined compositions of two regions are displayed as atomic percentages. ....	55
Figure 3.8 TEM micrograph of the control sample of methanol-washed lead telluride NCs (PbTe) after annealing .....	55
Figure 3.9 XRD spectra of the iodide stripped (PbTe-I), sulfide stripped (PbTe-S), sulfide, then iodide stripped (PbTe-SI), and methanol stripped (PbTe) lead telluride as well as lead sulfide	

NCs mixed with lead telluride NCs (PbTe–PbS) samples after hot-pressing are shown along with the PDF files 27–1402 for silicon, 78–1057 for lead sulfide (arrows), and 77–0246 for lead telluride. ....	56
Figure 3.10 Temperature-dependent Seebeck coefficient (a) and electrical conductivity (b) values of hot-pressed samples. ....	59
Figure 3.11 Thermal conductivity (a) and lattice thermal conductivity (b) values near room temperature plotted as a function of temperature for the sulfide stripped sample (PbTe-S hp), the sulfide and iodide stripped sample (PbTe-SI hp), the control (PbTe hp), the iodide stripped sample (PbTe-I hp), and the composite of mixed lead sulfide and lead telluride nanoparticles (PbTe–PbS hp). The data point at 290 K for PbTe-S and PbTe–PbS is removed because of a common fluctuation that occurs from melting of small ice crystals in the cryostat.....	61
Figure 3.12 Thermoelectric Figure of Merit, ZT, values as a function of temperature. ....	63
Figure 4.1 XRD patterns of tetrahedrite synthesized by the reported literature method before ( $\text{Cu}_{15.8}\text{Sb}_{7.8}\text{S}_{13}$ ) and after hot-pressing ( $\text{Cu}_{15.8}\text{Sb}_{7.8}\text{S}_{13}$ hp). PDF patterns 42–0561 and 35–0581 are displayed for tetrahedrite ( $\text{Cu}_{12}\text{Sb}_4\text{S}_{13}$ ) and famatinite ( $\text{Cu}_3\text{SbS}_4$ ), respectively. The literature-prepared tetrahedrite is ball-milled in a 1:1 molar ratio with the natural mineral tennantite, $\text{Cu}_{10}\text{Zn}_{1.8}\text{Fe}_{0.2}\text{As}_{2.7}\text{Sb}_{1.3}\text{S}_{13}$ , and hot pressed to produce $\text{Cu}_{15.8}\text{Sb}_{7.8}\text{S}_{13} + \text{NM}$ hp. ....	68
Figure 4.2 TEM images of different regions of literature-prepared tetrahedrite revealing different compositions by EDS a) $\text{Cu}_{13.2}\text{Sb}_{4.6}\text{S}_{13}\text{Cl}_{0.8}$ b) $\text{Cu}_{2.0}\text{S}_{0.8}$ .....	69
Figure 4.3 The temperature-dependent Seebeck coefficient (a) and resistivity (b) values are displayed for the hot-pressed samples. These include the solvothermal tetrahedrite prepared by literature methods (Lit. Prep.), the solvothermal tetrahedrite mixed in a 1:1 molar ratio with the natural mineral tennantite, $\text{Cu}_{10}\text{Zn}_{1.8}\text{Fe}_{0.2}\text{As}_{2.7}\text{Sb}_{1.3}\text{S}_{13}$ (Lit. + NM), and the solid state tetrahedrite (Solid State).....	70
Figure 4.4 Temperature-dependent thermal conductivity (a) and Figure of Merit, ZT (b) values of the hot-pressed samples. These include the solvothermal tetrahedrite prepared by literature methods (Lit. Prep.), the solvothermal tetrahedrite mixed in a 1:1 molar ratio with the natural mineral tennantite, $\text{Cu}_{10}\text{Zn}_{1.8}\text{Fe}_{0.2}\text{As}_{2.7}\text{Sb}_{1.3}\text{S}_{13}$ (Lit. + NM), and the solid state tetrahedrite (Solid State).....	71
Figure 4.5 XRD pattern of the solvothermal tetrahedrite product synthesized with a stoichiometric ratio of reagents is displayed. The reference patterns, PDF 05-0534, PDF 42–0561, and PDF 44-1417 are displayed for antimony(III) oxide ( $\text{Sb}_2\text{O}_3$ ), tetrahedrite ( $\text{Cu}_{12}\text{Sb}_4\text{S}_{13}$ ), and chalcostibite ( $\text{CuSbS}_2$ ), respectively. The * marks the locations of prominent chalcostibite peaks, and the # marks locations of prominent $\text{Sb}_2\text{O}_3$ peaks that do not overlap with peaks from tetrahedrite.....	74

Figure 4.6 XRD patterns of the solvothermal tetrahedrite product synthesized with 100% molar excess of thiourea before and after treatment with sulfuric acid. The reference patterns, PDF 05-0534, PDF 42-0561, and PDF 44-1417 are displayed for antimony(III) oxide ( $\text{Sb}_2\text{O}_3$ ), tetrahedrite ( $\text{Cu}_{12}\text{Sb}_4\text{S}_{13}$ ), and chalcostibite ( $\text{CuSbS}_2$ ). The \* marks locations of prominent  $\text{CuSbS}_2$  peaks that do not overlap with peaks from tetrahedrite. ..... 75

Figure 4.7 XRD patterns of the solvothermal tetrahedrite product synthesized with 100% molar excess of thiourea before and after treatment with sulfuric acid. The reference patterns, PDF 05-0534, PDF 42-0561, and PDF 44-1417 are displayed for antimony(III) oxide ( $\text{Sb}_2\text{O}_3$ ), tetrahedrite ( $\text{Cu}_{12}\text{Sb}_4\text{S}_{13}$ ), and chalcostibite ( $\text{CuSbS}_2$ ). The # marks locations of prominent  $\text{Sb}_2\text{O}_3$  peaks that do not overlap with peaks from tetrahedrite. ..... 76

Figure 4.8 XRD spectra of several solvothermal tetrahedrite products synthesized with 100% molar excess thiourea. The pattern PDF 44-1417 for chalcostibite ( $\text{CuSbS}_2$ ) is shown for reference. The arrows mark locations of prominent  $\text{CuSbS}_2$  peaks that do not overlap with peaks from tetrahedrite or famatinite..... 77

Figure 4.9 XRD patterns from solvothermal tetrahedrite synthesized with 100% molar excess thiourea (Tet.100) before and after hot-pressing as well as after ball-milling with NM and hot-pressing. Reference patterns for tetrahedrite ( $\text{Cu}_{12}\text{Sb}_4\text{S}_{13}$ ), PDF 42-0561, and chalcostibite ( $\text{CuSbS}_2$ ), PDF 44-1417, are displayed below the data plots and \* marks observed peaks due to chalcostibite..... 78

Figure 4.10 Thermoelectric properties determined from 80 K to 300 K are displayed for solid state tetrahedrite (Solid State), solvothermal tetrahedrite synthesized with 100% molar excess thiourea (Tet.100), and the solvothermal tetrahedrite synthesized with 100% molar excess thiourea and mixed with NM (Tet.100 + NM). Properties displayed include a) Resistivity, b) Thermopower, c) Thermal Conductivity, and d) Figure of Merit..... 79

Figure 4.11 Expanded views of the XRD patterns from several runs of the solvothermal synthesis with 300% molar excess sulfur source are displayed along with their compositions as determined by ICP-OES. The pattern for chalcostibite ( $\text{CuSbS}_2$ ) is shown for reference. The arrows mark locations of where the prominent  $\text{CuSbS}_2$  peaks that do not overlap with peaks from tetrahedrite or famatinite would be expected to be..... 81

Figure 4.12 XRD patterns for the tetrahedrite product from several runs of the solvothermal synthesis using 300% molar excess of sulfur precursor. Reference PDF patterns 42-0561 and 35-0581 are displayed for tetrahedrite ( $\text{Cu}_{12}\text{Sb}_4\text{S}_{13}$ ) and famatinite ( $\text{Cu}_3\text{SbS}_4$ ), respectively. The ICP-OES determined composition, normalized to S = 13, is displayed for each product. The \* marks observed peaks for famatinite. ..... 82

Figure 4.13 XRD patterns from the solvothermal tetrahedrite synthesized with 300% molar excess thiourea before (Tetrahedrite) and after (Tet. hp) hot-pressing as well as the tetrahedrite ball-milled with NM and hot-pressed (Tet. + NM hp). Reference PDF patterns 42-0561 and 35-0581 are displayed for tetrahedrite ( $\text{Cu}_{12}\text{Sb}_4\text{S}_{13}$ ) and famatinite ( $\text{Cu}_3\text{SbS}_4$ ), respectively. The \* marks observed peaks for famatinite. ..... 84

Figure 4.14 Temperature-dependent Seebeck coefficient (a) and resistivity (b) values from room temperature to 720 K plotted as a function of temperature for the solid state tetrahedrite (Solid State), the solvothermal tetrahedrite synthesized with 300% molar excess thiourea (Tetrahedrite), the solvothermal tetrahedrite mixed with natural mineral (Tet. + NM), and the solid state tetrahedrite mixed with NM (Solid State + NM). All samples were hot-pressed .....	85
Figure 4.15 Thermal conductivity (a) and ZT (b) values from room temperature to 720 K plotted as a function of temperature for the solid state tetrahedrite (Solid State), the solvothermal tetrahedrite synthesized with 300% molar excess thiourea (Tetrahedrite), the solvothermal tetrahedrite mixed with natural mineral (Tet. + NM), and the solid state tetrahedrite mixed with NM (Solid State + NM).....	86
Figure 5.1 XRD pattern for the tetrahedrite product from several runs of the solvothermal synthesis. Reference patterns 42–0561 and 35–0581 are displayed for tetrahedrite ( $\text{Cu}_{12}\text{Sb}_4\text{S}_{13}$ ) and famatinite ( $\text{Cu}_3\text{SbS}_4$ ), respectively. The ICP-MS determined composition, normalized to S = 13, is displayed for each product. ....	93
Figure 5.2 XRD pattern for the tetrahedrite product from several runs of the solvothermal synthesis. Reference patterns 42–0561 and 35–0581 are displayed for tetrahedrite ( $\text{Cu}_{12}\text{Sb}_4\text{S}_{13}$ ) and famatinite ( $\text{Cu}_3\text{SbS}_4$ ), respectively. The ICP-MS determined composition, normalized to S = 13, is displayed for each product. ....	95
Figure 5.3 XRD pattern for the tetrahedrite product from several runs of the solvothermal synthesis. Reference patterns 42–0561 and 35–0581 are displayed for tetrahedrite ( $\text{Cu}_{12}\text{Sb}_4\text{S}_{13}$ ) and famatinite ( $\text{Cu}_3\text{SbS}_4$ ), respectively. The ICP-MS determined composition, normalized to S = 13, is displayed for each product. ....	97
Figure 5.4 XRD patterns for zinc-doped solvothermal tetrahedrite with composition $\text{Cu}_{10.16}\text{Zn}_{0.79}\text{Sb}_{3.99}\text{S}_{13}$ (from mass averaging the samples with compositions determined by ICP-MS and normalized to S=13) before and after hot-pressing. Reference patterns 42– 0561 and 35–0581 are displayed for tetrahedrite ( $\text{Cu}_{12}\text{Sb}_4\text{S}_{13}$ ), and famatinite, respectively. The ★ marks prominent famatinite peaks. ....	101
Figure 5.5 XRD patterns for zinc-doped solvothermal tetrahedrite with composition $\text{Cu}_{10.46}\text{Zn}_{1.15}\text{Sb}_{4.09}\text{S}_{13}$ (from mass averaging the samples with compositions determined by ICP-MS and normalized to S=13) before and after hot-pressing. Reference patterns 42– 0561 and 35–0581 are displayed for tetrahedrite ( $\text{Cu}_{12}\text{Sb}_4\text{S}_{13}$ ), and famatinite, respectively. The ★ marks prominent famatinite peaks. ....	102
Figure 5.6 XRD patterns for zinc-doped solvothermal tetrahedrite with composition $\text{Cu}_{10.99}\text{Zn}_{1.40}\text{Sb}_{4.01}\text{S}_{13}$ (from mass averaging the samples with compositions determined by ICP-MS and normalized to S=13) before and after hot-pressing. Reference patterns 42– 0561 and 35–0581 are displayed for tetrahedrite ( $\text{Cu}_{12}\text{Sb}_4\text{S}_{13}$ ), and famatinite, respectively. The ★ marks prominent famatinite peaks. ....	103

Figure 5.7 Expanded views are displayed for the XRD patterns for zinc-doped solvothermal tetrahedrite with composition Cu<sub>10.99</sub>Zn<sub>1.40</sub>Sb<sub>4.01</sub>S<sub>13</sub> (from mass averaging the samples with compositions determined by ICP-MS and normalized to S=13) before and after hot-pressing. The reference pattern 42–0561 for tetrahedrite (Cu<sub>12</sub>Sb<sub>4</sub>S<sub>13</sub>) is overlaid on each pattern. . 104

Figure 5.8 Temperature-dependent Seebeck coefficient (a) and resistivity (b) values from room temperature to 720 K plotted as a function of temperature for the solid state tetrahedrite (Solid State), the solvothermal tetrahedrite (Tetrahedrite), the solvothermal tetrahedrite mixed with natural mineral (Tet. + NM), the solid state tetrahedrite mixed with NM (Solid State + NM), and the zinc doped solvothermal tetrahedrite samples (compositions calculated from determinations by ICP-MS). All samples were hot-pressed..... 105

Figure 5.9 Temperature-dependent Power Factor ( $\alpha^2/\rho$ ) values from room temperature to 720 K plotted as a function of temperature for the solid state tetrahedrite (Solid State), the solvothermal tetrahedrite (Tetrahedrite), the solvothermal tetrahedrite mixed with natural mineral (Tet. + NM), the solid state tetrahedrite mixed with NM (Solid State + NM), and the zinc doped solvothermal tetrahedrite samples (compositions calculated from determinations by ICP-MS)..... 107

Figure 5.10 Temperature-dependent thermal conductivity values from room temperature to 720 K plotted as a function of temperature for the solid state tetrahedrite (Solid State), the solvothermal tetrahedrite (Tetrahedrite), the solvothermal tetrahedrite mixed with natural mineral (Tet. + NM), the solid state tetrahedrite mixed with NM (Solid State + NM), and the zinc doped solvothermal tetrahedrite samples (compositions calculated from determinations by ICP-MS)..... 108

Figure 5.11 Temperature-dependent thermoelectric figure of merit, ZT, values from room temperature to 720 K plotted as a function of temperature for the solid state tetrahedrite (Solid State), the solvothermal tetrahedrite (Tetrahedrite), the solvothermal tetrahedrite mixed with natural mineral (Tet. + NM), the solid state tetrahedrite mixed with NM (Solid State + NM), and the zinc doped solvothermal tetrahedrite samples (compositions calculated from determinations by ICP-MS) ..... 110

## CHAPTER 1 : INTRODUCTION AND THESIS STATEMENTS

### 1.1. THERMOELECTRICS

Thermoelectric materials salvage waste heat by converting it to electricity and therefore act as an environmentally friendly technology for energy efficiency. A majority of the energy generated in the United States is lost as heat, making waste heat plentiful and cheap.<sup>1</sup> However, the practicality of alternative energy has been limited by high cost in comparison to coal.<sup>1</sup> The roadblocks to widespread application of thermoelectric materials beyond niches such as space station generators are the lengthy and complex preparation of materials,<sup>2-9</sup> the expense, rarity, and toxicity of component materials,<sup>10-18</sup> and the low figure of merit, ZT.

Thermoelectric materials are inherently or intentionally doped as *p*-type or *n*-type. For *n*-type, as displayed in Figure 1.1, electrons are easily excited from an occupied energy level near the top of the band gap by heat (IR radiation,  $h\nu$ ) to provide excited electrons as charge carriers. These excited electrons,  $e^*$ , are accelerated from the hot end to the cold end by a temperature difference,  $\Delta T$ , resulting in a negative charge at the cold end and a voltage difference,  $\Delta V$ , across the length of the material. The voltage difference per temperature difference is known as the Seebeck Coefficient or thermopower,  $\alpha = -\Delta V/\Delta T$ . In *p*-type materials, electrons are excited to an available molecular orbital towards the bottom of the bandgap, resulting in holes,  $h^+$ , which are accelerated toward the cold end to result in a voltage difference with a difference in temperature. The thermopower,  $\alpha$ , electrical conductivity,  $\sigma$ , and thermal conductivity,  $\kappa_{tot}$ , along with the average temperature,  $T$ , determine ZT by the equation  $ZT = T\alpha^2\sigma/\kappa_{tot}$ . The factors  $\alpha$ ,  $\sigma$ , and  $\kappa_{tot}$  are interrelated, and the thermopower and electrical conductivity are often inversely related, making achievement of high ZT ( $\geq 1$ ) challenging. To further complicate matters, the

total thermal conductivity ( $\kappa_{\text{tot}}$ ) is the sum of electronic charge carrier ( $\kappa_C$ ) and lattice ( $\kappa_L$ ) contributions; so,  $\kappa_C$  increases with  $\sigma$  leading to increased  $\kappa_{\text{tot}}$ .

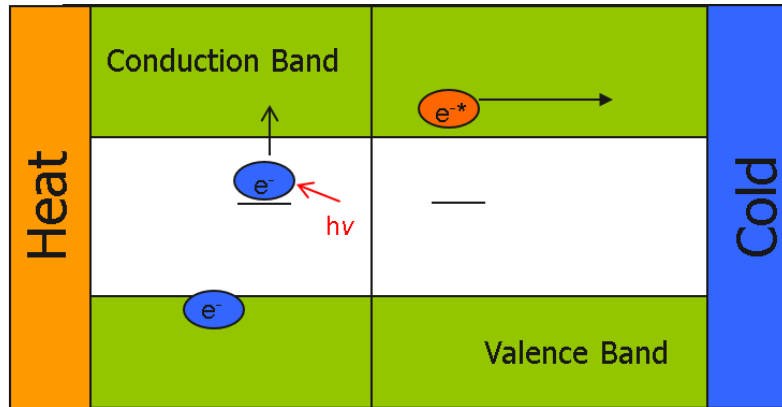


**Figure 1.1** Electrons (dark blue) at the hot end of an *n*-type semiconductor excite to the conductance band by absorption of heat ( $h\nu$ ), resulting in the hole and excited electron,  $h^+$  and  $e^*$ , respectively, which travel toward the cold end at different rates.

## 1.2. TRADITIONAL THERMOELECTRIC MATERIALS (BULK)

Traditional bulk thermoelectric materials are crystalline semiconductors with a bandgap that allows thermal excitation of electrons to generate the carriers.<sup>19</sup> The fact that they are crystalline allows transport of carriers; however, the semiconductor bandgap limits electrical conductivity in comparison to metals. This limits the electrical contribution to thermal conductivity ( $\kappa_C$ ). The  $\kappa_C$  is determined by the Wiedeman–Franz Law from the electrical conductivity as  $\kappa_C = L\sigma T$ , with  $L$  as the Lorenz number for degenerate semiconductors (generally  $2.45 \times 10^{-8}$  W ohm K<sup>-2</sup>) and  $T$  as temperature.<sup>19-20</sup> The bulk materials demonstrate low lattice thermal conductivities due to incorporation of heavy elements. This is consistent with the Keyes' equation, where  $\kappa_L$  is mainly limited by destructive interference of phonons, also referred to as phonon–phonon scattering:<sup>21</sup>

$$\kappa_L T = \frac{R^{3/2}}{3\gamma^2 \varepsilon^3 N_0^{1/3}} \frac{T_m^{3/2} \rho^{2/3}}{A^{7/6}}$$

In Keyes' equation,  $A$  is the mean atomic mass,  $R$  is the ideal gas constant,  $T_m$  is the melting point,  $\rho$  is the density,  $\gamma$  is the Grüneisen constant,  $\varepsilon$  is the fractional amplitude of the interatomic thermal vibration, and  $N_0$  is Avogadro's number. The  $\kappa_L$  decreases proportionally to  $A^{-7/6}$ , allowing heavy elements to decrease the thermal conductivity. This is why thermoelectric materials often rely on bismuth or lead cations and tellurium anions.

The compounds lead telluride ( $PbTe$ ), silver antimony telluride ( $AgSbTe_2$ ), alloys of  $AgSbTe_2$  with germanium telluride ( $(AgSbTe_2)_{1-x}(GeTe)_x$ ) or TAGS (tellurium-antimony-germanium-silver), and bismuth telluride based materials ( $Bi_2Te_3$  or  $CsBi_4Te_6$ ) are considered traditional thermoelectrics.<sup>19</sup> This series of materials exhibit optimized ZT values of 0.8 to 1.5 over a wide range of operating temperatures as displayed in Figure 1.2. Therefore, the thermoelectric material for an application can be chosen by matching the maximum ZT with the operating temperature.

### Traditional Thermoelectric Materials

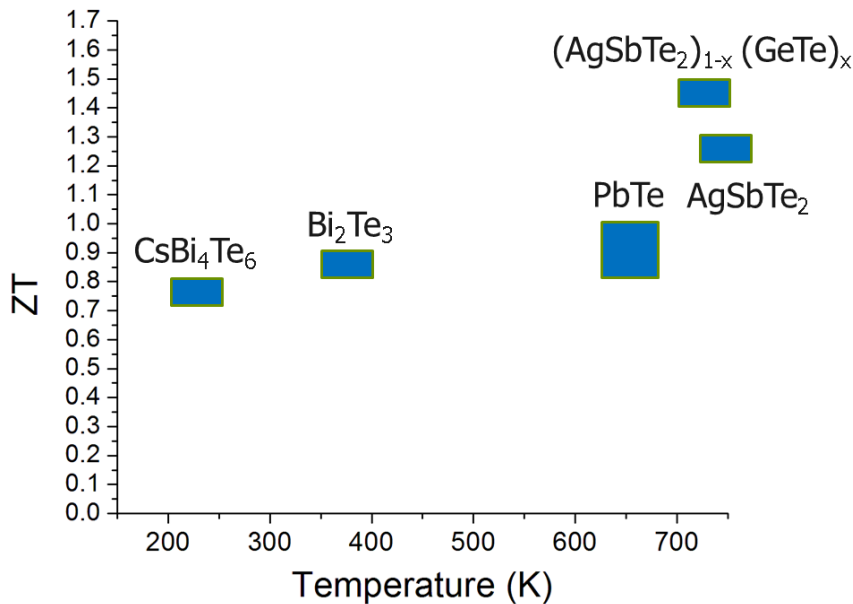


**Figure 1.2** ZT values at operation temperatures for traditional thermoelectric materials  $CsBi_4Te_6$ ,  $Bi_2Te_3$ ,  $PbTe$ ,  $AgSbTe_2$ , and  $(AgSbTe_2)_{1-x}(GeTe)_x$ .

Optimally doped bismuth telluride exhibits a ZT near unity at relatively low temperatures (~350–400 K). The pure, bulk material is a semiconductor with a narrow ( $E_g = 0.15$  eV) bandgap, and a rhombohedral crystal structure that results in layered planes held together by Van der Waals forces.<sup>22</sup> A ZT of 0.5 is achieved with a relatively low lattice thermal conductivity of  $2.4 \text{ W m}^{-1} \text{ K}^{-1}$  for pure  $\text{Bi}_2\text{Te}_3$ . The ZT is greatly increased to 0.9 by substitutional doping of antimony for bismuth ( $\text{Bi}_{2-x}\text{Sb}_x\text{Te}_3$ ,  $x=1.5$ ) due to a decrease in the thermal conductivity to  $1.5 \text{ W m}^{-1} \text{ K}^{-1}$ . The decreased thermal conductivity is caused by impurity scattering, where the antimony acts as a mass impurity to scatter phonons.<sup>19</sup> A similar ZT of 0.8 is obtained at even lower temperatures (225 K) for  $\text{CsBi}_4\text{Te}_6$ .<sup>23</sup> The material consists of  $\text{Cs}^+$  sandwiched between planes of  $\text{Bi}_4\text{Te}_6^-$ . The ability to perform at lower temperature than  $\text{Bi}_2\text{Te}_3$  stems from a much smaller bandgap of 0.08 eV due to the presence of unique  $\text{Bi}^{2+}$ – $\text{Bi}^{2+}$  bonds.

Bulk PbTe is a semiconductor ( $E_g = 0.32$  eV) with a rock salt structure like NaCl, and a ZT of ~0.4 (300 K). The larger bandgap of PbTe is consistent with a much higher optimal operating temperature (625–675 K) than demonstrated for  $\text{Bi}_2\text{Te}_3$ . The ZT increases to 0.8–1.0 at 650 K by *n*-type doping with iodide to increase the electrical conductivity.<sup>24–25</sup> The iodide doping results in occupied molecular orbitals in the bandgap from which electrons can be easily excited to the conduction band. This increases the power factor by increasing the electrical conductivity.<sup>10, 24–25</sup> High temperature performance is enhanced by a decrease in lattice thermal conductivity from  $2.2 \text{ W m}^{-1}\text{K}^{-1}$  at room temperature to  $1.1 \text{ W m}^{-1}\text{K}^{-1}$  at 650 K. The thermopower can be increased by incorporation of thallium while maintaining low lattice thermal conductivity to reach a ZT of 1.5 at 773 K.<sup>26</sup> Thus, the low lattice thermal conductivity acts as starting point, and optimization of the electronic properties can achieve increased ZT if the low thermal conductivity can be maintained.

Silver antimony telluride ( $\text{AgSbTe}_2$ ) exhibits a ZT as high as 1.3 at high temperature (720 K), but the thermoelectric properties vary with the method of sample preparation.<sup>27-28</sup>  $\text{AgSbTe}_2$  is a semiconductor with a bandgap varying from  $E_g = 0.2\text{--}0.6 \text{ eV}$ .<sup>29</sup> This variation stems from the site distribution of Ag and Sb.<sup>27</sup> The  $\text{Te}^{2-}$  forms a rock salt lattice like chloride in  $\text{NaCl}$ . The  $\text{Ag}^+$  and  $\text{Sb}^{3+}$  were thought to randomly occupy the octahedral voids like a solid solution. However, a structure with  $\text{Sb}^{3+}$  as the second nearest neighbor to another  $\text{Sb}^{3+}$ , (the nearest neighbor is  $\text{Te}^{2-}$ ,  $\text{Sb}-\text{Te}-\text{Sb}$ ), is less stable than a structure with  $\text{Ag}^+$  as the second nearest neighbor to  $\text{Sb}^{3+}$  ( $\text{Sb}-\text{Te}-\text{Ag}$ ). This leads to regions within the solid where the  $\text{Ag}^+$  and  $\text{Sb}^{3+}$  are ordered instead of random like a solid solution. The differing regions of order and disorder of  $\text{Sb}^{3+}$  and  $\text{Ag}^+$  are thought to lower the lattice thermal conductivity. Additionally, computational work predicts the presence of low frequency optical phonons that can interfere destructively with the acoustic phonons.<sup>30</sup> The combination of ordered and disordered domains in the same crystal lattice of  $\text{Te}^{2-}$ , as well as destructive interference between optical and acoustic phonons, lead to low lattice thermal conductivity.<sup>27, 30</sup>

TAGS are alloys between  $\text{AgSbTe}_2$  and  $\text{GeTe}$  ( $(\text{AgSbTe}_2)_{1-x}(\text{GeTe})_x$ ) and are also known as TAGS-*m*, with the *m* denoting the mole percentage of  $\text{GeTe}$ .<sup>31</sup> The  $\text{GeTe}$  is incorporated as a solid solution in the rock salt crystal structure above 510 K.<sup>32-33</sup> Incorporation of  $\text{GeTe}$  leads to *p*-type doping, increasing the ZT to 1.5 at 750 K for  $\text{GeTe}$ -rich compositions (*m*=80–85). TAGS-80 and TAGS-85 were among the first thermoelectric materials to achieve high ZT>1, and their performances are largely credited to extremely low lattice thermal conductivity (0.3 W m<sup>-1</sup> K<sup>-1</sup>). As early performers, these materials were employed by NASA for power generation in space.<sup>19</sup>

### 1.3. NANOSTRUCTURING TO IMPROVE ZT

Nanostructuring of various thermoelectric materials has been found to decrease lattice thermal conductivity resulting in an increase in ZT. The reduction in  $\kappa_L$  is thought to occur primarily through the mechanism of Rayleigh scattering, in which the phonon is considered a wave, and the fraction of waves scattered (Rayleigh scattering cross-section) is proportional to  $d^6/\lambda^4$ .<sup>34</sup> Here, the  $d$  is the diameter of the nanocrystalline impurity and the  $\lambda$  is the wavelength of the phonon. Therefore, the nanocrystalline impurities tend to scatter longer wavelength phonons in comparison to dopants (as mass impurities), which scatter short wavelength phonons.

Materials can be nanostructured as a result of superlattices formed by layers with alternating compositions or by incorporation of nanocrystalline impurities.<sup>34</sup> Superlattices can be prepared by bottom-up methods like chemical vapor deposition. Likewise, nanocrystalline impurities can be incorporated by top-down methods like ball-milling bulk materials followed by hot-pressing or precipitation of crystalline impurities from a melt of the elements. Alternatively, nanocrystals of different compounds can be prepared separately, followed by hot-pressing, as a bottom-up approach.

A variety of thermoelectric materials have been nanostructured by exploiting superlattices. For example, alternating layers of  $\text{Bi}_2\text{Te}_3/\text{Sb}_2\text{Te}_3$  were constructed by chemical vapor deposition to yield a very high ZT of 2.4 (300 K) due to a very low  $\kappa_L$  of  $0.22 \text{ W m}^{-1} \text{ K}^{-1}$  when measured perpendicular to the planes of  $\text{Bi}_2\text{Te}_3$ .<sup>35</sup> Similarly constructed periodic superlattices of  $\text{PbSe}_{.25}\text{Te}_{.75}$  and  $\text{PbTe}$  in alternating layers (55 Å period) decrease the  $\kappa_L$  by ~80% from  $2.2 \text{ W m}^{-1} \text{ K}^{-1}$  for bulk  $\text{PbTe}$  to  $0.5 \text{ W m}^{-1} \text{ K}^{-1}$  for a ZT of 1.75 (425 K).<sup>36</sup> Thus, the superlattice approach has been demonstrated for modification of traditional thermoelectric materials to lower thermal conductivity.

The effectiveness of the superlattice approach to nanostructuring has led to its exploitation in modifying phases with prohibitively high  $\kappa_L$ . The  $\text{Si}_{0.8}\text{Ge}_{0.2}$  alloy consists of abundant elements, but would normally not be considered for thermoelectrics due to a prohibitively high  $\kappa_L$  of  $\sim 5 \text{ W m}^{-1} \text{ K}^{-1}$  (300 K); however, layers of  $\text{Si}_{1-x-y}\text{Ge}_x\text{C}_y$  and Si alternate to form a periodic superlattice with a 3 nm period to lower  $\kappa_L$  by 40% to  $3 \text{ W m}^{-1} \text{ K}^{-1}$  (300 K).<sup>37-39</sup> The decrease in  $\kappa_L$  is due to lattice strain from the lattice mismatch of the layers.<sup>40</sup> Similarly, a superlattice of three monolayers of AlAs followed by 3 monolayers of GaAs leads to a  $\kappa_L$  of  $3.1 \text{ W m}^{-1} \text{ K}^{-1}$  (300 K) in  $\text{GaAs}/\text{Al}_x\text{Ga}_{1-x}\text{As}$ , representing a 75% decrease from the  $\kappa_L$  of  $\text{Al}_{0.5}\text{Ga}_{0.5}\text{As}$ .<sup>41-42</sup> These superlattices demonstrate an ability to greatly decrease  $\kappa_L$ , but the reported values are still high relative to traditional thermoelectric materials.

Ball-milling and hot-pressing bulk materials allows top-down production of nanostructured thermoelectrics nanostructured for decreased lattice thermal conductivity. This process can be used to increase the ZT of bulk *n*-type  $\text{Bi}_2\text{Te}_3$  from 1 to 1.2 at room temperature<sup>43</sup> and to increase the ZT of BiSbTe alloy to 1.4 at 373 K.<sup>44</sup> This technique also works on the Si/Ge alloy described above, increasing the ZT from 0.60 to 0.72 at high temperature (1000 K) by greatly decreasing the thermal conductivity.<sup>45</sup> As a different approach to preparing thermoelectrics composed of actual nanocrystals, mechanical alloying of powdered elements results in a polycrystalline alloy of  $\text{Ag}_{0.8}\text{Pb}_{18+x}\text{SbTe}_{20}$ . The crystallites are micron sized and contain 20 nm diameter precipitates inside. The lattice thermal conductivity is decreased to 30% of that of PbTe, resulting in a ZT of 1.5 (673 K).<sup>46</sup>

Thermoelectrics can be nanostructured with endotaxially embedded NCs through precipitation of NCs in a melt as a top-down method or molecular beam epitaxy as a bottom-up method. Molecular beam epitaxy was used to synthesize a nanodot superlattice of  $\text{PbTe}/\text{PbSe}$

that exhibits a 50% decrease in  $\kappa_L$  from that of bulk PbTe to  $\sim 1 \text{ W m}^{-1} \text{ K}^{-1}$  (300 K) and a power factor 25–35% lower than PbTe. The crystals share a rock salt lattice of anions with crystalline domains composed of either PbTe or PbSe due to the endotaxial growth.<sup>47–48</sup> Precipitation from a melt of elements is used to prepare nanostructured  $\text{AgPb}_m\text{SbTe}_{2+m}$  (LAST-*m*).<sup>49–50</sup> The precipitation occurs spontaneously upon cooling from a melt to form  $\text{AgSbTe}_2$  and PbTe rock salt crystals that are endotaxially embedded. They share an anion lattice, but lattice strain results from the joining of the two crystals because of their different lattice spacing. This decreases  $\kappa_L$  to 0.5–0.8  $\text{W m}^{-1} \text{ K}^{-1}$  (300 K) relative to 2.2  $\text{W m}^{-1} \text{ K}^{-1}$  for bulk PbTe. The variation LAST-18 achieves  $\sim 1.7$  at 700 K with  $\sim 0.4 \text{ W m}^{-1} \text{ K}^{-1}$ . Similarly, the *p*-type analog of LAST- *m*,  $\text{NaPb}_m\text{SbTe}_{2+m}$  (or SALT-*m*) is prepared from a melt of the elements, resulting in endotaxially embedded  $\text{NaSbTe}_2$  in PbTe, which decreases the  $\kappa_L$  to 0.5–0.8  $\text{W m}^{-1} \text{ K}^{-1}$  (300 K) due to lattice strain. A maximum ZT of 1.6 (675 K) is achieved for SALT-20 due to a low  $\kappa_L$  of 0.5  $\text{W m}^{-1} \text{ K}^{-1}$  and  $\kappa_{\text{tot}}$  of 0.85  $\text{W m}^{-1} \text{ K}^{-1}$ .<sup>51</sup> Embedding endotaxial NCs through precipitation from a melt has also been exploited in the nontraditional thermoelectric material  $\text{In}_{0.53}\text{Ga}_{0.47}\text{As}$ .<sup>52</sup> Precipitation of 2–4 nm ErAs crystallites decreases  $\kappa_L$  by 50% to 3  $\text{W m}^{-1} \text{ K}^{-1}$  (300 K) from the high thermal conductivity  $\text{In}_{0.53}\text{Ga}_{0.47}\text{As}$  alloy. Thus, this technique is robust for reducing the  $\kappa_L$  of thermoelectric materials for improved ZT.

Solution-phase synthesis of pre-grown crystallites has been used to introduce micro- and nanostructuring to PbTe. Sub-micron crystal domains have been introduced by growing 200–400 nm PbTe crystallites in aqueous solution without ligands, followed by hot-pressing to result in comparable ZT to state of the art bulk PbTe (ZT of 0.8 at 580 K) by pairing a decreased  $\kappa_{\text{tot}}$  ( $0.75 \text{ W m}^{-1} \text{ K}^{-1}$ ) with an electrical conductivity ( $\sim 210 \text{ S}\cdot\text{cm}^{-1}$ ) that is two thirds of the value for the pure bulk ( $300 \text{ S}\cdot\text{cm}^{-1}$ ).<sup>12–13</sup> Smaller (30 nm) NCs were employed to form a nanostructured

PbTe pellet after ligand stripping with phosphonic acid.<sup>6</sup> This results in oxidized grain boundaries that lead to enhanced thermopower ( $625 \mu\text{W cm}^{-1} \text{K}^{-2}$ ) and  $\kappa_{\text{tot}}$  ( $0.75 \text{ W m}^{-1} \text{ K}^{-1}$ ) at room temperature but low ZT (0.02) due to low electrical conductivity ( $1.3 \text{ S}\cdot\text{cm}^{-1}$ ). Electrical transport has been studied on thin films of ligand stripped PbTe nanostructures at room temperature. Electrical conductivity was increased two orders of magnitude for thin films of solution grown, ligand capped nanowires by ligand stripping with hydrazine ( $\sim 5 \text{ S}\cdot\text{cm}^{-1}$ )<sup>53</sup> or ethanol ( $1.3 \text{ S}\cdot\text{cm}^{-1}$ ).<sup>54</sup> A similar electrical conductivity ( $4.8 \text{ S}\cdot\text{cm}^{-1}$ ) was achieved for a composite thin film of PbTe and Ag<sub>2</sub>Te NCs after ligand stripping with hydrazine. NCs.<sup>55</sup> Although high thermopower values are demonstrated for the hydrazine-stripped ( $410 \mu\text{W cm}^{-1} \text{K}^{-2}$ )<sup>53</sup> and ethanol-stripped ( $628 \mu\text{W cm}^{-1} \text{K}^{-2}$ )<sup>54</sup> thin films, ZT values are not determined because thermal conductivity values are not measured. However, these studies reveal the importance of ligand removal from ligand-capped NCs. The ligands are electrically insulating, and removing them can greatly increase the electrical conductivity, but it remains low compared to bulk PbTe ( $300 \text{ S}\cdot\text{cm}^{-1}$ )<sup>12</sup> or pellets of sub-micron crystallites grown without ligands.<sup>13</sup>

#### **1.4. PREPARATION OF SEMICONDUCTOR METAL CHALCOGENIDE NANOCRYSTALS BY HOT-INJECTION METHODS IN SOLUTION**

The hot-injection method is used to limit the size of crystallites grown in solution.<sup>56</sup> In brief, an anion precursor is dissolved in a nonpolar organic solvent to prepare a solution. The metal precursor is an ionic salt. This is dissolved in the organic solvent with the help of a surfactant, also referred to as a capping ligand, to prepare a second solution. The surfactant molecule is often amphiphilic, exhibiting a polar head group to interact with the cation and a nonpolar tail to interact with the solvent. An excess of metal precursor is commonly used to prepare a concentrated solution to favor precipitation of the product as small nanocrystals. The

anion solution is quickly injected into the metal cation solution at the reaction temperature to nucleate the product nanocrystals, which quickly lowers the concentration of both anion and cation left in the solution for further growth of the nucleated nanocrystals.

Hot-injection synthesis can be broken down into four steps: Pre-nucleation, nucleation, growth, and annealing.<sup>56</sup> The pre-nucleation step consists of preparing the solubilized cation and anion solutions as described above, and quickly combining them at a temperature to form the monomer. The nucleation step requires the collision of several monomers to begin formation of the crystal lattice.<sup>56-57</sup> Small dimensions of the nucleated nanocrystal, 1–2 nm, result in a very small lattice enthalpy. The lattice enthalpy is the force that holds the nanocrystal together while the entropy from solvating atoms on the surface tears it apart. These competing forces establish an equilibrium between formation and dissolution of the crystal. The total Gibbs free energy,  $\Delta G_{TOT} = (4/3)\pi r^3 \Delta G_v + \Delta G_s$ , can be calculated for crystal formation based off of the radius,  $r$ , the volume dependent free energy of the crystal,  $\Delta G_v$ , which is negative, and the positive free energy at the surface  $\Delta G_s$ .<sup>56</sup> Below the critical radius,  $r_c$ ,  $\Delta G_{TOT}$  increases with  $r$ , and the crystal will dissolve again to form monomers. These monomers can either contribute to nucleating a new lattice, or join the surface of an existing nanocrystal as part of the growth stage. This process of unstable nanocrystals dissolving into monomers that serve to increase the size of existing nanocrystals is referred to as Ostwald ripening, and increases polydispersity. If the radius is larger than  $r_c$ ,  $\Delta G_{TOT}$  decreases with  $r$ , and the crystal will not dissolve.

The critical radius can be calculated from the interfacial tension between the crystal and the solution,  $\gamma$ , the density of the crystal,  $\rho$ , the Boltzmann constant,  $k$ , and the parameter  $S$ , as  $r_c = -2 \gamma / (\rho k T \ln S)$ .<sup>56</sup> The parameter  $S$  reflects the degree of oversaturation, and is equal to the product of the concentrations of Cd and Se precursors in the reaction divided by the

concentration that would be in equilibrium with a bulk crystal at the reaction temperature, T. Thus, starting with a supersaturated solution of one of the precursors is sufficient to increase S and favor smaller nanocrystals by decreasing  $r_c$ . Increasing the reaction temperature of the solution further decreases the crystallite size.<sup>58</sup> By stabilizing small crystallite sizes, reaction conditions prevent them from dissolving again, and the concentration of monomers available for the growth stage is greatly decreased.

Growth occurs as monomers join the surface of a nucleated nanocrystal. The existing crystal lattice serves as a template for the monomers to join, but is passivated by the surfactant and solubilized in the nonpolar solvent (Figure 1.3). When crystallites nucleate and first begin to grow, the concentration of monomer available near the surface of the crystal is beginning to decrease. At this early stage, the growth rate is determined by either the rate at which monomers add to the surface or the rate at which surfactant dissociates; the slower of these will be the rate determining step. Thus, the use of surfactants that bind strongly to cations on the particle surface can slow growth. Growth overlaps with the nucleation stage; so, the rates compete, and a slower growth rate will favor smaller crystallites.

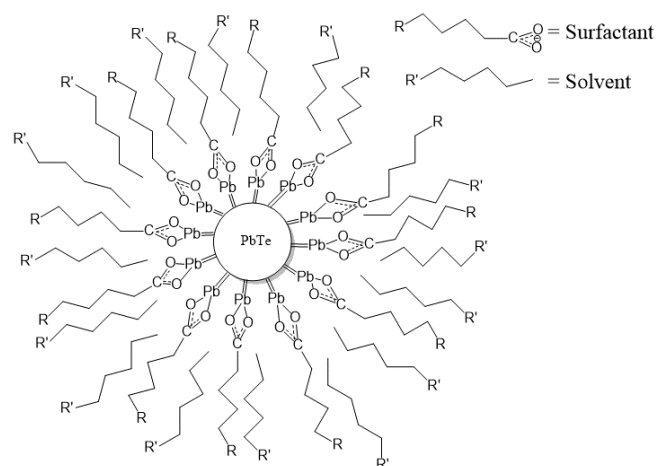


**Figure 1.3** The solvent-stabilized, surfactant capped  $\text{PbTe}$  nanoparticle is illustrated. Dangling bonds of lead cations on the surface are passivated by a long chain surfactant, like oleate, and the nonpolar end of the surfactant is solubilized by the long chain solvent. The  $\text{R}$  and  $\text{R}'$  are generic carbon chains.

The local concentration of monomers near the surface of nucleating and growing crystals quickly decreases, limiting the amount available for further growth. At this later stage, the growth rate depends on the rate of diffusion of monomers to the surface of the crystal. The diffusion rate of the monomer can be slowed by excess of one of the precursor ions, as well as the use of bulky surfactants. Employing an excess of a precursor also helps prevent the dissolution of small nanocrystals into new monomers that can be used for growth of another nanocrystal by Ostwald ripening. In addition, the diffusion rate can be decreased by lowering the temperature. The nanocrystals can then be annealed in solution at this lower temperature.

The purpose of annealing is to improve the crystallinity of the lattice. The surface of the particle may be amorphous and the lattice may be imperfect after the nucleation and growth steps. Annealing is carried out at a lower temperature than the nucleation and growth that occur shortly after the initial hot-injection. During annealing, the monomers and ions at the crystal surface are mobile, and can arrange to join the underlying lattice more perfectly. This is spontaneous thermodynamically because the radius of the lattice,  $r$ , provides a negative contribution to the total free energy of the particle by contributing to  $\Delta G_{\text{TOT}}$  as  $(4/3)\pi r^3 \Delta G_v$ .

## **1.5. THE CHEMICAL MECHANISM OF LEAD TELLURIDE NANOPARTICLE FORMATION**

Relevant to this research, mechanisms proposed for nanocrystal synthesis of the lead chalcogenides lead selenide (PbSe) and lead telluride (PbTe) from common precursors are reviewed. These syntheses often employ trioctylphosphine chalcogenide, TOP=E, as the source of the selenium or tellurium nucleophile, E.<sup>56, 59</sup> Lead acetate trihydrate serves as a common lead precursor that is often reacted with the surfactant oleic acid to form lead oleate according to the reaction scheme



The reaction produces acetic acid (boiling point ~390 K) and water as side products. These side products mostly boil off at 443 K with the help of argon flow, driving the reaction forward to dissolve the lead acetate. Some acetate remains in the solution to catalyze nanocrystal growth by acting as a short chain capping ligand in competition with oleate. The short chain acetate replaces some oleic acid on the particle surface to allow very small crystallites to aggregate and sinter.<sup>60</sup> The lead oleate, reacts with the TOP=E to form the monomer as displayed in Figure 1.4.<sup>59, 61-62</sup>

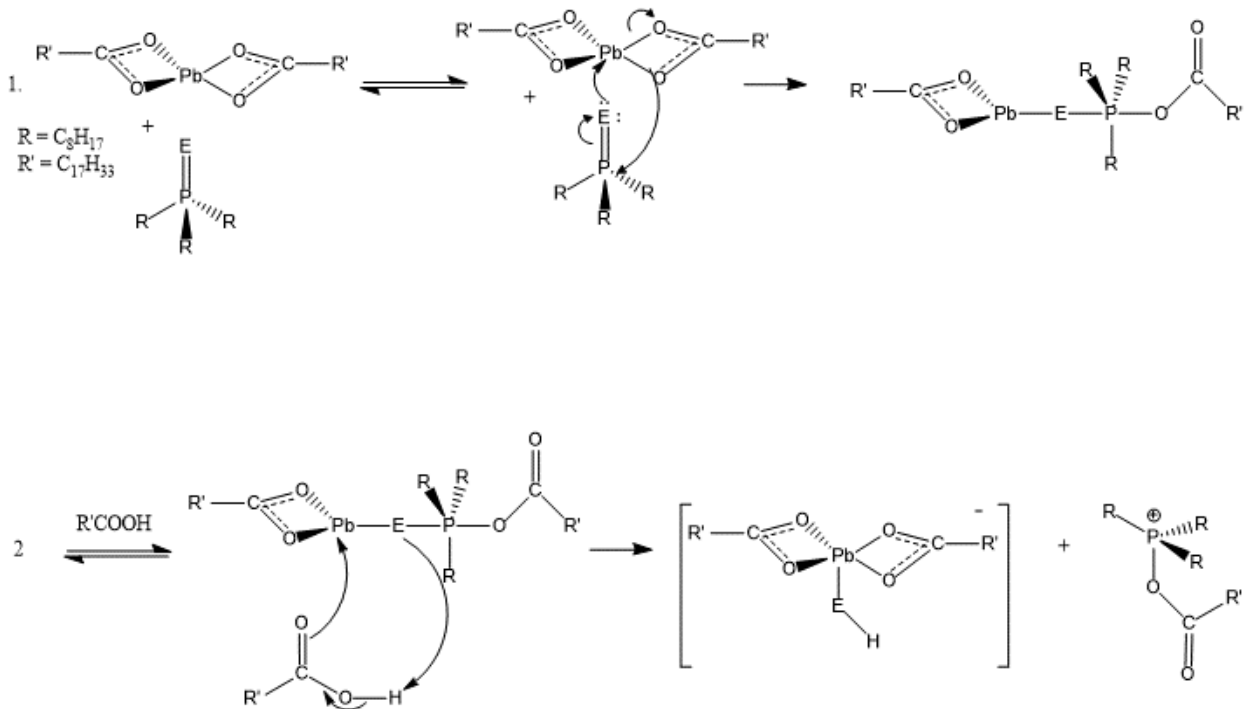


**Figure 1.4** The P=E bond is inserted between the lead and an oleate ( $\text{R}'\text{COO}^-$ ) in Scheme 1. Oleic acid transfers a proton to the electrophile (Scheme 2).

The cleavage of the bond between the electrophile and the phosphine has been investigated in detail (Figure 1.4).<sup>62</sup> The attack by the nucleophile on the metal cation (Scheme 1) is a concerted reaction resulting in the insertion of the P=E bond between the metal and the oleate. The acidic proton from an oleic acid is transferred to the nucleophile (Scheme 2) to

release trioctyl phosphonium oleate as a side product. This was trapped and observed. The main product could serve as the solubilized monomer. Alternatively, activation of the E–H by the metal would result in elimination of an oleic acid by proton transfer.

## **1.6. Thesis Statement #1: Nanostructuring of PbTe and PbS NC Inclusion for Increased ZT**

Lead telluride was chosen for bottom-up nanostructuring in this work because it is a traditional thermoelectric material for high temperature use ( $ZT \sim 1$  at 650 K) that exhibits improved thermoelectric properties from nanostructuring. Nanostructured PbTe demonstrates increased ZT relative to the bulk due to lower thermal conductivity<sup>6, 11, 13, 63</sup> and higher thermopower<sup>64-66</sup> caused by phonon scattering and carrier filtering at the grain boundaries.

Carrier filtering occurs because grain boundaries between crystals in PbTe exhibit energy barriers.<sup>64-66</sup> These energy barriers are a result of trap states at the particle surface that can result from lattice imperfections or chemisorption of oxygen on to nanocrystals.<sup>66</sup> Trapped carriers create a potential energy barrier by repelling like charges. These energy barriers can scatter holes near the top of the valence band and excited electrons near the bottom of the conduction band.<sup>64-66</sup> Filtering of low energy carriers increases the thermopower, contributing to a rise in ZT.

An alternative approach to augmenting ZT is to form grain boundaries by phase segregation. This approach has also been demonstrated by precipitation of lead sulfide NCs in lead telluride from a melt of lead, tellurium, and sulfur.<sup>10</sup> Precipitation within a mixture comprising 8 mol% of lead sulfide more than doubles the ZT of PbTe, to 1.5 at 642 K, by lowering  $\kappa_{\text{Lat}}$ , as displayed in Figure 1.5, by 80% to  $0.4 \text{ W m}^{-1} \text{ K}^{-1}$ .<sup>10</sup>

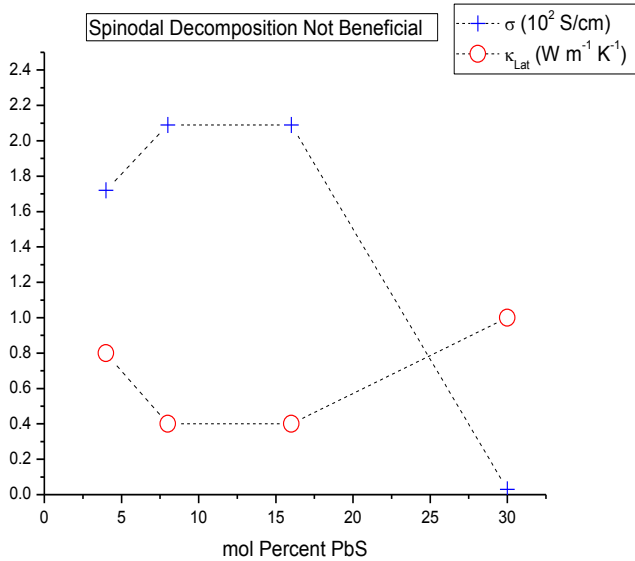


**Figure 1.5** Lattice thermal conductivity and electrical conductivity at 642 K are plotted versus mol% of lead sulfide.

Varying the lead sulfide mol% affected the thermal conductivity inconsistently due to the changing form of the lead sulfide with increasing mol%. The lead sulfide is observed as NCs at 4 mol%, then a combination of NCs and regions of alternating sulfur and tellurium richness resulting from spinodal decomposition at 8 mol%, then only the spinodal decomposition regions at 30 mol%. At this point the  $\kappa_{\text{Lat}}$  increases and  $\sigma$  decreases, demonstrating that spinodal decomposition regions are detrimental to ZT.<sup>10</sup>

Approaches to nanostructure PbTe have encountered barriers to increasing ZT. The crystallite sizes in PbTe nanostructured by top-down methods like ball milling are large (ca 100's of nm), therefore limiting the spectral range of phonons that can be scattered. Nanostructuring of PbTe by incorporation of PbS NCs through precipitation from a melt does increase ZT, but the increase is limited due to incorporation of spinodal decomposition regions as the mole percentage of PbS is increased, even at low levels (8 mol%).<sup>10</sup> Bottom-up methods using small nanocrystals (NCs) from solution-phase arrested precipitation result in low electrical conductivity and ZT due to insulating organic capping ligands required for size control.<sup>6,5,9,55,67</sup>

The tradeoff between size control and incorporation of insulating ligands presents a challenge to increasing ZT in PbTe-based thermoelectrics.

Efforts are being made to remove insulating ligands from colloidally prepared materials in order to employ nanoparticles in photovoltaic devices. Removal of organic ligands has been reported for thin films of lead sulfide, NCs by stripping with an ammonium sulfide solution to result in an inorganically connected assembly.<sup>67</sup> Another strategy exploited in the photovoltaics literature as an alternative means to modify the interfaces is ligand stripping of nanoparticles by iodide, resulting in a dramatic 700% increase in carrier mobility.<sup>68</sup> Ligand removal by hydrazine has been applied to thermoelectric materials resulting in a ten order of magnitude increase in electrical conductivity (to  $\sim 8.5 \text{ S cm}^{-1}$ ) for thin films<sup>69</sup> of lead selenide, PbSe, and electrical conductivity values up to  $22 \text{ S}\cdot\text{cm}^{-1}$  for hot-pressed pellets of PbS-PbSe hollow spheres.<sup>14</sup> Therefore, ligand stripping may offer a means to augment electrical conductivity in nanostructures assembled from dispersible NC building blocks, a premise that will be tested here for PbTe.

As one approach to improving the ZT of PbTe, we test whether PbTe nanostructured with PbS can be improved over that formed from a melt<sup>10</sup> by avoiding contributions from spinodal decomposition. Our strategy is to first grow dispersible PbTe and PbS NCs independently by hot-injection methods and then combine them by incipient wetness. To increase the practicality of assembling dispersible PbTe NCs into nanocomposites from the bottom-up, we design a new, multi-gram synthesis using hot-injection methods in solution. For combining the PbTe and PbS, we target 8 mol% PbS because this composition demonstrated the highest ZT in a previously reported PbTe–PbS composite formed from a melt.<sup>10</sup> The resulting material is then hot-pressed to form a PbTe–PbS nanocomposite. This material is characterized to test whether this method

of nanostructuring leads to decreased lattice thermal conductivity. As a second approach, we employ ligand stripping with several agents in an attempt to increase the electrical conductivity in bottom-up nanostructured PbTe by removing the insulating ligands from pre-grown, dispersible NCs. These two approaches are illustrated in Figure 1.6, and corresponding results will be presented in Chapter 3.

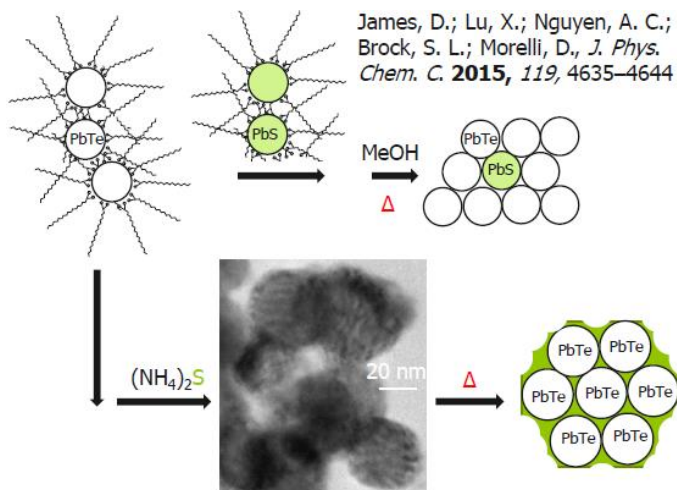


**Figure 1.6** Two approaches for PbTe based nanocomposites are displayed. Oleic acid capped PbTe NCs are mixed with oleic acid capped PbS by incipient wetness (Top). Methanol and heat are used consecutively to strip the oleic acid ligands and remove the solvent, resulting in PbTe–PbS. Alternatively, ammonium sulfide ( $(\text{NH}_4)_2\text{S}$ ) in methanol is used to strip the oleate, reacting with lead cations on the surface to result in a film of lead sulfide. Heating removes elemental sulfur to result in PbTe NCs held together by PbS at the interfaces.

## 1.7. THERMOELECTRIC MATERIALS FROM ABUNDANT ELEMENTS

A very different approach to increasing the practicality of thermoelectric devices is to avoid toxic and rare elements commonly required for thermoelectric materials and to focus on materials with naturally low lattice thermal conductivities, thereby avoiding the need to nanostructure.<sup>10-18</sup> Attempts to make “greener” thermoelectric materials have focused on copper-sulfides and selenides, particularly those adopting the chalcopyrite (zinc blende-based) structure type. However, doped CuInSe<sub>2</sub> and CuInS<sub>2</sub> exhibit relatively low ZT even up to 550 K,<sup>70-71</sup> whereas the more promising nanostructured CuAgSe<sub>2</sub> reaches a maximum ZT of 0.55 at 700 K.<sup>72</sup>

The tetrahedrite mineral,  $\text{Cu}_{12}\text{Sb}_4\text{S}_{13}$ , is not only composed of only Earth abundant elements, but also exhibits an intrinsically low lattice thermal conductivity ( $\kappa_L=0.4\text{Wm}^{-1}\text{K}^{-1}$  at 700 K).<sup>2-3</sup>

Unique features in the tetrahedrite crystal structure are responsible for an intrinsically low lattice thermal conductivity (Figure 1.7 a). The features of interest in the unit cell are emphasized by enclosing with a rectangle. For clarity, this arrangement of atoms in the unit cell is displayed in Figure 1.7b after removal of other atoms. The structure consists of trigonal planar  $\text{Cu}^+$  ions interacting with 3  $\text{S}^{2-}$  ions and 2  $\text{Sb}^{3+}$  ions. The two  $\text{Sb}^{3+}$  ions, one above the plane and one below, each possess a lone pair and form a trigonal pyramidal shape with three S ions.

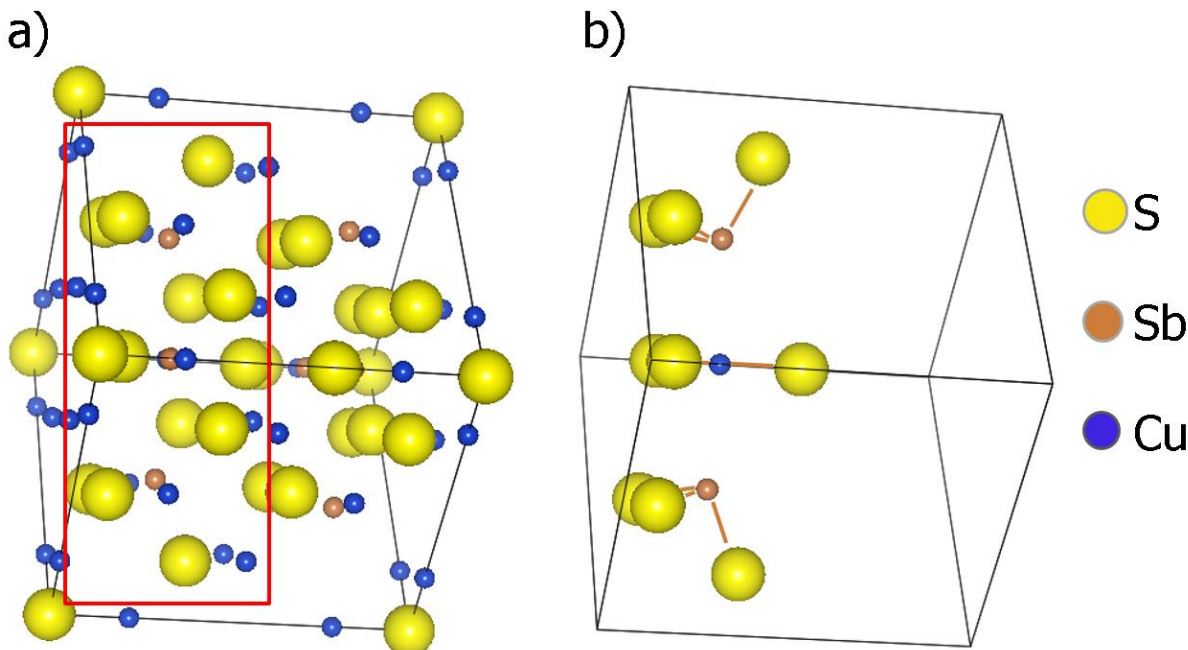


**Figure 1.7** The unit cell<sup>73</sup> (a) of tetrahedrite, Inorganic Crystal Structure Database code 41753, projected parallel to a triangular plane formed by a Cu atom (blue) with three S atoms (yellow) is displayed. A rectangle is added to point out a region of the cell containing an arrangement of two trigonal pyramidal Sb atoms (brown) above and below the trigonal planar Cu. The unit cell is displayed again in the same orientation (b) for clarity after hiding all atoms not included in this arrangement of two trigonal pyramidal Sb atoms above and below the trigonal planar Cu. Reprinted (adapted) with permission from James, D. J.; Lu, X.; Morelli, D. T.; Brock, S. L., Solvothermal Synthesis of Tetrahedrite: Speeding Up the Process of Thermoelectric Material Generation. *ACS Appl. Mater. Interfaces* **2015**, DOI: 10.1021/acsami.5b07141. Copyright 2015 American Chemical Society.

Thus, the Cu is positioned to interact with the lone pair on either Sb ion. The intrinsic low lattice thermal conductivity ( $\kappa_L=0.4\text{Wm}^{-1}\text{K}^{-1}$  at 700K) of tetrahedrite,  $\text{Cu}_{12}\text{Sb}_4\text{S}_{13}$ , stems from the anharmonic vibration of Cu atoms vertical to the S triangle plane as they dynamically interact

with the lone pairs on Sb atoms above and below.<sup>74</sup> This results in a trigonal bipyramidal Cu ion that acts as a rattler in a cage. The changing vibration frequency with cell volume leads to a high Grüneisen parameter resulting in low  $\kappa_L$  due to destructive interference of the phonons.<sup>75</sup>

The role of lone pairs contributed by Sb<sup>3+</sup> is further explored by comparison of tetrahedrite crystal structures formed by Cu<sub>12</sub>Sb<sub>2</sub>Te<sub>2</sub>S<sub>13</sub> ( $\kappa_L = 0.7 \text{ W m}^{-1} \text{ K}^{-1}$ ) and Cu<sub>10</sub>Te<sub>4</sub>S<sub>13</sub> ( $\kappa_L = 1.4 \text{ W m}^{-1} \text{ K}^{-1}$ ).<sup>76</sup> The latter compound possesses random copper vacancies in the tetrahedrite structure, which fail to lower the  $\kappa_L$ . The low  $\kappa_L$  of Cu<sub>12</sub>Sb<sub>2</sub>Te<sub>2</sub>S<sub>13</sub> is due to a unique abundance of low energy (~3 meV) vibrational modes not present in Cu<sub>10</sub>Te<sub>4</sub>S<sub>13</sub>, and Raman spectroscopy measurements associate these with out-of-plane vibrations of the trigonal planar copper. These results corroborate an increased out of plane displacement of the trigonal planar copper in Cu<sub>12</sub>Sb<sub>2</sub>Te<sub>2</sub>S<sub>13</sub> compared to Cu<sub>10</sub>Te<sub>4</sub>S<sub>13</sub>. This indicates that the 5s<sup>2</sup> lone pair from antimony interacts with copper while that of tellurium is truly inert. Bouyrie, *et. al.* suggest that, rather than a bond being formed, the displacement of the trigonal planar copper results in a dipole that interacts with the dipole formed by the stereochemically active (from partial sp<sup>3</sup> hybridization) lone pair on Sb<sup>3+</sup>. This results in the low energy vibrational modes that interfere with acoustical phonons for decreased  $\kappa_L$ . Similarly low energy (4 meV) vibrational modes were assigned to the trigonal planar copper in pure tetrahedrite, Cu<sub>12</sub>Sb<sub>4</sub>S<sub>13</sub>.<sup>74</sup>

The 12 copper equivalents in Cu<sub>12</sub>Sb<sub>4</sub>S<sub>13</sub> consist of 10 Cu<sup>+</sup> and 2 Cu<sup>2+</sup> ions. The latter of these can be replaced by Zn<sup>2+</sup> or other transition metals to modulate electronic properties by adjusting the Fermi Level. The pure tetrahedrite, Cu<sub>12</sub>Sb<sub>4</sub>S<sub>13</sub>, is *p*-type and metallic with the Fermi Level in the valence band.<sup>3</sup> The density of states diagrams have been determined by Suekuni *et al.* for tetrahedrite with several transition metal (TM) dopants (Cu<sub>11</sub>M<sub>1</sub>Sb<sub>4</sub>S<sub>13</sub>) M = Mn, Fe, Co, or Ni (Figure 1.8).<sup>77</sup> For Cu<sub>12</sub>Sb<sub>4</sub>S<sub>13</sub> there are two available energy states in the

valence band above the Fermi Level that electrons can easily be excited into, resulting in metallic character.<sup>2, 77-78</sup> The metal-semiconductor transition occurs at 85 K; so, at higher temperatures, resistivity increases consistent with a metal.<sup>77, 79</sup> The bandgap is between 1.2 eV for bulk and up to 1.7 eV for nanocrystals and can be modified by doping with transition metals (Figure 1.8).<sup>2, 77-78, 80</sup> For instance, bulk tetrahedrite doped with Zn<sup>2+</sup> or Mn<sup>2+</sup> has demonstrated bandgaps of 1.8 eV.<sup>81</sup>

Metals have been incorporated by in-situ doping during solid state synthesis to optimize ZT, forming Cu<sub>12-x</sub>(TM)<sub>x</sub>Sb<sub>4</sub>S<sub>13</sub>, TM = Zn, Mn, Fe, Co, Ni, or Zn.<sup>2, 77, 81-85</sup> The pure element is used as the source of dopant in solid state syntheses, and is mixed with copper, antimony, and sulfur in the desired stoichiometry to yield the product.

The Keszler group prepared tetrahedrite samples doped with Mn, Fe, Co, Ni, or Zn at a dopant level of x = 2 and compared them with the pure tetrahedrite up to 575 K. Doping with Mn or Co lead to improved ZT values of 0.8 and ~0.5 at 575 K, respectively.<sup>81</sup> The Mn-doped sample achieves the high ZT by increasing the thermopower while moderately decreasing the electrical conductivity and the thermal conductivity. The increased thermopower in this sample is attributed to the increased band gap of 1.8 eV. This is the same band gap measured for the Zn-doped sample. The larger band gap prevents electrons from exciting across to the conduction band, where they would be more mobile. Flow of excited electrons to the cold end would lower the thermopower. Doping with Fe, Co, or Ni results in a smaller band gap due to the effect of their magnetic moment on the band structure (Figure 1.8b, c, and d).<sup>77, 81</sup> The band gap is smaller due to splitting of the orbitals into low energy (majority-spin) states and high energy (minority-spin) states generated at the top of the valence band.

**1.7.1. Ni-Doping.** Doping with Nickel results in little change in the maximum ZT compared to pure tetrahedrite (~0.3 at 575 K).<sup>81</sup> The electrical conductivity and thermal conductivity for this sample are decreased similarly to the better performing Mn-doped sample (vide infra), but the increase in thermopower is disproportionately small. The substituted nickel exhibits a magnetic moment consistent with  $\text{Ni}^{2+}$  with a spin of S=1 at doping levels of  $x = 2$  or  $x = 1.5$ .<sup>77, 79</sup> The spin should be S=1 for  $d^8$  with 6 paired and two unpaired electrons. Substitution of the  $\text{Ni}^{2+}$  for  $\text{Cu}^{2+}$  would be expected to inject holes into the lattice, due to  $\text{Ni}^{2+}$  being only  $d^8$  and having one less  $d$  electron than  $\text{Cu}^{2+}$ . Injection of holes into the valence band of the *p*-type material would result in a metallic behavior like that exhibited by the pure tetrahedrite; however, the Ni-doped tetrahedrite exhibits semiconductor behavior, and there is no metal to semiconductor transition at low temperatures.<sup>77, 79</sup>

The semiconductor behavior for Ni-doping is due to the magnetic moment. Nickel doping causes the states at the Fermi Level to split because the unpaired electrons can either have the same spin as the majority of unpaired electrons, lowering the energy below the Fermi Level for the  $x = 1$  doping level (majority-spin band), or have the opposite spin, raising the energy above the Fermi Level (minority-spin band). This leaves the Fermi Level between the two bands, resulting in the semiconducting behavior (Figure 1.8d).<sup>77</sup>

**1.7.2. Zn, Fe-Doping.** For the samples doped with Zn or Fe, ZT decreased due to low electrical conductivity.<sup>81</sup> This is because the doping is not optimized, and the high level of Zn doping ( $x = 2$ ) leads to a filled valence band, resulting in a semiconductor instead of a metal.<sup>81</sup> The zinc contributes 3d orbitals well below the Fermi Level, consistent with  $\text{Zn}^{2+}$ , which does not contribute a magnetic moment and so does not lead to any band splitting between minority and majority bands (Figure 1.8e).<sup>77</sup> Thus, the band structure near the Fermi Level is not

modified from that of the pure tetrahedrite. Instead the Fermi Level is raised towards the top of the valence band by contribution of the extra electron ( $d^{10}$ ) in comparison to  $\text{Cu}^{2+}$  ( $d^9$ ) as discussed previously. These results agree with zinc-doped, solid state samples reported by Lu *et. al.* demonstrating relatively low resistivity for  $x = 0.1$ , an order of magnitude increase in resistivity for  $x = 1.5$ , and insulating behavior for  $x = 2$ , indicating a semiconducting material.<sup>2</sup> Decreased carrier contributions to thermal conductivity and increased thermopower values result in high temperature (700 to 750 K) ZT values of 1 and 0.8 for  $x = 0.5$  and  $x = 1$ , respectively. Thus, the ideal doping level for Zn-doped tetrahedrite is in this region. At higher concentrations ( $x \geq 1.5$ ), the ZT decreases due to high resistivity.

Doping with iron for  $x = 2$  also decreases ZT by greatly decreasing the electrical conductivity, but the  $\text{Fe}^{2+}$  actually has fewer  $d$  electrons ( $d^6$ ) to contribute than  $\text{Cu}^{2+}$  ( $d^9$ ); therefore, the valence band should not be filled. Instead, the decreased electrical conductivity in this case could be attributed to impurity scattering and hole-trapping by  $\text{Fe}^{2+}$ .<sup>81</sup> Further investigation into the band structure and magnetic properties of the substituting iron provide another explanation. The divalent state of iron is confirmed for  $x \geq 1.5$ .<sup>77</sup> At lower doping levels,  $x = 0.5$  and  $x = 1$ , it would be  $\text{Fe}^{3+}$ .<sup>86</sup> In either case, the substituted iron exhibits a magnetic moment, and splitting of bands near the Fermi Level into minority-spin and majority-spin results in a gap at the Fermi Level, leading to semiconductor behavior and low electrical conductivity (Figure 1.8b). Earlier studies by Lu, *et. al.* at lower doping levels proposed that doping with  $\text{Fe}^{3+}$  resulted in raising the Fermi Level by contributing two extra electrons to the valence band per  $\text{Fe}^{3+}$  instead of the one extra electron contributed by  $\text{Zn}^{2+}$ . This results in a maximum ZT of 0.8 at a doping level of only  $x = 0.5$  due to increased resistivity (lowering thermal conductivity) and increased thermopower.<sup>2</sup>

**1.7.3. Mn, Co-Doping.** The decrease in electrical conductivity for  $Mn^{2+}$  and  $Co^{2+}$  doped tetrahedrite is less severe because they are less oxidizing<sup>81</sup> and lack the propensity for hole-trapping, in addition to magnetic contributions to the band structure (Figure 1.8a and c).<sup>77</sup> The substituted  $Mn^{2+}$  has a magnetic moment which was determined for  $x = 1.8$  to be of  $7.45 \mu_B$  per formula unit.<sup>85</sup> The magnetic moment results in a majority-spin band below the Fermi Level and a minority-spin band above the Fermi Level extending into the band gap from the conduction band above.<sup>77</sup> In contrast to Ni-doping, there are still available states at the Fermi Level, and the valence band extends above it. Thus, the Mn-doped tetrahedrite retains metallic behavior rather than becoming a semiconductor.<sup>77</sup> For Co-doping, the cobalt is  $Co^{2+}$ , and leads to a minority-spin state in the band gap with a majority-spin state below the Fermi Level. However, there are still available states at and extending above the Fermi Level, similar to the Mn-doped tetrahedrite, which maintains metallic behavior. The moderate decrease in electrical conductivity suppresses the carrier contribution to thermal conductivity,  $\kappa_C$ , at high temperature, leading to an over 70% decrease in the thermal conductivity for improved ZT in the Co and Mn-doped samples.<sup>81</sup> Further optimization revealed a decreasing electrical conductivity and increasing thermopower with Mn from  $x = 0.5$  to  $2.0$ , resulting in a maximum ZT of  $1.13$  with  $x = 1$ . This is slightly higher than the ZT of  $1$  for  $x = 0.5$ . Chetty, *et. al.* investigated Mn-doped tetrahedrite from  $x = 0.4$  to  $1.8$ , and noted the increasing resistivity with temperature for doping levels of  $x = 0.4$  up to  $x = 0.9$ , indicating metallic behavior.<sup>85</sup> At higher doping levels,  $x = 1.4$  and  $x = 1.8$ , the resistivity decreased with temperature, indicating semiconductor behavior. Therefore, they propose that increasing the substitutional doping of  $Mn^{2+}$  for copper fills the valence band changing the band structure. This results in less of the majority carrier, holes, to

increase the thermopower with increasing Mn<sup>2+</sup> similarly to Zn-doping. They demonstrate maximum ZT values of 0.65 for x = 0.4 and 0.45 for x = 0.9.<sup>85</sup>

## **1.8. Thesis Statement #2: Rapid and Facile Synthesis of Tetrahedrite and Doped Systems on Large Scale**

Although the advantageous qualities of tetrahedrite have led to several licensed patents as a thermoelectric,<sup>87-88</sup> the long and energy intensive synthesis of tetrahedrite serves as a roadblock to industrial production as a thermoelectric material. Tetrahedrite is currently prepared by high-temperature solid-state synthesis, which requires three days in a tube furnace as reagents are heated slowly to 650 °C and then slowly allowed to cool.<sup>2-3</sup> The product is then ball-milled and annealed for two weeks at 450 °C before being ball-milling again and hot-pressed. As an alternative synthesis method, recent work has demonstrated that tetrahedrite can be grown in solution as discrete nanocrystals by hot-injection methods on a small scale (ca. 0.5 mmol copper precursor per reaction) using long chain ligands as capping agents.<sup>89</sup> However, adaptation of these nanocrystals for thermoelectric use would face the dual challenges of small scale production and the need to eliminate the long chain ligands that increase resistivity by orders of magnitude in other thermoelectric systems.<sup>55, 69</sup> Moreover, it is doubtful that the benefits of phonon scattering achieved by nanostructuring<sup>90</sup> will be realized in this system because of the inherently low κ<sub>L</sub>.

Recent work with tetrahedrite has focused on decreasing the reliance on synthetic tetrahedrite for thermoelectric use by taking advantage of its ability to form solid solution with the naturally occurring tennantite.<sup>91</sup> Tetrahedrite naturally occurs as tennantite, Cu<sub>(12-x-y)</sub>Zn<sub>x</sub>Fe<sub>y</sub>As<sub>4</sub>S<sub>13</sub>, with arsenic in place of antimony and substitutional doping of copper sites by zinc and iron. This plentiful mineral has low electrical conductivity due to excessive doping;

however, ball-milling tennantite in an approximately 1:1 mole ratio with synthetic tetrahedrite shifts the XRD spectrum to lower 2-Theta by diluting impurities. This adjusts the doping level and increases the ZT to one.<sup>3</sup>

The zinc-rich tennantite ( $\text{Cu}_{10.0} \text{Zn}_{1.8} \text{Fe}_{0.2} \text{As}_{2.7} \text{Sb}_{1.3} \text{S}_{13}$ ) serves as a source of  $\text{Zn}^{2+}$  for doping. Substitution of  $\text{Cu}^{2+}$  ions by  $\text{Zn}^{2+}$  in the solid solution is proposed to raise the Fermi Level toward the top of the valence band by adding one additional electron per  $\text{Zn}^{2+}$  (see 1.7.2).<sup>2</sup>

<sup>3</sup> The density of states decreases near the top of the valence band, resulting in a *p*-type material due to lower mobility of excited electrons (Figure 1.8e).<sup>77</sup> As the Fermi Level is raised, the holes are generated nearer to the top of the valence band, and the low density of states results in filtering of the low energy holes. This increases  $\alpha$  and  $\rho$  to tune the electronic and thermal properties.<sup>2-3</sup> The optimum doping level for  $\text{Cu}_{(12-x)}\text{Zn}_x\text{S}_{13}$  has been achieved at  $x = 0.9$  for a ZT  $\sim 1$  at 700 K by ball-milling the natural mineral with the un-doped solid state material.<sup>3</sup>

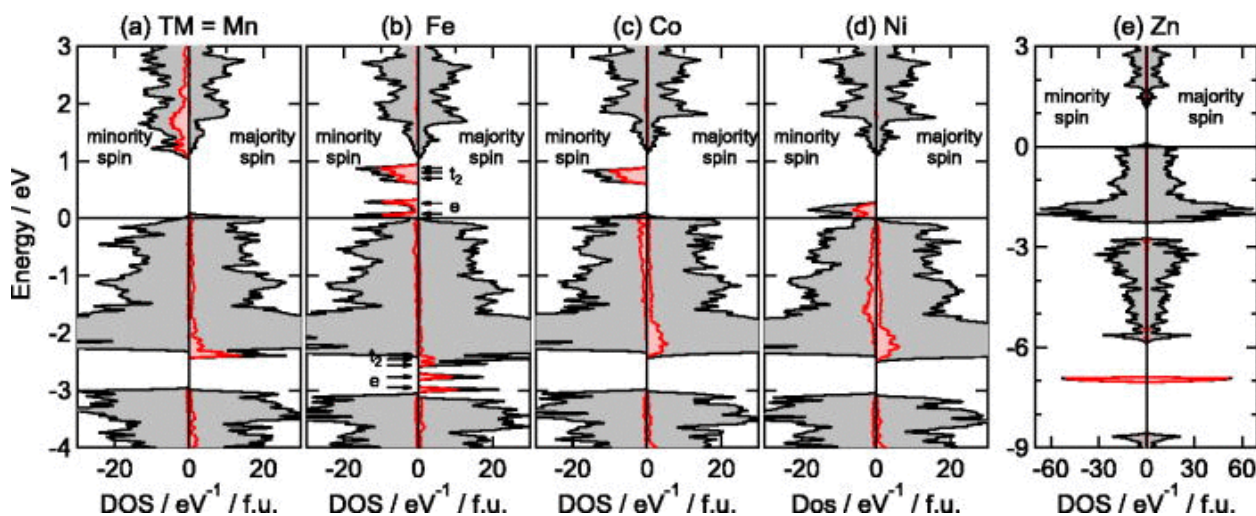


**Figure 1.8** Spin-resolved electronic DOS for  $U=0$  of  $\text{Cu}_{11.0}\text{TM}_{1.0}\text{Sb}_4\text{S}_{13}$  (TM=Mn (a), Fe (b), Co (c), Ni (d), and Zn (e)). The red area describes the partial DOS for TM. Reprinted with permission from Suekuni, K.; Tomizawa, Y.; Ozaki, T.; Koyano, M., Systematic Study of Electronic and Magnetic Properties for  $\text{Cu}_{12-x}\text{TM}_x\text{Sb}_4\text{S}_{13}$  (TM = Mn, Fe, Co, Ni, and Zn) Tetrahedrite. *J. Appl. Phys.* **2014**, *115* (14), 143702. Copyright 2014, AIP Publishing LLC.

While tennantite also serves as a source of iron or arsenic, arsenic incorporation has not been discussed as playing a role in tuning electronic properties in previous works.<sup>2-3</sup> However,

mixing iron-rich tennantite ( $\text{Cu}_{10.5}\text{Fe}_{1.5}\text{As}_{3.6}\text{Sb}_{0.4}\text{S}_{13}$ ) with synthetic tetrahedrite has been found to increase ZT by tuning electronic properties to an optimum doping level of 0.38 mole equivalents of iron (vs. 0.9 moles of Zn). Nevertheless, the ZT is lower (0.8 at ~700 K) than that achieved by mixing tetrahedrite with the zinc-rich tennantite.<sup>3</sup> The iron present from mixing zinc-rich tennantite ( $\text{Cu}_{10.0}\text{Zn}_{1.8}\text{Fe}_{0.2}\text{As}_{2.7}\text{Sb}_{1.3}\text{S}_{13}$ ) in a 1:1 mole ratio with tetrahedrite would be quite small at 0.1 mole equivalents. At this amount, the iron would be  $\text{Fe}^{3+}$  and would contribute two extra electrons to the valence band per iron, raising the Fermi Level similarly to zinc.<sup>2, 86</sup> However, the  $\text{Fe}^{3+}$  also results in impurity bands above the Fermi Level in Fe-doped tetrahedrite (Figure 1.8b).<sup>77, 86</sup> The impurity bands are formed due to the magnetic moment of  $\text{Fe}^{3+}$  from the  $d^5$  electron configuration. The magnetic moment results in a splitting of available energy states in the valence band. The electrons can either be aligned with the majority of spins from unpaired electrons, lowering the energy, or be opposed to them, raising the energy. This results in a majority-spin band below the Fermi Level and a minority-spin band above it. The addition of Zn-doping raises the Fermi Level, and the minority-spin band provides extra energy states to be filled by the added electrons from Zn-doping. Therefore, the Fe-doping could increase the amount of zinc that can be incorporated before the material becomes insulating (Figure 1.8b). As a result, the maximum ZT ~1 was achieved for  $x = 0.95$  using zinc-rich tennantite as the dopant source.<sup>3</sup> This is significantly more zinc than the  $x = 0.5$  required for optimal Zn-doping (ZT ~1) of solid state tetrahedrite in the absence of iron.<sup>2</sup>

In the present work, we attempt to address the problem of long synthesis times at high temperatures and limited scalability for preparation of tetrahedrite. To alleviate these problems, we develop and optimize a chloride-free solvothermal route to synthetic tetrahedrite that can be done with two days of heating at moderate temperatures (ca 150 °C) and allows parallel

processing due to the manageable temperature and pressure requirements. Thermoelectric characterization is carried out on the product as well as on a 1:1 mixture of the product with natural mineral (tennantite). We show that properties of the solvothermal tetrahedrite are comparable to those produced by solid state methods and that our product is amenable to doping by mixing with tennantite. These results will be discussed in Chapter 4. In addition to doping by ball-milling with tennantite, we modify our solvothermal synthesis to dope in-situ with zinc for  $\text{Cu}_{12-x}\text{Zn}_x\text{Sb}_4\text{S}_{13}$  over a range of  $x = 0.79$  to  $1.40$  to modulate the electronic and thermal properties. These results will be discussed in Chapter 5.

## CHAPTER 2 : EXPERIMENTAL

### 2.1. INTRODUCTION

**2.1.1. Lead Telluride Based Thermoelectric Materials.** This work pursues multiple approaches to improve thermoelectric properties using several types of materials. For the first approach, lead telluride (PbTe) is nanostructured from the bottom up to decrease thermal conductivity. This entails the development of a new, multi-gram synthesis of dispersible PbTe nanocrystals (NCs) and their characterization. The PbTe NCs are then treated with methanol, ammonium sulfide, tetrabutylammonium iodide, or ammonium sulfide followed by tetrabutylammonium iodide to strip the insulating ligands in a strategy to improve the electrical conductivity of the resulting nanostructured material. In addition, lead sulfide (PbS) NCs are synthesized, characterized, and mixed with PbTe NCs by incipient wetness to provide nanocrystalline impurities for decreased thermal conductivity. These nanostructured materials are annealed to remove solvent and excess sulfur (in the case of the sulfide-stripped PbTe NCs). Then, they are hot-pressed to prepare pellets for the characterization of thermoelectric properties. The experimental details relative to synthesis of the PbTe and PbS NCs as well as mixing of NCs by incipient wetness, ligand stripping, and annealing are described in Chapter 3.

Characterization is performed at each stage of the process. The PbTe and PbS NCs are investigated by X-ray diffraction (XRD) to determine crystallinity, phase, and crystallite diameter. They are imaged by Transmission Electron Microscopy (TEM) to observe the size and morphology. Energy dispersive X-ray spectroscopy (EDS) is employed to investigate the composition. The PbTe NCs are similarly characterized by TEM and EDS following ligand stripping or mixing with PbS, before and after annealing, to investigate changes in the particle surface, aggregation, and composition. Investigation by XRD is carried out after annealing and

again after hot-pressing to monitor changes in the crystallite size. The average composition of the hot-pressed material is determined by Inductively Coupled Plasma-Optical Emission Spectroscopy (ICP-OES). The hot-pressed material was cut into a rectangular parallel-piped and characterized further by determining the room temperature electrical conductivity, thermopower, and thermal conductivity in a cryostat using standard steady state techniques. The cryostat setup is equipped with a set of thermocouples to monitor the temperature, a resistor to apply heat, an ohmmeter to monitor resistance, and a voltmeter to monitor the voltage drop across the rectangular parallel-piped.

**2.1.2. Tetrahedrite Based Materials.** As an alternative approach to improving thermoelectric materials, we develop a rapid, solvothermal method to produce tetrahedrite and dope it by ball-milling it with the natural mineral tennantite ( $\text{Cu}_{10.0}\text{Zn}_{1.8}\text{Fe}_{0.2}\text{As}_{2.7}\text{Sb}_{1.3}\text{S}_{13}$ ) as a source of zinc. In addition, we adapt the synthesis for zinc doping in-situ. The tetrahedrite is produced in multiple Teflon-lined vessels in parallel by sealing them in stainless steel bombs and heating in a laboratory oven. Each solvothermal product is investigated by XRD for crystallinity and characterized by either ICP-OES or Inductively Coupled Plasma-Mass Spectroscopy (ICP-MS). Samples are hot-pressed to prepare a pellet for characterization of thermoelectric properties as described above. Experimental details relative to the solvothermal synthesis of the undoped tetrahedrite as well as ball-milling the solvothermal tetrahedrite with the natural mineral are described in Chapter 4. Experimental details relevant to in-situ doping of the solvothermal tetrahedrite is described in Chapter 5.

The thermoelectric properties are studied at low temperature for preliminary data, and at high temperature for more promising specimens. The hot-pressed material is cut into a rectangular parallel-piped for determination of thermoelectric properties near room temperature

as described above. For high temperature measurements, a disc and a rectangular parallel-piped are cut from the pellet. The thermopower and resistivity are determined on the rectangular parallel-piped by standard steady state techniques, and the resistance is measured using the four-probe method.<sup>92</sup> The disc is used to determine the thermal diffusivity (D) with the laser flash technique.

## 2.2. CHARACTERIZATION

**2.2.1. Size and Morphology Observation by TEM.** A JEOL 2010 TEM instrument is used to take electron microscopy images utilizing a 200 kV accelerating voltage. The microscope has an EDAX Energy Dispersive X-ray Spectrometer as an accessory. To prepare NCs of PbTe or PbS for imaging, a spatula-tip of sample is dispersed in hexane by sonication to form a colloid solution. A drop of colloid solution is applied to a carbon coated copper grid (200 mesh Cu grid from SPI) supported on filter paper on a vacuum filtration funnel. Vacuum is applied to quickly remove solvent. If the sample cannot be completely dispersed, as is the case for annealed samples of NCs and the tetrahedrite synthesized by literature methods, the solid is transferred to the grid with hexane and a disposable pipette.

A TEM instrument works on the principle that an electron has a wavelength on the Ångstrom scale (~0.04 Å at 90 KV accelerating voltage) when in motion. This allows electrons to resolve features less than a nanometer in size (< 2 Å).<sup>93</sup> The wavelength decreases with accelerating voltage according to the DeBroglie wavelength  $\lambda = h / p$ , with  $h$  being Planck's constant, and  $p$  being the momentum. This results in the  $\lambda$  following the equation  $\lambda = \frac{h}{(2meV)^{1/2}}$ , with  $m$  being the mass of the electron,  $e$  being the charge of the electron,  $V$  being the accelerating voltage, and  $h$  being the Planck's constant. The wavelength is further decreased as the velocity

of the electron approaches the speed of light, increasing the relativistic mass and increasing the momentum. The electrons are essentially used in place of light for microscopy.

The basic layout of a TEM consists of a beam of electrons generated by a source or electron gun, which passes through a sample to a detector, such as a fluorescent screen, a film, or a digital camera to generate an image. The electron gun consists of a metal filament, from which electrons are removed and directed by an accelerating voltage. For the JEOL 2010 TEM, current (106–108  $\mu\text{A}$ ) is applied to a LaB<sub>6</sub> filament which emits electrons thermionically.<sup>94</sup> The 200 KV accelerating voltage accelerates them through a set of magnetic lenses. The magnetic field from the magnetic lenses focuses the electrons into a beam that converges through a central point, the focal point. The beam passes through an objective aperture to remove stray electrons while allowing the center of the beam to pass through. These electrons pass through the sample and the focal point. Electrons can be scattered by atoms in your sample, and are scattered more effectively by atoms with higher atomic number.<sup>93</sup> The electrons that are not scattered are transmitted and used to generate the bright field image. These pass through an aperture to remove scattered electrons and are focused by another set of magnetic lenses before striking the detector to create the bright field image. We first use a fluorescent screen as a detector and attempt to focus the image by adjusting the height of the sample stage (Z-height) to position our sample at the focal point. Once the bright field image appears to be in focus, and the contrast of the image is low, then the fluorescent screen is removed to allow the electrons to pass through to the HRTEM digital camera.<sup>94</sup> While observing the live feed from the camera, we fine tune the focus to obtain clear images. This allows us to observe the size and morphology of nanocrystals in this work. Images are processed and saved with Amtv600 software from the Advanced Microscopy Techniques Corporation.

**2.2.2. Composition Determination by EDS.** The EDS technique takes advantage of the X-rays released by the process of scattering electrons, and is often coupled with TEM as an accessory to the microscope. Our JEOL 2010 TEM is coupled to an EDS detector by EDAX Inc. When electrons are scattered by atoms, the incident electrons can remove inner shell electrons (K shell or 1s) from the atom. As a result, higher energy electrons such as L shell (2s) or M shell (2p) can emit X-rays to relax and fill the hole in the inner shell (Figure 2.1).<sup>93</sup> This transition will release an X-ray with an energy equal to the difference between the two levels, resulting in a frequency ( $\nu$ ) according to  $E = h\nu$ , with  $E$  being energy and  $h$  being Planck's constant. Since chemical bonds are formed with valence electrons, transitions between other energy levels are characteristic of the particular element of an atom, rather than its bonding to other atoms. This allows EDS to detect individual elements in a sample according to characteristic X-rays that are emitted. The X-rays are counted over a period of seconds by a solid-state semiconductor detector. They excite electrons to generate holes and excited electrons, which are measured as a charge pulse which is converted to a voltage pulse by a charge-to-voltage converter.<sup>94</sup> The data is processed by the EDAX genesis software 1.0. The spectrum is basically a histogram created from the X-rays detected at each energy. The result is a plot of counts versus energy that exhibits peaks at the energies released by electronic transitions in the elements that are detected. The energy for the peak may be consistent with transitions of several different elements; therefore, the user will choose the element from this list that is likely to be in the sample. If more than one of these elements is likely to be present (overlapping peaks), then it may be necessary to use a different peak (K, L, or M). Once the element is chosen, the peak area is used with a scaling factor specific to the element and the transition to calculate the mass present for each element. The mass of each element is reported as a weight percent of the total mass of all

the elements chosen, and these are used to calculate the atomic percent of each element detected based off of the atomic weight. For example, PbTe nanocrystals would ideally exhibit 50 % atomic percent each for Pb and Te, for a ratio Pb:Te of 1:1.

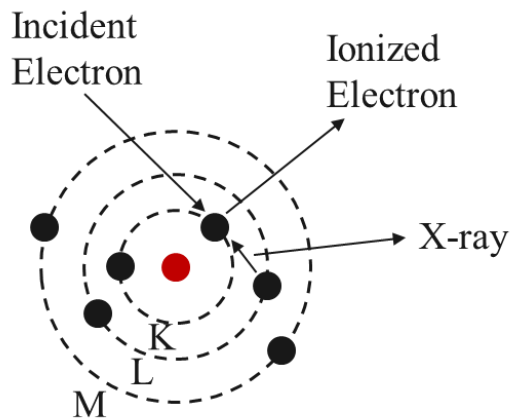


**Figure 2.1** A simple diagram of inner shell electrons (K shell, L shell, and M shell) in an atom. An electron from the electron gun ionizes a K shell electron, and an electron from the L shell relaxes via emission of an X-ray.

**2.2.3. Investigation of Phase and Crystallite Size by XRD.** Solids were analyzed for crystalline features by X-ray Diffraction (XRD) with a Rigaku Smartlab Powder X-ray Diffractometer over a range from  $20\text{--}80 = 2\theta$ . Powders are mounted on a zero-background quartz sample holder. For incorporation of Silicon as an internal standard, a spatula-tip of silicon is mixed with the analyte by grinding prior to mounting. Jade 5.0 software is used to process the diffraction patterns. Diffraction patterns from the ICDD Powder Diffraction File (PDF) database were compared to patterns from our products to identify crystal structures.

Most XRD instruments have several main parts: an electron source, a metal anode as the X-ray source, a monochromator, a stage to hold the analyte, and a detector. The electron source consists of a filament, from which electrons are accelerated at a controlled voltage. These strike the anode (usually copper) and remove inner shell electrons. Higher energy electrons relax to fill the holes and emit X-rays. This occurs similarly to the generation of X-rays described above for the EDS technique (Figure 2.1). The monochromator selects the desired X-ray wavelength. For

a copper anode, this usually corresponds to the  $K_{\alpha}$  transition of an electron from an outer shell (the  $2p$  orbital) to the inner K shell (the  $1s$  orbital).<sup>93</sup> A basic monochromator consists of a diffraction grating and a properly placed mirror to redirect the desired wavelength to the analyte stage. The X-rays are scattered by atoms in the solid, directing some of them back toward the detector.

The  $K_{\alpha}$  wavelength is small enough ( $1.54 \text{ \AA}$ )<sup>93</sup> to interact with parallel, repeating planes (lattice planes) in a crystal like a diffraction grating because it is on the scale of interatomic distances in a solid. As the X-ray hits the solid analyte, it can be scattered off lattice planes near the surface of the solid or pass through and penetrate until scattering off a plane deeper in the crystal. Some of the scatter exits back out through the surface of the crystal toward the detector. The X-rays scattered off of a plane at the surface will travel a different pathlength than those that scatter off of planes in the interior of the solid. This results in X-rays traveling many discrete pathlengths. The different pathlengths result in a difference in phase leading to constructive or destructive interference (Figure 2.2).<sup>93</sup> Constructive interference between two pathlengths results in a maximum in X-ray intensity (a peak).

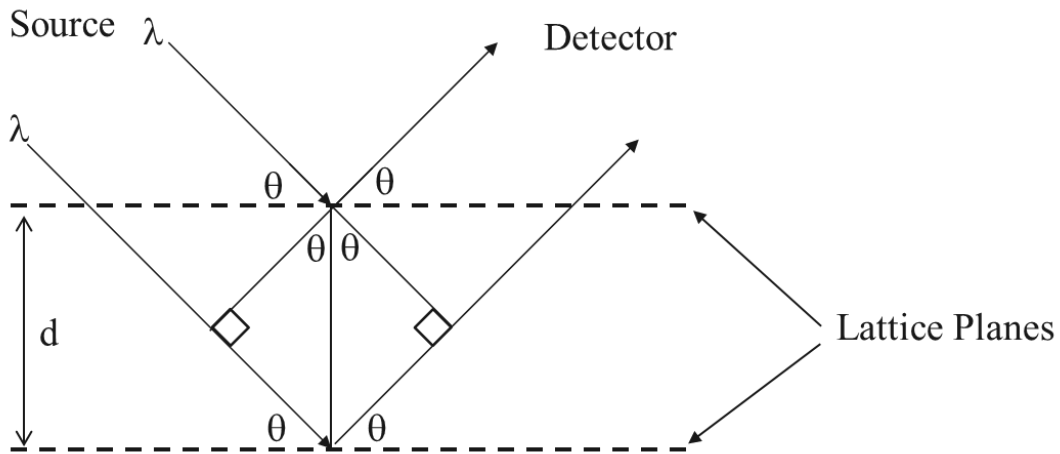


**Figure 2.2** Interaction of X-rays of  $\lambda$  wavelength with a parallel set of planes with lattice spacing  $d$  by two different paths and incident angle  $\theta$ .

According to Bragg's Law, constructive interference between waves of light in two pathlengths results in a maximum intensity depending on the incident angle of the X-ray intersecting the plane of atoms ( $\theta$ ), the X-ray's wavelength ( $\lambda$ ), and the distance between the planes ( $d$ ). Distance between planes is also commonly referred to as the d-spacing or lattice spacing of planes. The  $n$ -th intensity maximum occurs at  $n\lambda = 2d(\sin\theta)$  with  $n$  equal to an integer.<sup>93</sup> There is more than one maxima because the waves from two pathlengths will be in phase as long as the pathlengths differ by an integer number of  $\lambda$ .

Due to the dependence of Bragg's Law on the incident angle of the X-ray ( $\theta$ ), and the random orientation of crystals in a powdered sample, the  $\theta$  is scanned through a range to obtain a spectrum. To do this, the sample stage could simply be tilted through a range of angles, but to avoid disturbance of the sample, common setups actually move the source beam and the detector in tandem as if revolving partially around the stage. The detected X-ray intensities are commonly plotted relative to  $2\theta$ , and these are compiled in reference libraries according to compound and crystal type. The d-spacing between planes depends on the interatomic spacing and arrangement of atoms in the crystal type. The peak intensities depend on the element type, because heavier atoms have more electrons and scatter X-rays more efficiently, and the symmetry of the unit cell. Thus, the combination of composition and structure type of a material results in a unique diffraction pattern that can be catalogued for comparison.

The size of the crystal, or crystallite size, also has an impact on the diffraction pattern. For bulk materials, a particular plane will be regularly repeated with the same d-spacing many times. Each repetition will contribute intensity when conditions are correct for constructive interference according to Bragg's Law. For instance, if the angle is correct for constructive interference by Bragg's Law for two consecutive planes, planes 1 and 2, then the pathlength

from a third plane would also interfere constructively because the d-spacing is doubled, and n is an integer; therefore,  $n\lambda = 2*(2d)(\sin\theta)$  would hold true simply by doubling n. This will work for each parallel plane. Consider that, if n=1 in Bragg's Law, then the diffracted light from plane 1 would interfere constructively with a plane at d angstroms away, or 2d (n=2) angstroms away, or 3d (n=3), and so on. This will increase the signal intensity at the  $\theta$  for constructive interference at the particular d-spacing of the lattice planes. Lattice imperfections, especially lattice strain at the surfaces of the material, will slightly change the d-spacing and lead to peak broadening. The same effect is observed for nanocrystals, where there are insufficient planes to ensure perfect destructive interference around  $\theta$ . Thus, the shape of the X-ray peak is dependent on the size of the crystallite perpendicular to the plane of atoms responsible.

The Scherrer equation allows estimation of the crystallite size based on a diffraction peak, and can differ depending on the peak chosen due to anisotropic growth. The Scherrer equation is  $\tau = \alpha\lambda (\beta\cos\theta)^{-1}$  and relates the crystallite size ( $\tau$ ) to the wavelength of the X-ray ( $\lambda$ ), the Full Width at Half Maximum (in radians) of the peak ( $\beta$ ), and  $\theta$ . The  $\alpha$  is the shape factor, which varies from 0.89 for spherical crystallites to 0.94 for cubic crystallites. Crystallite sizes are estimated in this work using the Jade 5.0 software to assign  $\alpha$  and apply the Scherrer equation. It should be noted that for nanocrystals, the estimation of the crystallite size assumes that the entire particle is one crystal, and does not include amorphous regions on the surface. Therefore, the estimated size is often smaller than that observed by TEM for monodisperse samples.

**2.2.4. Elemental Analysis.** Elemental analysis is carried out on the tetrahedrite and PbTe-based materials by Inductively Coupled Plasma Optical Emission Spectroscopy (ICP-OES) to determine the composition prior to hot-pressing. Samples are prepared by grinding into a

powder to obtain a representative sample. The powder (~14 mg) is precisely weighed on a microbalance and dissolved in a combination of concentrated hydrochloric and nitric acids consisting of 10 ml nitric acid and 30 ml hydrochloric acid. Once digested, the resulting solution is diluted with de-ionized water to 500 mL in a volumetric flask. Analysis is carried out by a Horiba Ultima ICP-OES. For the tetrahedrite doped in-situ with zinc (discussed in Chapter 5) analyte solutions are prepared as above, but analysis is carried out using Inductively Coupled Plasma Mass Spectroscopy (ICP-MS) with an Agilent Technologies 7700 Series ICP-MS.

In ICP-OES, the analyte solution is atomized by the ICP torch. The electrons of each element are constantly being excited followed by relaxation through release of photons. Since the elements are atomized, the wavelengths of emitted photons depend on the element present and its electronic transitions. The instrument is set to detect the characteristic wavelengths of the analyte elements. Calibration standards are prepared from stock solutions of the ionized analytes. These are used first to calibrate the detector for the expected wavelengths. The detector scans a range of wavelengths with high resolution (0.1 nm) around that expected for an analyte. Then, the wavelength with the highest signal is chosen for that element. Once this has been repeated for each analyte, the calibration standards are used to plot calibration curves as signal versus concentration for each analyte. Finally, the unknown solution, formed by digesting the sample, is atomized by the ICP torch and emissions at selected wavelengths are used to determine concentrations of the analyte elements. The relative concentration detected determine the composition of the original sample.

For ICP-MS, samples are again atomized by the ICP torch. Subsequently, these are carried by a flow gas into the mass spectrometer. Due to ionization of the atoms by the torch, they are separated due to mass to charge ratio and detected. Similarly to ICP-OES, calibration

standards are used to develop calibration curves relating signal to concentration. The relative concentrations detected in the unknown solution, prepared by digesting the sample, are then used to determine the composition of the sample.

**2.2.5. Thermoelectric Characterization.** For the PbTe-based samples, hot-pressing is carried out at 70 MPa by heating to 330 °C and maintaining the temperature for 15 minutes before allowing the sample to cool naturally. The inner diameter of the die is 10 mm, and results in a disk approximately 3.6 mm thick. The density of the disk is determined to be at least 90% of the theoretical density of PbTe.

A diamond saw is used to cut a rectangular parallelepiped of approximately 3x3x7 mm<sup>3</sup> from the hot-pressed disk. The 3x3 mm<sup>2</sup> dimensions are for the area (A) of the end of the pipe as illustrated (Figure 2.3), and 7 mm is the length. Thermoelectric measurements are taken under high vacuum over a temperature range of 220 K to 350 K using standard steady state techniques in a cryostat isolated by continuous liquid nitrogen flow.<sup>92</sup> Radiation losses of the parallelepipeds are calculated based on the thermal conductivity of a Pyrex glass standard. The radiation loss is corrected for in the sample by an empirical formula governed by the Stefan–Boltzmann law,  $P=A\sigma T^4$ , wherein  $P$  is the power irradiated from the sample,  $A$  is surface area,  $\sigma$  is the Stefan–Boltzmann constant, and  $T$  is the temperature. The error in electrical and thermal conductivity measurements is estimated to be 5%.

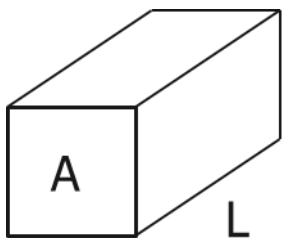


**Figure 2.3** A parallelepiped with an area at the end of A and a length of L.

The cryostat setup contains multiple tools for measurement of thermoelectric properties (Figure 2.4). Properties are measured over a temperature range, and the average temperature is adjusted using a resistor.<sup>92</sup> Voltage is applied to a resistor ( $800 \Omega$ ) at one end of the sample to generate heat. The voltage to the resistor is drained by copper foil to prevent it from flowing through the sample. A thermocouple at each end of the parallelepiped records temperature at that end. These temperatures are different due to the low thermal conductivity of the sample. Once the average temperature reaches the target, it is allowed to equilibrate for several minutes, the applied voltage to the resistor is temporarily turned off so that electrical properties can be measured.

The voltage drop across the length of the parallelepiped is recorded using the  $V^+$  and  $V^-$  electrodes. The difference in voltage between the two ends of the parallelepiped is used with the difference in temperature to determine the thermopower ( $\alpha$ ) according to the equation  $\alpha = -\Delta V/\Delta T$ . Then, a current is applied by the  $I^+$  electrode and drained by the  $I^-$  electrode. The resulting voltage is measured across the  $V^+$  and  $V^-$  electrodes according to the four probe method.<sup>92</sup> The thermopower voltage,  $\alpha\Delta T$ , can contribute to the voltage measured,  $V_{tot}$ , in addition to the voltage due to applied current,  $V_{IR}$ , by the equation  $V_{tot}=V_{IR} + \alpha\Delta T$ . To cancel the thermopower contribution, the voltage drop is measured while the current is applied from the  $I^+$  electrode to the  $I^-$  electrode, and then vice versa. This way,  $V_{IR}$  can be calculated as  $V_{IR} = \frac{V(I^+)+\alpha\Delta T-[V(I^-)+\alpha\Delta T]}{2}$ . Resistance,  $R$ , is calculated according to Ohm's Law by the equation  $R = V_{IR}/I$ , with  $V$  being voltage and  $I$  being current. The resistance of the sample is used to calculate the resistivity ( $\rho$ ), as  $\rho = R*A/L$ , where  $R$  is the resistance in ohms,  $A$  is the area of the square face of the parallelepiped, and  $L$  is its length. Once these measurements are complete, the sample is heated to the next target temperature and the measurements are repeated.

For the thermal conductivity, the voltage to the resistor is converted to power,  $P$ , by  $P=VI$ . This is used with the cross sectional area,  $A$ , the difference in temperature measured by the thermocouples,  $\Delta T$ , which are separated by distance  $L$ , to calculate the thermal conductivity,<sup>92</sup>  $\kappa_{\text{tot}}$ , with the equation  $\kappa_{\text{tot}} = \frac{VI \times L}{\Delta T \times A}$ .

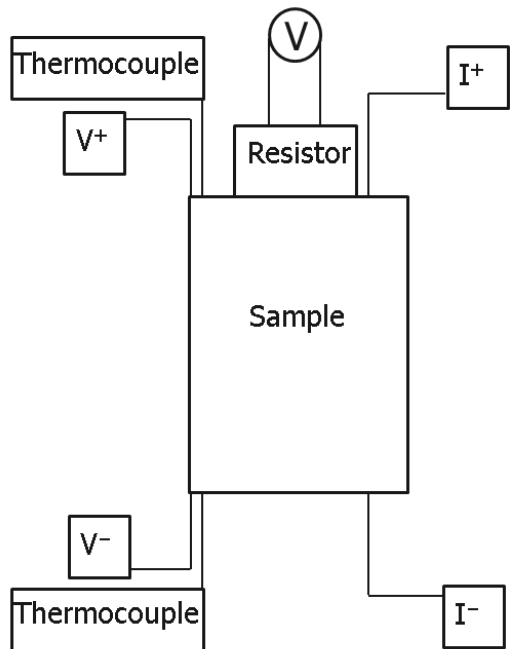


**Figure 2.4** The schematic setup for measuring electronic properties of the parallelepiped is displayed. Electrodes for applying current ( $I^+$  and  $I^-$ ) and the voltage ( $V^+$  and  $V^-$ ) by the four probe method are labeled. Thermocouples are attached at each end. A resistor is used to apply heat.

Preparation of rectangular parallelepipeds of the tetrahedrite requires different conditions. The tetrahedrite is hot-pressed under 80 MPa of pressure at 430 °C for 30 minutes before allowing it to cool naturally. This forms a 4.5 mm thick disk (10 mm in diameter) that exhibits at least 95 % of the theoretical density of tetrahedrite. A disk shaped portion of this sample is removed by a diamond saw for use later in determining the thermal conductivity at high temperature. Rectangular parallelepipeds (approximately 3 x 3 x 7 mm<sup>3</sup>) for thermoelectric characterization are cut from the remaining pellet using a diamond saw. Powder XRD analysis is

carried out on the remaining pellet sections to determine the structure and phase purity of the tetrahedrite after hot-pressing.

A continuous liquid nitrogen flow cryostat is used to determine the thermoelectric properties of the tetrahedrite near room temperature as described for characterization of the PbTe. For high temperature measurements (~350 – 720 K) on the parallelepipeds the thermopower and electrical resistivity are measured using the Ulvac ZEM-3 Seebeck Coefficient/Electric Resistance Measuring System. Unlike the cryostat used near room temperature and below, the Ulvac ZEM-3 can controllably adjust the temperature of the sample and measure properties up to 1073 K. This system employs an Infrared Gold Image Heating Furnace that uses an Infrared lamp as the main heat source. A microheater is used to establish a temperature difference by heating one end of the sample. The instrument provides automated measurement of the voltage difference and application of current through a set of electrodes as illustrated in Figure 2.4. The resistance is calculated by application of the 4 probe method as described previously.

The separate disk (ca. 10 mm diameter by 1 mm thick) cut from the same hot-pressed pellet as the parallelepiped is tested for thermal conductivity. The thermal diffusivity (D), sample density (at room temperature), and the specific heat ( $C_p$ ) are used to calculate the thermal conductivity ( $\kappa_{tot}$ ) using the equation  $\kappa_{tot}=D*\text{density} \cdot C_p$ . The laser flash technique is employed using a Netzsch LFA457 to measure the high temperature thermal diffusivity. The Netzsch LFA457 instrument consists of a furnace equipped with a laser as a secondary heat source, a thermocouple, and an infrared detector. The furnace adjusts the starting temperature of the disc, and this is measured by the thermocouple. Then, the flat (front) side is irradiated by a short energy pulse. The temperature is monitored on the back side by the infrared detector. The

temperature on the back side will increase from the starting temperature to a maximum ( $\Delta T$ ).

The time taken to reach half of  $\Delta T$  is  $t_{1/2}$ . The diffusivity (D) is calculated from  $t_{1/2}$  and the sample thickness (d) by the equation  $D = 0.1388 \times d^2 / (t_{1/2})$ .

The specific heat capacity of the material is determined using a Netzsch DSC200F3 for differential scanning calorimetry (DSC) on a scrap piece of the pellet left after cutting the disk and the parallelepiped. The Netzsch DSC200F3 has a reference crucible and a sample crucible mounted on a stage inside of a furnace. Each crucible holder is equipped with a thermocouple for measurement of temperature. The furnace is heated to increase the temperature of the reference crucible at a constant rate. The sample crucible will also increase at a constant rate, but the temperature will be lower. The same amount of heat is being delivered to both sides; therefore,  $\Delta T$  is related to the  $C_p$  and mass,  $m$ , by  $\Delta T = mC_p$ . Specific heat values for these samples agree with the Dulong-Petit value for pure  $\text{Cu}_{12}\text{Sb}_4\text{S}_{13}$ . The uncertainties in the thermopower and electrical resistivity values are estimated to be 5%, and the uncertainty in the thermal conductivity is estimated to be 10%.

## 2.3. MATERIALS

### 2.3.1. Materials for the Synthesis and Ligand Stripping of PbTe and PbS

**Nanocrystals.** The following chemicals were obtained from Aldrich Chemicals: hexamethyldisilathiane (TMS, synthesis grade), lead(II) acetate trihydrate (puriss ACS reagent grade), tellurium (99.8% trace metals basis), 1-octadecene (ODE, technical grade), oleic acid (OA, technical grade), and tetrabutylammonium iodide (TBAI, 98%). The following chemicals were obtained from Strem Chemicals: lead oxide (99.999+%), tri-*n*-octylphosphine (TOP, min. 97%), and ammonium sulfide (20% aqueous solution). The following chemicals were obtained

from Fisher Chemical: acetone and hexanes (Certified ACS grade). Ethanol (200 Proof) was obtained from Decon Laboratories, Inc., and methanol (ACS grade) from EMD Chemicals.

**2.3.2. Materials for the Solvothermal Synthesis of Tetrahedrite.** Antimony(III) sulfate (>95%) and copper(II) nitrate hemi(pentahydrate) (98.0 – 102.0%) were obtained from Aldrich Chemicals. Thiourea (99% min.) and antimony(III) chloride (99.0% min.) were obtained from Alfa Aesar. Copper(I) chloride (99% purified) was obtained from Acros. The zinc(II) nitrate hexahydrate and ethylenediamine (anhydrous) was obtained from Fisher Chemical. Ethanol (200 proof) was obtained from Decon Laboratories, Inc, and concentrated sulfuric acid was obtained from EMD Chemicals. The copper(II) nitrate hemi(pentahydrate) was dried in an oven at 105 °C for two days to result in basic copper nitrate, Cu<sub>2</sub>(OH)<sub>3</sub>NO<sub>3</sub>. The composition of the natural mineral tennantite (designated here as NM) used for mixing was Cu<sub>10.0</sub>Zn<sub>1.8</sub>Fe<sub>0.2</sub>As<sub>2.7</sub>Sb<sub>1.3</sub>S<sub>13</sub>. This was purchased as a mineral specimen from Stefano Fine Minerals, Inc., Ann Arbor, Michigan, USA.

## CHAPTER 3 : DESIGN OF LEAD TELLURIDE BASED THERMOELECTRIC MATERIALS THROUGH INCORPORATION OF LEAD SULFIDE INCLUSIONS OR LIGAND STRIPPING OF NANO-SIZED BUILDING BLOCKS

### 3.1. INTRODUCTION

This chapter describes the multi-gram scale synthesis of dispersible, lead telluride (PbTe) nanocrystals (25–50 nm) using hot-injection methods in common organic solvents and their use to prepare nanostructured thermoelectric material. These nanocrystals (NCs) are ligand stripped with methanol, methanol solutions of ammonium sulfide, tetrabutylammonium iodide, or ammonium sulfide followed by tetrabutylammonium iodide to prepare samples for hot-pressing. In addition, pre-grown lead sulfide NCs (4–6 nm) are combined with the dispersible PbTe NCs by incipient wetness to form a nanocomposite sample. The resulting samples are annealed and then hot-pressed into pellets and characterized for thermoelectric properties. The effects of nanostructuring and ligand stripping on thermoelectric properties are evaluated. The work in this chapter has been published.<sup>95</sup> (Reprinted (adapted) with permission from James, D.; Lu, X.; Nguyen, A. C.; Morelli, D.; Brock, S. L., Design of Lead Telluride Based Thermoelectric Materials through Incorporation of Lead Sulfide Inclusions or Ligand Stripping of Nanosized Building Blocks. *J. Phys. Chem. C* **2015**, *119* (9), 4635-4644. Copyright 2015 American Chemical Society.)

### 3.2. EXPERIMENTAL

**3.2.1. Synthesis of Multi-Gram Scale Lead Telluride Nanoparticles.** A lead oleate precursor is prepared by dissolution of lead acetate trihydrate (4.172 g) in a solution of oleic acid (15.0 mL) and octadecene (50.0 mL) in a Schlenk flask equipped with reflux condensor by first applying vacuum to remove moisture and then heating under argon flow to 170 °C for one hour.

The resulting solution is then heated to 300 °C. The tellurium precursor is prepared by dissolution of elemental tellurium (1.394 g) in TOP (20.0 mL) with heating to 120 °C. The tellurium precursor (18.0 mL) is then injected into the lead oleate precursor. Lead telluride nucleates and is allowed to grow at this temperature for 10 minutes before lowering the temperature to 260 °C for 10 minutes of solution-phase annealing. This solution-phase annealing step serves to improve the composition ratio of the nanocrystals, which is otherwise very tellurium rich. The mixture is then removed from heat and allowed to cool naturally. The particles are isolated by rinsing into centrifuge tubes with hexane, flocculating with acetone, and centrifuging. The pellets are then washed by sonication in acetone, followed by centrifugation and drying. The product may be re-dispersed in hexanes for characterization by Transmission Electron Microscopy (TEM).

**3.2.2. Synthesis of Lead Sulfide NCs (4–6 nm) Following the Work by Hines and Coworkers.<sup>96</sup>** A mixture of lead oxide (0.450 g), OA (1.5 mL) and ODE (18.5 mL) is heated to 110 °C under vacuum with stirring. After 15 minutes, argon is introduced, and the temperature is adjusted to 150 °C and maintained until a translucent yellow solution is obtained. The sulfur precursor is prepared by adding 0.21 mL of TMS to 10 mL of ODE, and subsequently injected into the lead oleate precursor solution. The mixture is allowed to cool naturally after 10 minutes of growth, and then isolated by precipitating with ethanol. The product is washed three times by redispersing in hexane and precipitating with ethanol.

**3.2.3. Ligand Stripping with Sulfide<sup>67</sup> or Iodide.<sup>68</sup>** Approximately 1.5 g of lead telluride NCs are sonicated in 20 mL of 0.040 M ammonium sulfide or TBAI, respectively, in methanol for 20 minutes and then washed by sonicating in methanol several times. For the sample first stripped with sulfur followed by iodide, the same procedure is followed, but the

ligand stripping is performed consecutively, including methanol washes between sulfur stripping and iodide stripping. Each sample is then placed individually in an annealing-tube and purged with argon for at least 10 minutes. The argon flow is stopped to avoid loss of tellurium while heating (a bubbler prevents backflow of air). The temperature is raised to 300 °C at 10 °C per minute and held at 300 °C for 15 minutes to anneal the sample and help ensure removal of solvent. The tube is then sealed to allow the sample to cool naturally in the argon atmosphere.

**3.2.4. Preparation of the Nanocomposite of Lead Sulfide and Lead Telluride (PbTe-PbS).** Lead sulfide and lead telluride are weighed out in proportion to result in 8 mol% lead sulfide when mixed. The lead sulfide is dispersed as a colloidal solution in hexane and mixed with the lead telluride by incipient wetness under an inert atmosphere by adding 1–2 mL increments of lead sulfide colloid solution in hexanes to the lead telluride NCs resulting in a slurry, then grinding dry in a mortar and pestle. The sample is annealed by the same procedure described for the ligand stripped samples.

### 3.3. RESULTS AND DISCUSSION

**3.3.1. Synthesis and Characterization of PbTe Nanocrystals.** In order to prepare suitable quantities of material (ligand-stripped PbTe or PbTe/PbS nanocomposite) for thermoelectric measurements (ca 2 g samples), a large-scale synthesis of PbTe nanocrystals is needed. While such quantities of PbTe can be obtained by microwave syntheses, they consist of either micrometer-scale dendrites<sup>97</sup> or aggregates<sup>98</sup> unsuitable for mixing. Similarly, the lack of ligands in ball-milled PbTe ingots and the generally larger size of the resulting particles is expected to inhibit dispersal in solvents for homogeneous mixing with PbS NCs.<sup>11,63,12</sup> Relatively small, dispersible PbTe NCs can be prepared by solution-phase arrested precipitation in the presence of surface binding agents (ligands), but only in small quantities<sup>6</sup> suitable for thin

films<sup>5</sup> for which thermal conductivity measurements are not feasible.<sup>64,5,55</sup> Thus, to provide suitable quantities of lead telluride NCs for thermoelectric measurements in a practical manner, a multigram scale synthesis of dispersible, 25–50 nm lead telluride NCs was developed using standard Schlenk line techniques and common solvents. Briefly, lead acetate is dissolved in oleic acid and octadecene at 300 °C, at which point a solution of trioctylphosphine telluride is introduced by rapid injection, followed by annealing at 260 °C. This new method routinely produces 1–2.5 g of product per synthesis (Figure 3.1).

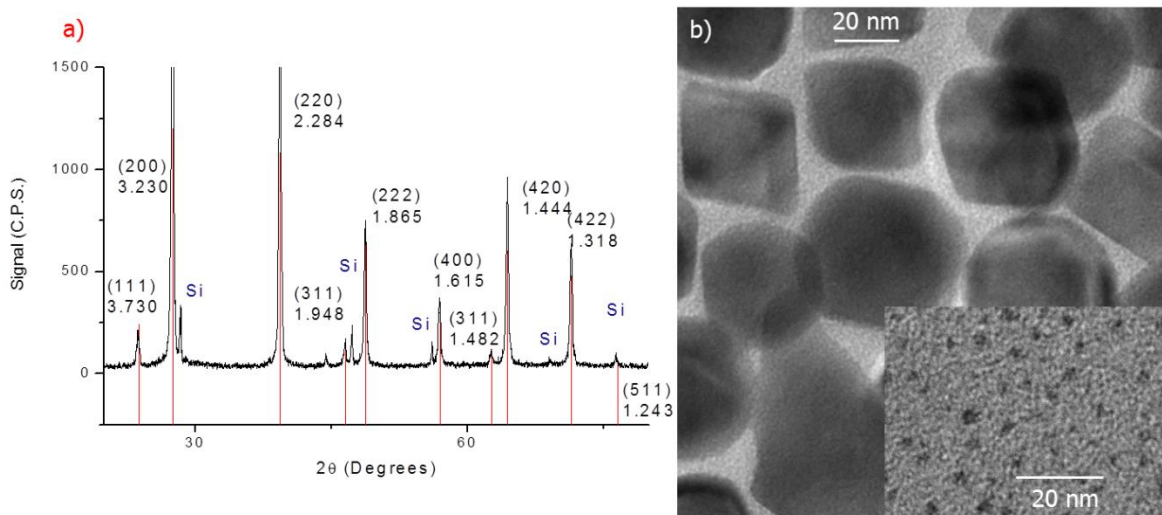


**Figure 3.1** (a) XRD data for lead telluride NCs. Silicon is present as an internal standard. The reference pattern for PbTe is shown (red lines), and the peak indices and *d*-spacings are indicated. (b) TEM micrograph of lead telluride nanoparticles. The inset shows the presumed 1–2 nm lead oleate clusters.

The crystalline nature of the lead telluride is evident by XRD (Figure 3.1a). The Scherrer size estimate of 30 nm supports the size observed by TEM (ca 20–40 nm, Figure 3.1b). Lead and tellurium are detected in a nearly 1:1 mole ratio (49:51) by energy dispersive X-ray spectroscopy (EDS). The dot-like features in the inset of Figure 3.1b are likely clusters of the lead oleate precursor,<sup>60</sup> as the tellurium to lead mole ratio for these clusters is very low (13:87 by EDS). These features are found at edges of groups of lead telluride nanoparticles, as well as on their own all over the sample grid. Similar features have been observed in previous lead

chalcogenide syntheses in which the lead oleate monomer is prepared as an intermediate product by dissolution of lead acetate in an oleic acid solution.<sup>59-60</sup>

**3.3.2. Ligand Stripping and Nanocrystal Mixing for Annealed Nanocomposites.** In the present work, two strategies are explored for improvement of the thermoelectric properties of lead telluride nanostructures. The first strategy relies on ligand stripping of lead telluride NCs to improve performance in single-component lead telluride nanostructures. Ligand stripping of lead telluride NCs using ammonium sulfide<sup>67</sup> or an iodide source<sup>68</sup> is employed because these ligand removal techniques have been demonstrated to increase  $\sigma$  in thin films of nanocrystals relative to the native ligands resultant from the particle synthesis. The second strategy is to mix lead telluride NCs with lead sulfide NCs to form a homogeneous nanocomposite. The mixed NCs sample is prepared by combining lead telluride nanoparticles with pre-grown lead sulfide NCs, 4–6 nm in diameter (Figure 3.2). Based on prior work on PbTe/PbS nanostructures prepared by spontaneous phase segregation,<sup>10</sup> a concentration of 8 mol % lead sulfide was targeted for achieving maximum ZT.

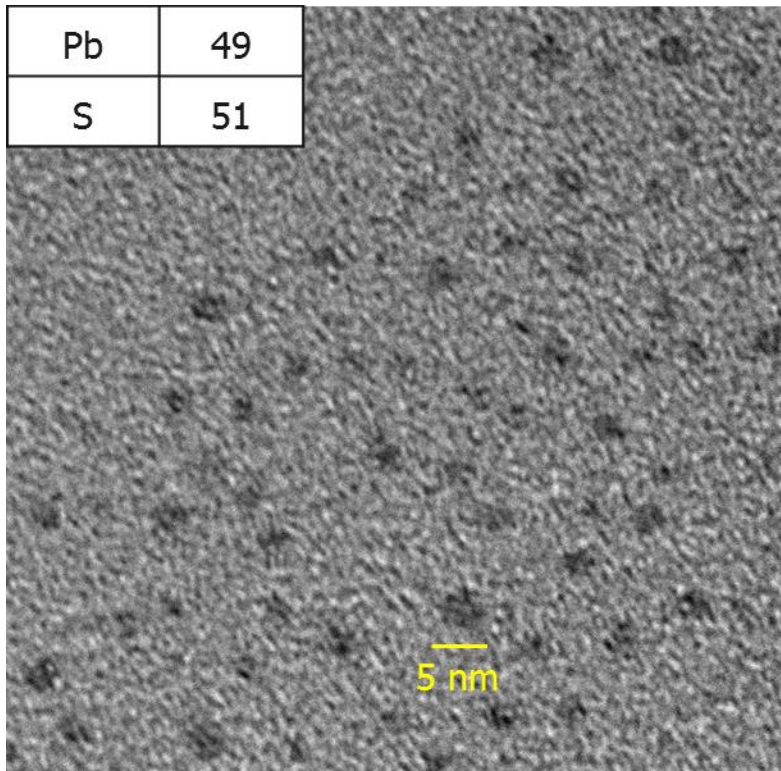


**Figure 3.2** TEM micrograph of lead sulfide NCs as prepared and dispersed in hexane. The composition of the group of NCs was determined by EDS and is displayed as atomic percentages.

The samples prepared include a control consisting of only lead telluride NCs washed with methanol to remove ligands (PbTe), a sulfide stripped sample of lead telluride NCs prepared by washing with ammonium sulfide solution (PbTe-S), a sample stripped consecutively with sulfide and iodide solutions (PbTe-SI), an iodide-stripped sample (PbTe-I), and a composite of lead telluride and lead sulfide NCs mixed by incipient wetness (PbTe-PbS). All samples are annealed under inert atmosphere to remove residual solvents and elemental sulfur generated by the sulfide ligand stripping.

The annealed nanoparticle samples are investigated by XRD (Figure 3.3). All samples exhibited reflections that could be indexed to lead telluride and the crystallite sizes were estimated by application of the Scherrer equation (Table 3.1). The iodide stripping results in 40 nm lead telluride crystallites, with no indication of a crystalline lead iodide phase. Lead telluride

crystallites in PbTe-I exhibited less growth during annealing relative to the 50-90 nm crystallite size observed in all of the other samples, suggesting that iodide is acting to protect the particle surfaces. To our surprise, the PbTe-S and PbTe-SI samples exhibited ca. 60 nm lead sulfide crystallites after annealing in addition to PbTe. PbS formation may be a result of ammonium sulfide reacting with the lead oleate clusters to form lead sulfide during annealing, or the sulfide may be replacing telluride in existing lead telluride crystallites by anion exchange. The substantial growth of lead telluride crystallites in PbTe-S and PbTe-SI during annealing (to 90 and 70 nm, respectively) suggests that sulfide stripping provides mobility for the lead, inducing ripening of lead telluride nanoparticles. In contrast, the growth of lead telluride crystallites in both PbTe-PbS and the control (PbTe) is limited to a Scherrer size of 50 nm upon annealing. Surprisingly, the mixed sample PbTe-PbS exhibits no evidence of crystalline lead sulfide after annealing. This may indicate a larger energy barrier to sintering the pre-grown lead sulfide NCs than to growing lead sulfide NCs from the sulfide stripped samples, PbTe-S and PbTe-SI, and/or that the small amount of PbS in the mixed sample is insufficient to be detected by XRD.

**Table 3.1** Scherrer sizes of lead telluride and lead sulfide crystallites after annealing (a) or hot-pressing (hp), as determined by XRD. Samples include lead telluride that has been iodide stripped (PbTe-I), sulfur stripped (PbTe-S), consecutively sulfur and iodide stripped (PbTe-SI), mixed with lead sulfide (PbTe-PbS), or washed with methanol (PbTe). The sulfur and iodine mole fraction values relative to lead are determined by inductively coupled plasma optical emission spectroscopy (ICP-OES).

Samples	PbTe Size (a)	PbS Size (a)	PbTe Size (hp)	PbS Size (hp)	S : Pb	I : Pb
(PbTe-I)	40 nm	N/A	60 nm	N/A	N/A	0.017
(PbTe-S)	90 nm	60 nm	60 nm	60 nm	0.16	N/A
(PbTe-SI)	70 nm	60 nm	70 nm	70 nm	0.28	0.007
(PbTe-PbS)	50 nm	Undetected	70 nm	40 nm	0.044	N/A
(PbTe)	50 nm	N/A	60 nm	N/A	N/A	N/A

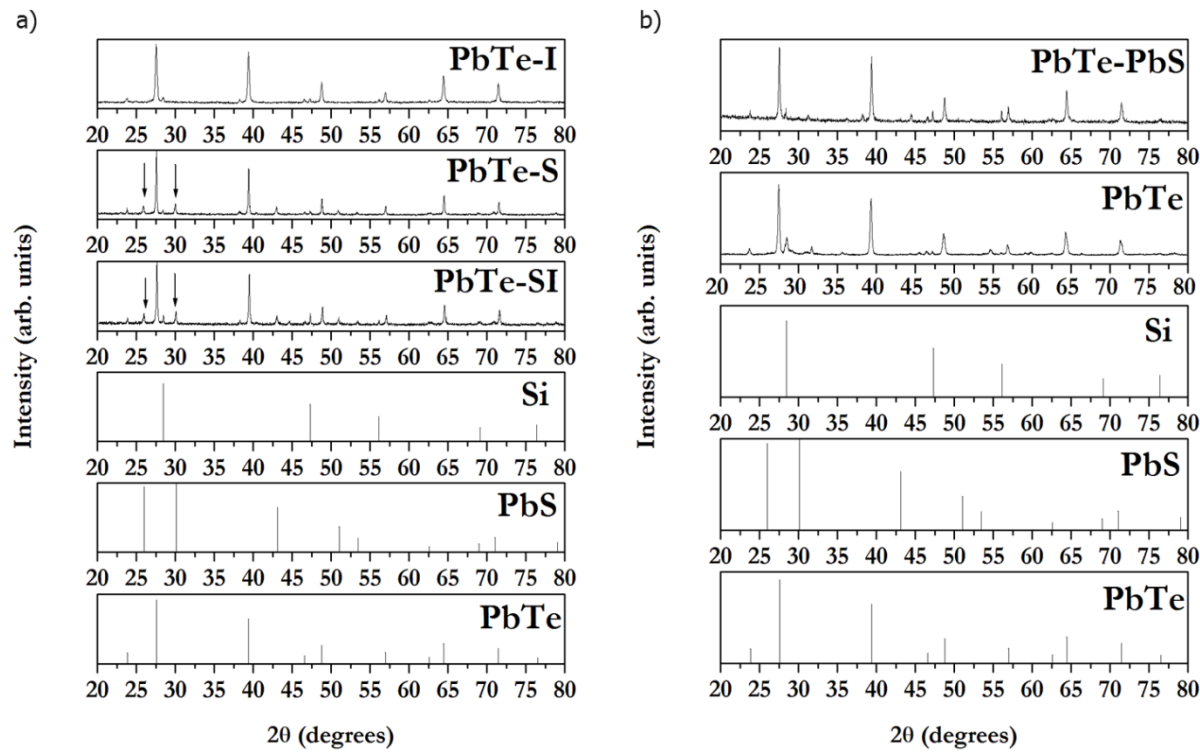


**Figure 3.3** XRD patterns of the iodide stripped (PbTe-I), sulfide stripped (PbTe-S), sulfide and then iodide stripped (PbTe-SI), lead sulfide mixed with lead telluride (PbTe-PbS), and methanol-washed lead telluride (PbTe) samples after annealing shown along with the Powder Diffraction File (PDF) patterns for silicon (internal standard, 27–1402), lead sulfide (78–1057, also indicated by arrows) and lead telluride (77–0246).

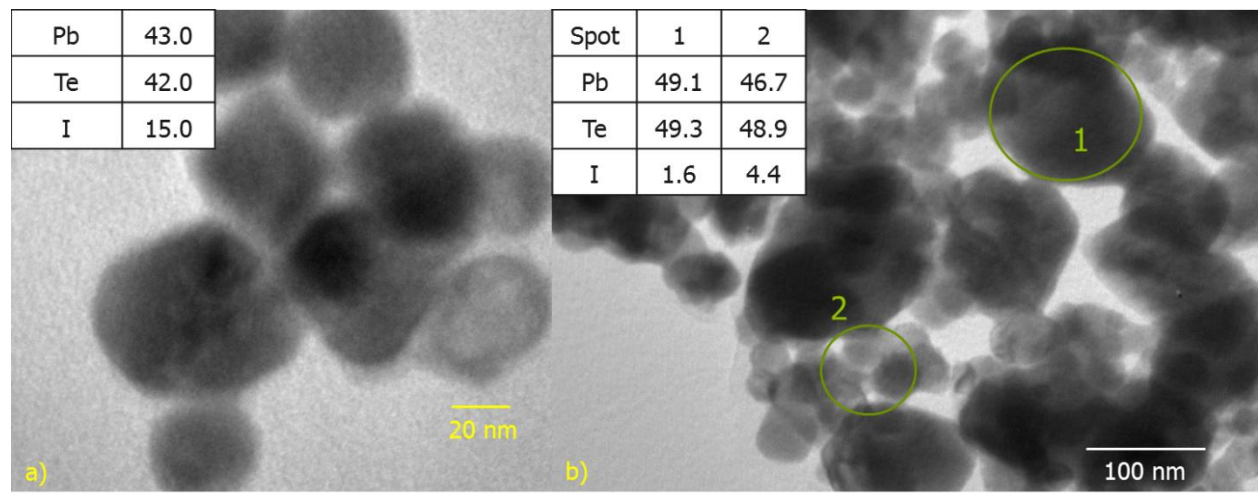


**Figure 3.4** TEM micrographs of lead telluride nanoparticles after iodide stripping (PbTe-I) before (a) and after (b) annealing. Compositions, as atomic percentages, are displayed in the insets.

Electron microscopy sheds light on how the samples are transformed during annealing. For PbTe-I, the aggregates of lead telluride appear much larger in the TEM (hundreds of nanometers) than the Scherrer size of 40 nm, suggesting that they contain multiple crystallites. The composition of sample regions inside particles and at interparticle boundaries is measured by EDS over several regions for comparison. The distribution of iodide becomes heterogeneous after annealing (Figure 3.4). There is about 15 mol % iodine in a wide area before annealing, and it is not matched stoichiometrically by the lead cation, which is determined to be in an approximately 1:1 mole ratio with tellurium (Figure 3.4a). After annealing, most of the iodine has been removed, with just a few percent remaining. The iodine appears to be more prevalent between the aggregates of lead telluride, as exhibited by spot 2 versus spot 1 in Figure 3.4b, suggesting iodide is segregated at the interfaces. These observations are replicated in other regions of the sample (Table 3.2). Iodine is more prevalent between aggregates than inside particles at the 95% confidence level because the confidence intervals do not overlap for the iodine percentage detected in intraparticle and interparticle regions.

**Table 3.2** Average iodine mole percentage for interparticle and intraparticle regions of TEM micrographs of PbTe-I after annealing along with the standard deviations and 95% confidence intervals of the measurements.

	Avg. I mol%	Standard deviation	95% Conf. Int.
Intraparticle	2.0	0.49	0.98 – 2.9
Interparticle	4.4	0.071	4.3 – 4.6

Ligand stripping with sulfide results in a low contrast growth on the lead telluride NCs in PbTe-S, as observed by TEM (Figure 3.5a), suggesting amorphous film formation; however, Moiré fringes suggest a second crystalline phase with different lattice parameters is also growing on the surface of PbTe, most likely PbS. Consistent with this hypothesis, EDS data suggest a decrease in Te relative to Pb and a large excess of sulfur. Presumably, sulfide displaces some telluride at the particle surface, giving rise to PbTe@PbS core@shell crystalline structures along

with an amorphous sulfur species. Annealing at 300 °C removes much of the excess sulfur from the lead telluride NCs, as the sulfur contribution decreases from 17 to 8 mol % for the entire image in Figure 3.5a to Figure 3.5b. This agrees with the removal of excess sulfur from ligand stripped PbS NCs at 300 °C, as reported by Robinson, *et. al.*<sup>67</sup> However, the lead telluride NCs are now sintered, resulting in large, sulfur-rich regions between them like spot 1, with levels of sulfur nearly as high as those of tellurium. These large sulfur-rich regions may be the source of the large lead sulfide crystallites indicated by XRD results.

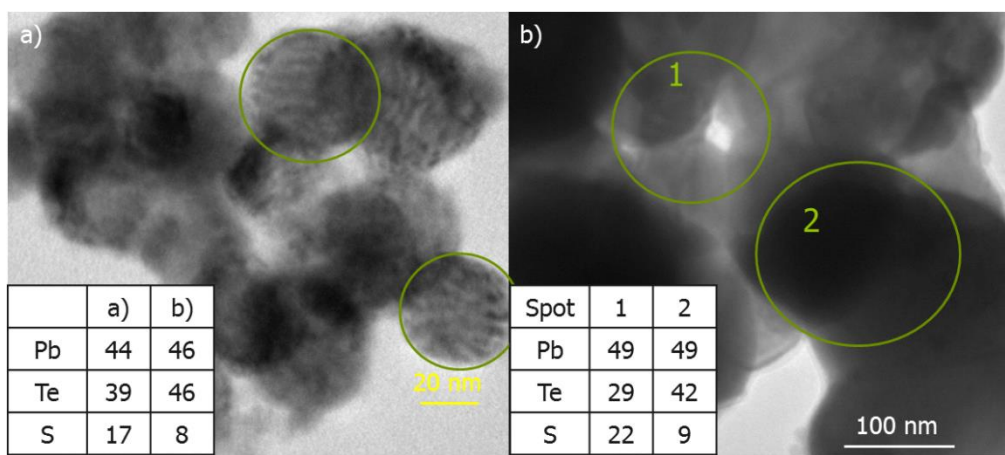


**Figure 3.5** TEM micrographs of the sulfide stripped lead telluride NCs (PbTe-S) before annealing (a), and after annealing (b). EDS results for the images are displayed alongside as atomic percent. Moiré fringes are evident in panel a (circled particles) due to interference patterns from two different lattice dimensions (presumably PbS over PbTe).

Examination of the sample stripped with sulfide and then iodide consecutively, PbTe-SI, reveals similar features to PbTe-S. Specifically, a low contrast growth and Moiré fringes are observed on the lead telluride NCs before annealing along with an anion-rich composition (Figure 3.6a). Annealing greatly decreases the sulfur mol % from 15 to 7.8; however, similarly to PbTe-S, the material after annealing contains large crystallites of lead sulfide as determined by application of the Scherrer equation to the XRD data (Table 3.1), and the material is now very heterogeneous in composition (Figure 3.6b). Between the sintered lead telluride NCs, which exhibit about 6 mol % sulfur, there are sulfur-rich regions with up to 18 mol % sulfur. Iodine is

also detected and decreases during annealing from 2 to 1 mol % for a wide area, with more of it detected (1.3 mol %) between the sintered lead telluride than in or on the lead telluride (0.8 mol %).

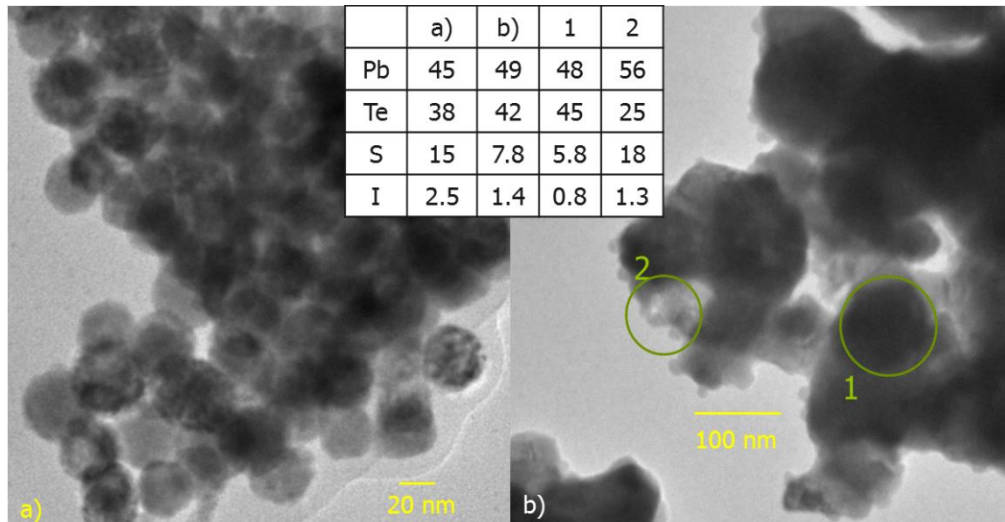


**Figure 3.6** TEM micrograph of lead telluride nanoparticles stripped first with sulfide and then with iodide (PbTe-SI) before annealing (a) and after annealing (b). The compositions determined for the images by EDS are displayed as atomic percentages.

In contrast to samples stripped with ammonium sulfide, evidence for lead sulfide crystallites was not apparent in the XRD pattern for the lead telluride NCs mixed with lead sulfide NCs sample, PbTe–PbS, after annealing at 300 °C. However, sulfur-rich regions are observable in TEM–EDS post-annealing (Figure 3.7), suggesting that PbS inclusions are present. The sulfur content is not uniform throughout the sample (see spot 1 vs spot 2). Thus, the PbS NCs do not appear to be homogeneously deposited on the PbTe in the course of incipient wetness.

Finally, examining the control sample, PbTe, by TEM and EDS after annealing reveals that the smaller crystallites of PbTe (Table 3.1) are severely aggregated in the TEM micrograph (Figure 3.8) compared to their original appearance in Figure 3.1. These aggregates of small crystallites are visually similar to the iodide stripped samples, but have a ratio of exactly 1:1 lead to tellurium by EDS.

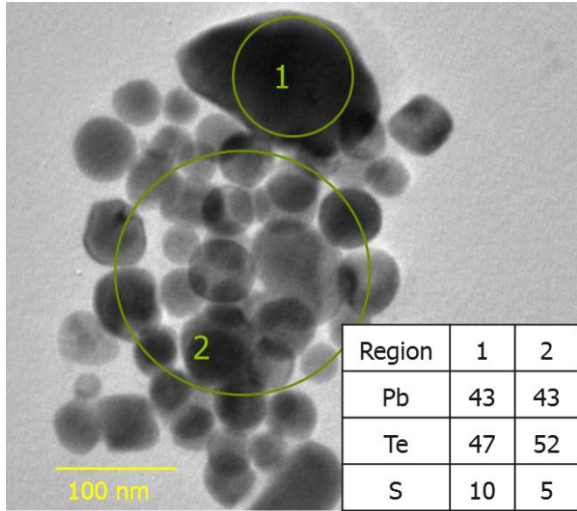


**Figure 3.7** TEM micrograph of mixed lead sulfide and lead telluride NCs (PbTe–PbS) after annealing. The EDS-determined compositions of two regions are displayed as atomic percentages.

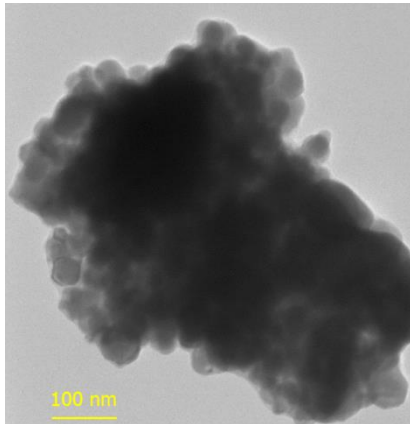


**Figure 3.8** TEM micrograph of the control sample of methanol-washed lead telluride NCs (PbTe) after annealing

Meaningful measurement of thermoelectric properties is most easily attained on large-scale (grams) dense samples. Accordingly, the annealed samples were hot-pressed at 330 °C under 2000 psi to produce pellets from which samples can be cut of appropriate geometry for measurement of  $\alpha$ ,  $\sigma$  and  $\kappa$ . In order to probe the effect of hot-pressing on nanoparticle sintering, all samples were probed by XRD (Figure 3.9).

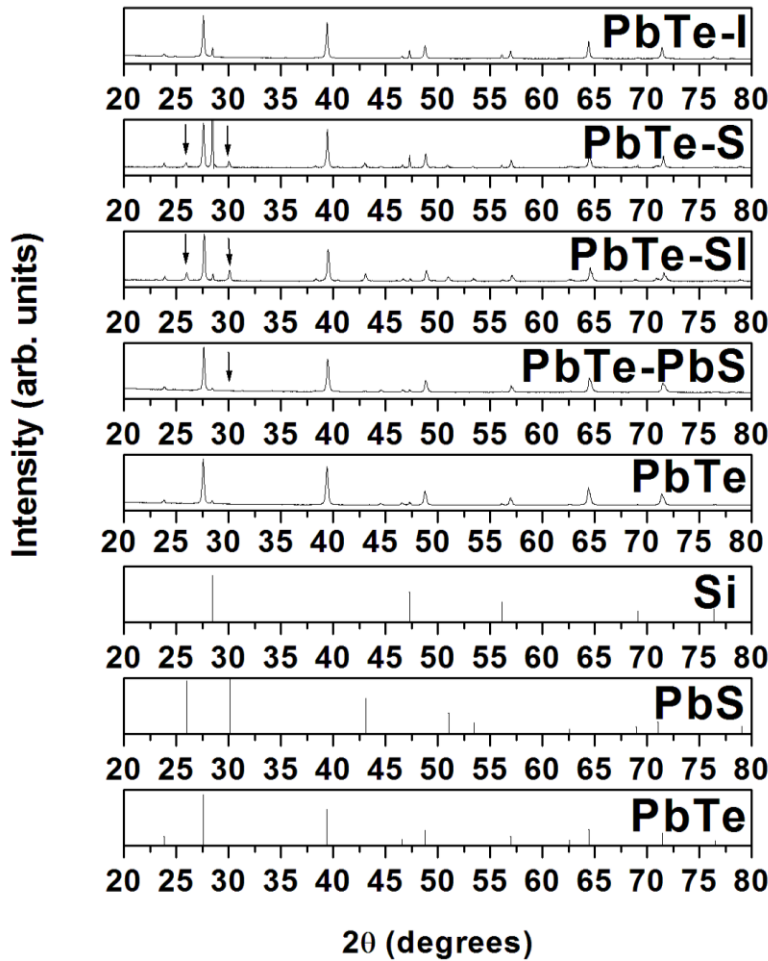


**Figure 3.9** XRD spectra of the iodide stripped (PbTe-I), sulfide stripped (PbTe-S), sulfide, then iodide stripped (PbTe-SI), and methanol stripped (PbTe) lead telluride as well as lead sulfide NCs mixed with lead telluride NCs (PbTe-PbS) samples after hot-pressing are shown along with the PDF files 27-1402 for silicon, 78-1057 for lead sulfide (arrows), and 77-0246 for lead telluride.

While the lead telluride crystallites in the iodide stripped sample, PbTe-I, did not sinter during annealing, they did exhibit growth during hot-pressing (from 40 to 60 nm, Table 3.1). Iodine is detected in this sample, with 1.7% iodine relative to lead (Table 3.1), which is much higher than the iodine composition in the phase-segregated sample prepared by the Kanatzidis group (0.110% iodine relative to lead).<sup>10</sup> The lead telluride crystallites in the PbTe-S and PbTe-SI samples exhibit the same Scherrer size after hot-pressing as after annealing; the lead sulfide crystallites in PbTe-S were also unchanged after annealing, whereas they grew slightly, to 70

nm, for PbTe-SI. Therefore, for the sulfide stripped samples, most the crystallite growth occurred during the annealing step, leaving their sizes stable for the hot-pressing step. In contrast, the mixed sample, PbTe–PbS, exhibited quite the opposite behavior. While the PbTe–PbS sample did not exhibit any lead sulfide phase after annealing, indicating that the incorporated lead sulfide NCs did not sinter, crystalline lead sulfide is apparent after hot-pressing, and can be modeled as particles with a Scherrer diameter of 40 nm (Table 3.1). By comparison, this is still smaller than the 60 nm Scherrer size for crystallites in the hot-pressed PbTe-S sample (Table 3.1). This may suggest that starting with pre-grown lead sulfide NCs results in growth of smaller lead sulfide crystallites than ligand stripping with sulfide. However, the sulfide stripped samples contain ca. 4x more sulfur than the mixed sample relative to Pb (Table 3.1), so it may be that the amount of PbS present is the determiner of crystallite size after hot-pressing. Investigating the control sample, PbTe hp, by XRD reveals that the lead telluride crystallites grow to about 60 nm during hot-pressing even without any ligand stripping or sulfide present. Therefore, the size of the lead telluride crystallites is fairly consistent among all samples after hot-pressing, at 60–70 nm in diameter.

**3.3.3. Thermoelectric Characterization of Hot-Pressed Nanocomposites.** The hot-pressed materials were characterized with respect to their thermoelectric properties over the temperature range 220–350 K. A compilation of room-temperature thermoelectric properties for all measured samples is displayed in Table 3.3 for comparison.

**Table 3.3** Thermoelectric properties of the hot-pressed samples at room temperature.

Hot-pressed (hp) Sample	$\alpha$ ( $\mu\text{V K}^{-1}$ )	$\sigma$ ( $\text{S cm}^{-1}$ )	$\kappa_{\text{Lat}}$ ( $\text{W m}^{-1}\text{K}^{-1}$ )	ZT
PbTe-I	-540	0.01	0.87	$1 \times 10^{-4}$
PbTe-S	520	0.97	1.2	0.007
PbTe-SI	-39	0.12	1.7	$3 \times 10^{-6}$
PbTe-PbS	-160	42	1.3	0.03
PbTe	-210	3.2	1.4	0.003

The temperature-dependence of the Seebeck coefficients is displayed in Figure 3.10a. For the ligand stripped samples (S, I, or SI) doping by sulfide and by iodide during the ligand stripping process is reflected in the data. Iodine has one more electron per anion than tellurium; therefore, substitution of iodine for tellurium provides additional electrons, and they can easily be excited to the conduction band and serve as additional negative carriers. Thus, PbTe-I hp is an *n*-type material with a large negative Seebeck coefficient at room temperature ( $-540 \mu\text{V}\cdot\text{K}^{-1}$ ). This thermopower is 70% larger than the  $-320 \mu\text{V}\cdot\text{K}^{-1}$  observed by Fang, *et. al.* for their most electrically conductive film of iodine-doped (5.05%) PbTe NCs<sup>5</sup> and 170% larger than the thermopower observed by Cao, *et. al.* for a pellet of relatively large, un-doped PbTe particles.<sup>13</sup> In contrast, substitution of tellurium with sulfur results in a *p*-type material because the band gap of lead sulfide is larger, and the valence band of lead sulfide is lower in potential energy than that of lead telluride, allowing lead sulfide to accept electrons from lead telluride. In the present case, doping is combined with formation of phase segregated lead sulfide crystallites. Not surprisingly, the sulfide stripped sample, PbTe-S hp, demonstrates a high, positive Seebeck coefficient of  $520 \mu\text{V}\cdot\text{K}^{-1}$  at room temperature, consistent with *p*-type doping. This thermopower is higher than that reported for the hydrazine treated film of PbTe wires ( $410 \mu\text{V}\cdot\text{K}^{-1}$ )<sup>53</sup> by Yan, *et. al.* but lower than those reported for nanowires washed with ethanol ( $628 \mu\text{V}\cdot\text{K}^{-1}$ )<sup>53</sup> by Yan, *et. al.* but lower than those reported for nanowires washed with ethanol ( $628 \mu\text{V}\cdot\text{K}^{-1}$ )<sup>53</sup> by Yan, *et. al.*

$\mu\text{V}\cdot\text{K}^{-1}$ )<sup>54</sup> or for a pellet of 30 nm PbTe grains enhanced by oxide boundaries for carrier filtering ( $625 \mu\text{V}\cdot\text{K}^{-1}$ ).<sup>6</sup> For the samples subjected to both sulfide and iodide stripping (PbTe-SI hp) the effects of counter-doping are evident, resulting in a small, negative Seebeck coefficient.

When PbTe and PbS NCs are hot-pressed to form a composite (PbTe–PbS hp), an *n*-type material with a Seebeck coefficient of  $-160 \mu\text{V}\cdot\text{K}^{-1}$  is obtained. This is considerably larger than the  $-100 \mu\text{V}\cdot\text{K}^{-1}$  recorded at room temperature for the 8 mol % lead sulfide composite in the previous work by the Kanatzidis group using iodide-doped PbTe,<sup>10</sup> but on par with a nanostructured pellet of PbTe.<sup>13</sup> The Seebeck coefficient for the PbTe–PbS hp sample is somewhat smaller in magnitude than that for the methanol-washed hot-pressed PbTe sample (also *n*-type), suggesting that PbS nanoparticles are injecting holes into the inherently *n*-type PbTe and annihilating excess electrons. Carrier injection from differing NCs has also been reported by Urban, *et. al.* in a composite film of PbTe and Ag<sub>2</sub>Te NCs where the Ag<sub>2</sub>Te NCs served as a source of holes for *p*-type doping.<sup>55</sup>

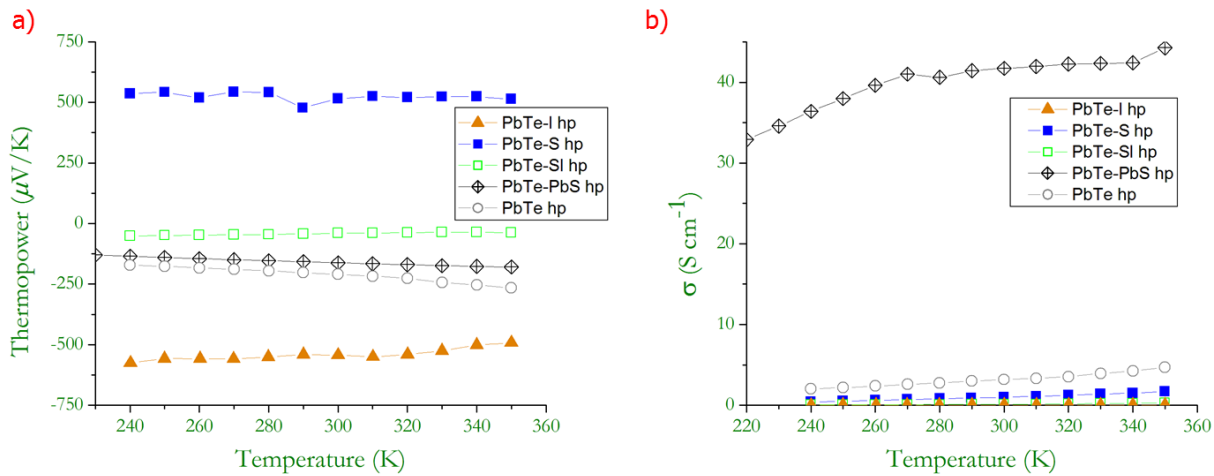


**Figure 3.10** Temperature-dependent Seebeck coefficient (a) and electrical conductivity (b) values of hot-pressed samples.

Ligand stripping was expected to lead to increased electrical conductivity, based on reports for thin films, because removal of the insulating ligands from the nanoparticles results in

better contact between their interfaces.<sup>5,55,67,68,53</sup> Electrical conductivity data are shown in Figure 3.10b. The electrical conductivity of all of the ligand stripped samples is decreased compared to the control,  $3.2 \text{ S}\cdot\text{cm}^{-1}$  for PbTe hp at 300 K, which is itself at the very low end of electrical conductivity for bulk lead telluride.<sup>12</sup> The behavior of PbTe hp is expected due to the lack of intentional doping and the nanocrystalline nature of the pellet sample. Nevertheless, PbTe hp actually exhibits higher electrical conductivity than hydrazine treated thin films of iodine doped NCs ( $0.4 \text{ S}\cdot\text{cm}^{-1}$ )<sup>5</sup> and has a value similar to  $\sigma$  observed for a film of hydrazine treated PbTe nanowires ( $\sim 5 \text{ S}\cdot\text{cm}^{-1}$ )<sup>53</sup> or a composite film of hydrazine treated PbTe and  $\text{Ag}_2\text{Te}$  NCs ( $4.8 \text{ S}\cdot\text{cm}^{-1}$ ),<sup>55</sup> although these values are still much lower than the  $\sim 210 \text{ S}\cdot\text{cm}^{-1}$  achieved by a pellet of relatively large particles from a ligand free synthesis.<sup>13</sup> For much higher electrical conductivities, intentional doping with 0.055 mol % lead(II) iodide in solid state synthesis can adjust the number of carriers to approximately  $5.0 \times 10^{18} \text{ cm}^{-3}$  with a corresponding carrier mobility of up to  $1.5 \times 10^3 \text{ cm}^2\cdot\text{V}^{-1}\text{s}^{-1}$  for an electrical conductivity of  $1200 \text{ S}\cdot\text{cm}^{-1}$ .<sup>10</sup> However, doping in the current work is not well controlled and leads to a surprising decrease in conductivity for the ligand stripped samples. For PbTe-S hp, the PbTe is doped with sulfur, yielding the large, positive Seebeck coefficient. Too much sulfur dopant results in too many holes as carriers, leading to a decrease in mobility and decreased electrical conductivity ( $0.97 \text{ S}\cdot\text{cm}^{-1}$ ) at room temperature. A similar phenomenon occurs in the iodide stripped sample, PbTe-I hp, where there are too many electron carriers, resulting in low electrical conductivity ( $0.01 \text{ S}\cdot\text{cm}^{-1}$ ) as well as in counter-doped samples (PbTe-SI,  $0.12 \text{ S}\cdot\text{cm}^{-1}$ ).

PbTe–PbS hp demonstrated the highest electrical conductivity in this work ( $42 \text{ S}\cdot\text{cm}^{-1}$  at 300 K). The addition of PbS decreases the number of carrier electrons leading to the smaller Seebeck coefficient and the increased electrical conductivity of PbTe–PbS hp compared to the

control (PbTe hp). The resulting trends of increasing electrical conductivity and a smaller Seebeck coefficient were also documented by the Kanatzidis group as they increased the mole percentages of lead sulfide in their *n*-type lead telluride.<sup>10</sup>

Thermal conductivity data are shown in Figure 3.11. The lattice thermal conductivity (Figure 3.11b) is calculated from the thermal conductivity (Figure 3.11a) and the electrical conductivity (Figure 3.10b) according to the relationship  $\kappa_{\text{total}} - \kappa_{\text{carrier}} = \kappa_{\text{Lat}}$  and  $\kappa_{\text{carrier}} = L\sigma T$ , with  $L$  being the Lorenz number and  $T$  being the temperature.<sup>10</sup> The Lorenz number value of  $2.44 \times 10^{-8} \text{ W}\cdot\Omega\cdot\text{K}^{-2}$ , the value for degenerate semiconductors, is chosen as appropriate for this system in accordance with work by the Kanatzidis group.<sup>10</sup> In all cases, the lattice thermal conductivity represents the majority of the total thermal conductivity. This is not surprising given the low electrical conductivity observed for all samples. We find that the lattice thermal conductivities,  $\kappa_{\text{Lat}}$ , at room temperature are lower for all samples displayed in Figure 3.11b than the literature value for bulk lead telluride ( $2.0 \text{ W}\cdot\text{m}^{-1}\text{K}^{-1}$ ).<sup>10</sup> This is expected due to the nanocrystalline nature of the lead telluride comprising the samples.

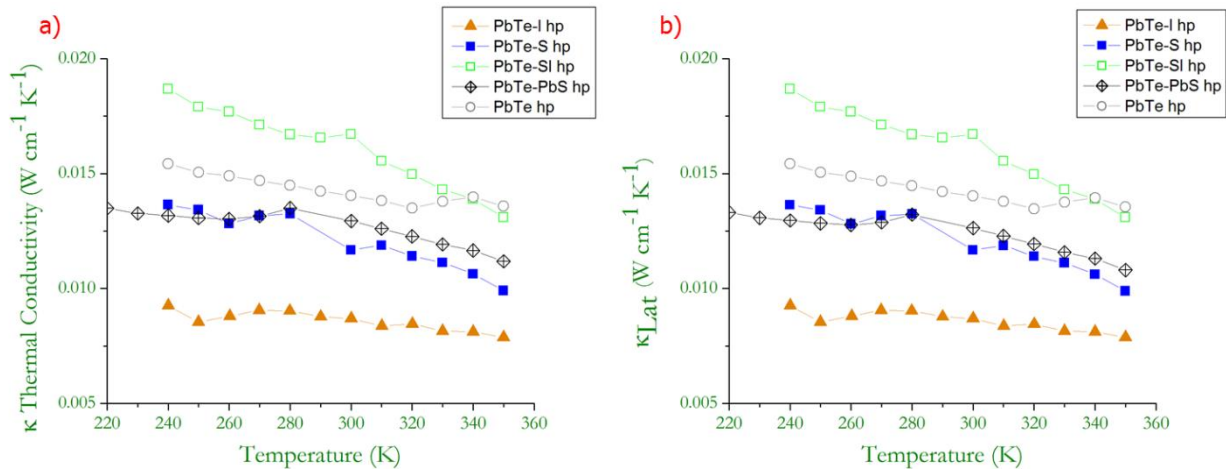


**Figure 3.11** Thermal conductivity (a) and lattice thermal conductivity (b) values near room temperature plotted as a function of temperature for the sulfide stripped sample (PbTe-S hp), the sulfide and iodide stripped sample (PbTe-SI hp), the control (PbTe hp), the iodide stripped sample (PbTe-I hp), and the composite of mixed lead sulfide and lead telluride nanoparticles (PbTe–PbS hp). The data point at 290 K for PbTe-S and PbTe–PbS is removed because of a common fluctuation that occurs from melting of small ice crystals in the cryostat.

For the sulfide stripped, iodide stripped, and PbS/PbTe composite samples, the lattice thermal conductivity is suppressed below that of the control, PbTe hp ( $1.4 \text{ W}\cdot\text{m}^{-1}\text{K}^{-1}$ ), which is actually rather high, nearly twice that of the  $0.75 \text{ W}\cdot\text{m}^{-1}\text{K}^{-1}$  reported by Cao, *et. al* for hot-pressed pellets of PbTe NCs (200 nm grain size).<sup>13</sup> In contrast, the sulfide and iodide stripped sample has the largest lattice thermal conductivity. This sample, PbTe-SI hp, also had the largest PbS crystallite size for inclusions after hot-pressing, which may be a contributing factor as matching phonon dispersion length scales with inclusion size is essential for lowering lattice thermal conductivity. Both the PbTe–PbS hp and PbTe-S hp samples had lower  $\kappa_{\text{Lat}}$  compared to the control. This is achieved with less lead sulfide mole percentage in the PbTe–PbS hp sample than in PbTe-S hp, in spite of the larger lead telluride crystallites, implying that the smaller lead sulfide nanocrystals are more effective at scattering phonons than the 60 nm lead sulfide in PbTe-S hp. However, the  $\kappa_{\text{Lat}}$  is still higher than that achieved in the previous work by the Kanatzidis group, in which 0.4 or 0.8  $\text{W}\cdot\text{m}^{-1}\text{K}^{-1}$  is achieved by precipitating 8 mol % or 4 mol % lead sulfide in lead telluride, yielding PbS crystallites of 3–10 nm in diameter).<sup>10</sup> These data suggest that, if the current methods are to demonstrate such low values, then the growth of lead sulfide nanocrystals must be limited. PbTe-I hp exhibits the lowest  $\kappa_{\text{Lat}}$  in the current work, which was unexpected. It appears that an amorphous iodide layer between lead telluride crystallites is moderating the propagation of phonons in the lattice.

The ZT values as a function of temperature are shown in Figure 3.12. In general, the relatively low electrical conductivities observed for the samples in the current work result in low ZT values (<0.05). PbTe–PbS hp has the largest ZT of all samples measured due to the large electrical conductivity, followed by PbTe-S hp due to the high Seebeck coefficient and a lattice

thermal conductivity similar to that of PbTe–PbS hp. Iodide stripped samples PbTe-I hp and PbTe-SI hp have the smallest ZT, lower than the PbTe control, dominated by the low electrical conductivity in these samples. These data underscore the importance of developing new methods for augmenting electrical conductivity if nanoparticle assemblies are to be practically employed in thermoelectrics.

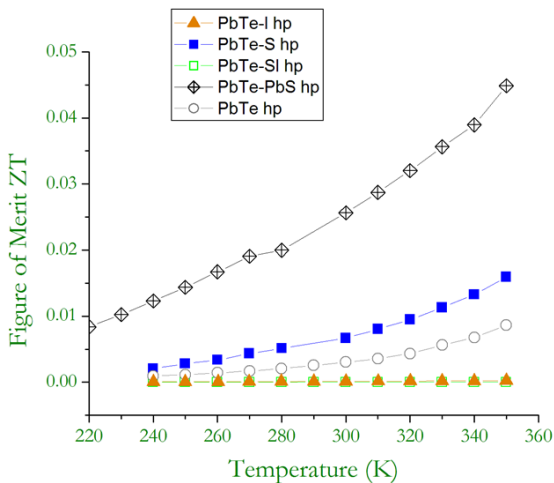


**Figure 3.12** Thermoelectric Figure of Merit, ZT, values as a function of temperature.

### 3.4. Conclusions

A multi-gram synthesis of lead telluride nanoparticles has been developed, producing quantities of crystalline material per synthesis suitable for thermoelectric testing. The resultant PbTe nanoparticles have been used to prepare nanocomposites with lead sulfide through physical mixing by incipient wetness as well as the surprising, in-situ growth of lead sulfide nanocrystals during ligand stripping by ammonium sulfide. Both methods of lead sulfide incorporation decrease the lattice thermal conductivity slightly versus the control. However, these values are still quite high compared to the  $0.4 \text{ W}\cdot\text{m}^{-1}\text{K}^{-1}$  achieved by precipitation from a melt in previous work by Androulakis et. al.<sup>10</sup> The higher values of lattice thermal conductivity observed in this study are thought to be due to failure of the lead sulfide nanocrystals to maintain their small size.

In comparison to bulk lead telluride, most of the decrease in lattice thermal conductivity observed in nanocomposites from this work results from nanostructuring of the lead telluride itself, as evidenced by the low lattice thermal conductivity of the control sample. All of the materials, however, exhibit low electrical conductivity. Ligand stripping of lead telluride nanoparticles with sources of sulfide and iodide was attempted to increase the electrical conductivity of the resulting nanostructures. However, the ligand stripping is found to dope the resulting nanostructures severely enough to not only determine whether they will be *n*-type or *p*-type, but also to greatly decrease the electrical conductivity. Much greater control over the degree of doping due to ligand stripping is needed in order to make this process viable. Since doping of nanoparticles is yet in its infancy, the simplest way to improve these nanostructures is to remain focused on the thermal conductivity, which is expected to be decreased beneficially by limiting the size of the nanoparticles.

## CHAPTER 4 : SOLVOTHERMAL SYNTHESIS OF TETRAHEDRITE: SPEEDING UP THE PROCESS OF THERMOELECTRIC MATERIAL GENERATION

### 4.1. INTRODUCTION

In the present work, we develop and optimize a ligand-less solvothermal route to synthetic tetrahedrite that can be done with one day of heating at moderate temperatures (ca 150 °C) and allows parallel processing due to the manageable temperature and pressure requirements. We begin by repeating a solvothermal synthesis of tetrahedrite from the literature. This is hot-pressed alone as well as after ball-milling with the natural mineral tennantite in a 1:1 mole ratio. The resulting tetrahedrite is characterized for thermoelectric properties around room temperature and found to have low performance. Due to the high chlorine content in these samples, we substituted nitrate and sulfate salts for the metal chloride precursors. The synthesis is repeated with the reducing solvent, ethylenediamine, in order to obtain the tetrahedrite crystal structure. The ratio of sulfur to copper precursor is modulated to determine the effect on the resulting crystal structure, composition, and crystalline impurities. Multiple syntheses are carried out in parallel and combined to form samples for hot-pressing. The hot-pressed pellets are characterized for thermoelectric properties for comparison. The solvothermal tetrahedrite is also ball-milled in a 1:1 mole to mole ratio with natural mineral (tennantite). We show that properties of the solvothermal tetrahedrite are comparable to those produced by solid state methods and that our product is amenable to doping by mixing with tennantite.<sup>99</sup> The work presented in this chapter has been published. (Reprinted (adapted) with permission from James, D. J.; Lu, X.; Morelli, D. T.; Brock, S. L., Solvothermal Synthesis of Tetrahedrite: Speeding Up the Process of Thermoelectric Material Generation. *ACS Appl. Mater. Interfaces* **2015**, DOI: 10.1021/acsami.5b07141. Copyright 2015 American Chemical Society.)

## 4.2. EXPERIMENTAL

**4.2.1. Synthesis and Characterization of Tetrahedrite: Literature Method.** There is one previous report of a solvothermal synthesis of tetrahedrite, and we used this as a basis of our initial exploration. The literature synthesis<sup>100</sup> is scaled down from the 50 mL vessel size to the 23 mL vessels that we had available. Briefly, 0.2944 g of copper(I) chloride, 0.2261 g of antimony(III) chloride, 0.2452 g of thiourea, and 18.4 mL of ethanol (200 proof) are added to a solvothermal vessel, which is then sealed in a stainless steel bomb and heated at 155 °C for 20 hours. After allowing the vessel to cool, the product is filtered and washed three times with deionized water followed by three ethanol washes. Subsequently the product is dried under vacuum at 50 °C.<sup>100</sup> This synthesis is repeated several times and the products combined to result in several grams of material for thermoelectric characterization.

**4.2.2. Synthesis of Tetrahedrite: Chloride Free with 100% Molar Excess Sulfur**

**Source.** Basic copper nitrate ( $\text{Cu}_2(\text{OH})_3\text{NO}_3$ , 0.3570g), antimony(III) sulfate (0.2503g), thiourea (0.4904g), and ethylenediamine (18.4mL) are combined in a 23 mL Teflon vessel. This is heated in a sealed stainless steel bomb in a furnace at 155 °C for 20–24 hours before the furnace is turned off and the pressurized vessel is allowed to cool on the benchtop. The product is then isolated by centrifugation and washed 1x with deionized water, followed by 5x with concentrated sulfuric acid, 2x with deionized water, and 1x with ethanol. The product is then dried under vacuum for at least four hours.

**4.2.3. Synthesis of Tetrahedrite: Chloride Free with 300% Molar Excess Sulfur**

**Source.** The synthesis is identical to that described above except that thiourea was increased to 0.9808 g and the isolation was performed by washing with deionized water (with agitation) followed by centrifugation, followed by washing with sulfuric acid (for one minute, again with

agitation) a total of 5x, followed by 2x with deionized water and 1x with ethanol. The yield is about 0.25 g per solvothermal vessel (64% of theoretical yield of 0.3922 g), and these were typically prepared in groups of four at a time.

**4.2.4. Synthesis of Tetrahedrite: Solid State Method.** For comparison to solvothermal materials, solid-state tetrahedrite was prepared as described in the literature.<sup>2</sup>

**4.2.5. Mixing of Tetrahedrite with NM.** Tetrahedrite (solvothermally or solid-state prepared) is ground together with the NM to target a 0.9 mol equivalent of Zn. These mixtures were then ball-milled at 1060 cycles per minute for 30 min using a stainless steel ball mill set in a SPEX 8000 Series Mixer.

### 4.3. RESULTS AND DISCUSSION

**4.3.1. Synthesis and Characterization of Tetrahedrite: Literature Method.** As a starting point to develop a facile and rapid synthesis of tetrahedrite, our initial studies focused on the one (to our knowledge) report of tetrahedrite formation by a solvothermal approach.<sup>100</sup> This method involves reaction of thiourea (as a sulfur source) with chloride salts of Cu<sup>+</sup> and Sb<sup>3+</sup> in ethanol in a stainless steel bomb under autogenous pressure at 155 °C for 20 hours.

Powder XRD data from the product obtained from the literature preparation reveals both famatinitite (Cu<sub>3</sub>SbS<sub>4</sub>) and tetrahedrite (Cu<sub>12</sub>Sb<sub>4</sub>S<sub>13</sub>) phases (Figure 4.1), as well as additional impurities that could not be identified relative to known phases in the ICDD-PDF database. The composition was determined to be Cu<sub>15.8</sub>Sb<sub>7.8</sub>S<sub>13</sub> by ICP-OES, which is metal-rich in both copper and antimony. Investigation by TEM and EDS revealed the product to be heterogeneous and to incorporate chlorine (Figure 4.2). The EDS of the region imaged in Figure 4.2a suggests a composition of Cu<sub>13.2</sub>Sb<sub>4.6</sub>S<sub>13</sub>Cl<sub>0.8</sub>, once scaled to a sulfur mole contribution of thirteen. This is less metal-rich than the bulk composition determined by ICP-OES, but there is still more metal

than called for by the tetrahedrite formula and the chlorine contributions cannot be neglected. The EDS of the region imaged in Figure 4.2b does not show any Sb or Cl, and suggests a composition of  $\text{Cu}_{2.0}\text{S}_{0.8}$ , similar to copper(I) sulfide, although this phase is not observed in the XRD pattern, suggesting it is present in small quantities and/or is amorphous.

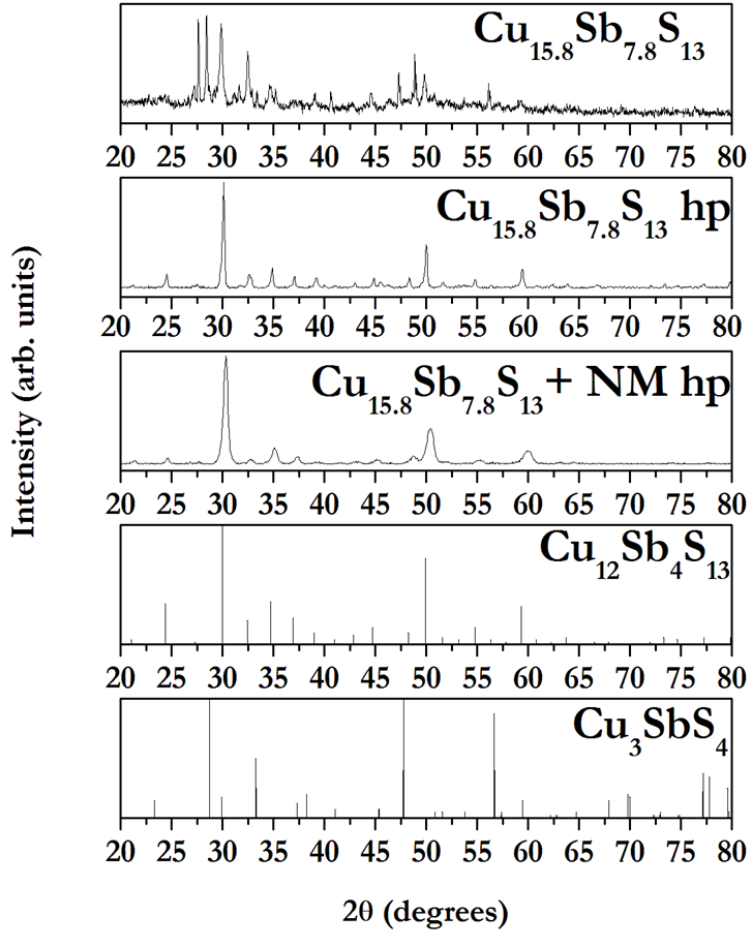


**Figure 4.1** XRD patterns of tetrahedrite synthesized by the reported literature method before ( $\text{Cu}_{15.8}\text{Sb}_{7.8}\text{S}_{13}$ ) and after hot-pressing ( $\text{Cu}_{15.8}\text{Sb}_{7.8}\text{S}_{13}$  hp). PDF patterns 42-0561 and 35-0581 are displayed for tetrahedrite ( $\text{Cu}_{12}\text{Sb}_4\text{S}_{13}$ ) and famatinite ( $\text{Cu}_3\text{SbS}_4$ ), respectively. The literature-prepared tetrahedrite is ball-milled in a 1:1 molar ratio with the natural mineral tennantite,  $\text{Cu}_{10}\text{Zn}_{1.8}\text{Fe}_{0.2}\text{As}_{2.7}\text{Sb}_{1.3}\text{S}_{13}$ , and hot pressed to produce  $\text{Cu}_{15.8}\text{Sb}_{7.8}\text{S}_{13} + \text{NM hp}$ .

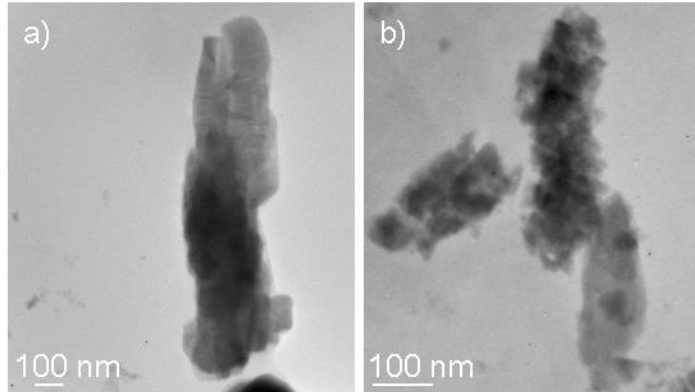


**Figure 4.2** TEM images of different regions of literature-prepared tetrahedrite revealing different compositions by EDS a)  $\text{Cu}_{13.2}\text{Sb}_{4.6}\text{S}_{13}\text{Cl}_{0.8}$  b)  $\text{Cu}_{2.0}\text{S}_{0.8}$ .

The literature-prepared tetrahedrite is hot-pressed alone and after mixing with the natural mineral (abbreviated as NM) tennantite ( $\text{Cu}_{10}\text{Zn}_{1.8}\text{Fe}_{0.2}\text{As}_{2.7}\text{Sb}_{1.3}\text{S}_{13}$ ) to achieve a 1:1 molar ratio. After hot-pressing at 430 °C the material ( $\text{Cu}_{15.8}\text{Sb}_{7.8}\text{S}_{13}$  hp) exhibits the XRD pattern of tetrahedrite (Figure 4.1) with few apparent crystalline impurities, suggesting the hot-pressing process was able to homogenize the mixture. Mixing the literature-prepared tetrahedrite with tennantite by ball-milling and then hot-pressing results in a shift in the tetrahedrite pattern towards higher  $2\theta$ , as expected, indicating that zinc is incorporated into the crystal structure as a solid solution (decrease in lattice parameters). Again, no crystalline impurities are revealed.

Relative to the solid-state tetrahedrite, the low-temperature thermoelectric properties of materials produced by the literature method reveal a ca 20% increased thermopower at room temperature,  $97 \mu\text{VK}^{-1}$ , as shown in Figure 4.3 a. This may be due to chloride acting as an electron dopant, filling the valence band holes and pushing the Fermi level towards the band gap. Mixing the natural mineral with the literature-prepared tetrahedrite sharply increases the thermopower at room temperature, to  $179 \mu\text{VK}^{-1}$ , as zinc is incorporated. These increased thermopower values come as a tradeoff for high resistivity as shown in Figure 4.3b. The resistivity of the literature-prepared tetrahedrite at room temperature is  $7.4 \text{ m}\Omega\cdot\text{cm}$ , or 230%

higher than that exhibited by solid state tetrahedrite ( $2.2 \text{ m}\Omega\cdot\text{cm}$ ). Upon mixing the literature recipe tetrahedrite in a 1:1 molar ratio with natural mineral, we predicted that some metallic behavior would be maintained with 0.9 mole equivalents of zinc because the resistivity of tetrahedrite is not reported to rise sharply until after the zinc doping level is increased above the optimum of 1 mole equivalent.<sup>2-3</sup> However, the high resistivity of the literature recipe tetrahedrite is further increased by mixing with the natural mineral, to  $69 \text{ m}\Omega\cdot\text{cm}$ . This indicates that the Fermi level is raised above the valence band and into the band gap, resulting in a semiconductor or insulator. Based on the significant quantities of chlorine detected in the EDS, we attribute this dramatic increase in resistivity to chloride doping in the literature-prepared sample.

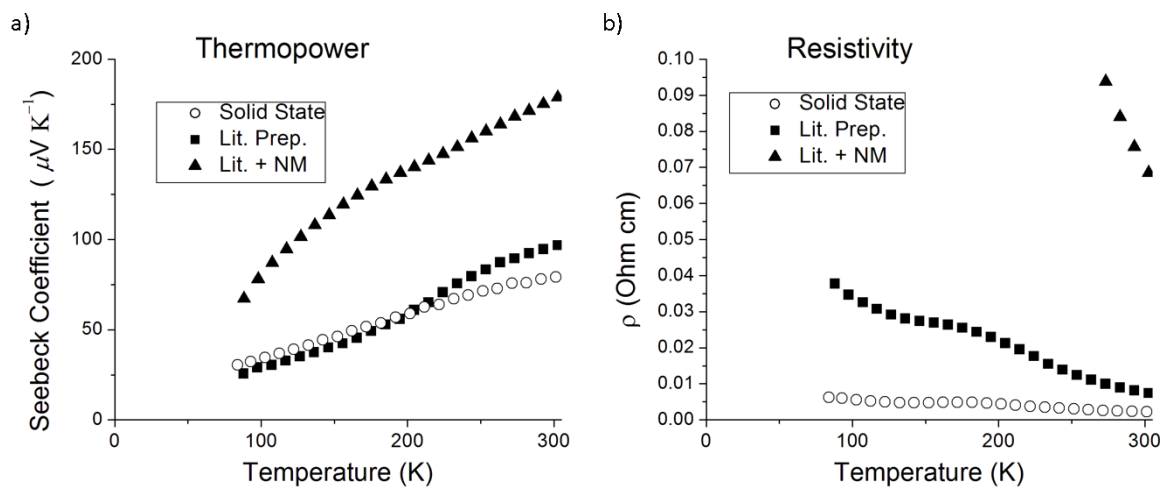


**Figure 4.3** The temperature-dependent Seebeck coefficient (a) and resistivity (b) values are displayed for the hot-pressed samples. These include the solvothermal tetrahedrite prepared by literature methods (Lit. Prep.), the solvothermal tetrahedrite mixed in a 1:1 molar ratio with the natural mineral tennantite,  $\text{Cu}_{10}\text{Zn}_{1.8}\text{Fe}_{0.2}\text{As}_{2.7}\text{Sb}_{1.3}\text{S}_{13}$  (Lit. + NM), and the solid state tetrahedrite (Solid State).

Thermal conductivity data for the solid state tetrahedrite, literature recipe tetrahedrite, and the 1:1 molar mixture of literature recipe tetrahedrite with natural mineral are displayed in Figure 4.4a. The thermal conductivity at room temperature of the literature recipe tetrahedrite is decreased some 20% from that of the solid state tetrahedrite ( $1.3 \text{ W m}^{-1} \text{ K}^{-1}$ ) to  $1.0 \text{ W m}^{-1} \text{ K}^{-1}$ .

The lower thermal conductivity tracks with higher resistivity, and is likely due to decreased electronic contribution to thermal conductivity ( $\kappa_C$ ). The thermal conductivity of the 1:1 mole to mole ratio mixture of literature recipe tetrahedrite and tennantite exhibits an even lower thermal conductivity at  $0.5 \text{ W m}^{-1} \text{ K}^{-1}$ , again correlating with increasing electronic resistivity.<sup>2-3</sup>

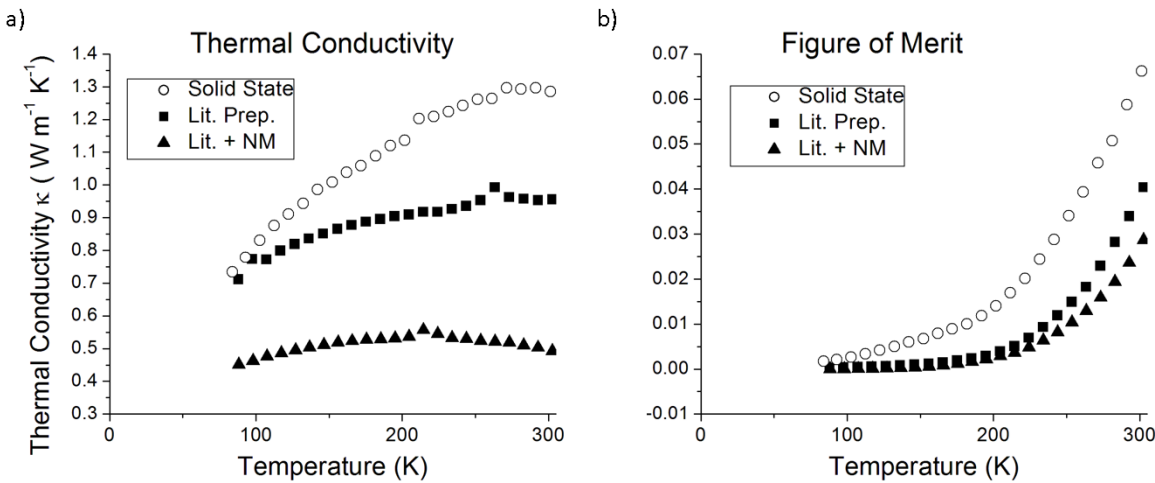


**Figure 4.4** Temperature-dependent thermal conductivity (a) and Figure of Merit, ZT (b) values of the hot-pressed samples. These include the solvothermal tetrahedrite prepared by literature methods (Lit. Prep.), the solvothermal tetrahedrite mixed in a 1:1 molar ratio with the natural mineral tennantite,  $\text{Cu}_{10}\text{Zn}_{1.8}\text{Fe}_{0.2}\text{As}_{2.7}\text{Sb}_{1.3}\text{S}_{13}$  (Lit. + NM), and the solid state tetrahedrite (Solid State).

The ZT values are calculated from the thermopower, resistivity, and thermal conductivity values and are displayed in Figure 4.4b for each of the hot-pressed samples. The literature recipe tetrahedrite exhibits a ZT value of 0.04 at room temperature, a ~45% decrease from the ZT value of 0.07 calculated for the solid state tetrahedrite. The sample of literature recipe tetrahedrite mixed in a 1:1 mole to mole ratio with tennantite exhibited an even lower ZT value of 0.03. In spite of higher Seebeck coefficients and lower thermal conductivity values, both samples containing literature tetrahedrite demonstrate lower ZT values than the solid state tetrahedrite. These decreases must be driven by the increased resistivity values. Compositional impurities, including the chloride doping, clearly increase the resistivity in the literature recipe tetrahedrite

disproportionately relative to the small increase achieved in thermopower. Therefore, we sought to avoid chloride precursors in optimizing the synthesis of tetrahedrite.

#### **4.3.2. Synthesis and Characterization of Tetrahedrite: Optimizing the Solvothermal**

**Synthesis of Tetrahedrite.** Since we viewed chloride as a counter ion that happens to dope the product, we sought to replace chloride with counter ions that would neither act as dopants nor precipitate an insoluble salt with any of the metals present. With this in mind, we decided to avoid not only halogens, but also good Lewis bases such as acetate, oleate, or oleylamine that might leave organic residues that might transform into amorphous carbon during hot-pressing. Nitrate and sulfate were selected as counter ions because they are resonance stabilized conjugate bases of strong acids that are carbon and halogen free, and they do not form insoluble salts with Cu<sup>+</sup>, Cu<sup>2+</sup>, or Sb<sup>3+</sup>. Accordingly, the basic copper nitrate (Cu<sub>2</sub>(OH)<sub>3</sub>NO<sub>3</sub>) was chosen as the new source of copper. Antimony nitrate is not commercially available; so, antimony(III) sulfate is used instead.

The reducing solvent ethylenediamine is employed to favor reduction of the Cu<sup>2+</sup> in the copper source (Cu<sub>2</sub>(OH)<sub>3</sub>NO<sub>3</sub>) to Cu<sup>+</sup>, because 10/12 copper cations present in tetrahedrite are monovalent. To produce a reducing environment, ethylenediamine (en) is reported to complex with the cation Cu<sup>2+</sup> as [Cu(en)<sub>3</sub>]<sup>2+</sup>.<sup>101</sup> Although the copper cation is chelated in this complex, the ligands are constantly exchanging with fresh ethylenediamine from the solvent ( $k_{\text{ex}} = 1.4 \times 10^7 \text{ s}^{-1}$  at 25 °C) by a dissociative-interchange mechanism, leaving Cu<sup>2+</sup> accessible to nucleophilic attack by the active sulfur source, hydrogen sulfide. The thiourea serves as the source of sulfur by decomposing to form hydrogen sulfide and a water soluble side product, cyanamide (HNCNH).<sup>102</sup>

To synthesize tetrahedrite, basic copper nitrate ( $\text{Cu}_2(\text{OH})_3\text{NO}_3$ ) is combined stoichiometrically with antimony(III) sulfate and thiourea in ethylenediamine and heated in a teflon-lined stainless steel bomb in a furnace at 155 °C for 20–24 hour. The product comprises tetrahedrite, chalcostibite ( $\text{CuSbS}_2$ ), and antimony(III) oxide ( $\text{Sb}_2\text{O}_3$ ) by XRD (Figure 4.5). Early studies indicated that use of excess thiourea could reduce the formation of chalcostibite and  $\text{Sb}_2\text{O}_3$  (Figure 4.6), and that crystalline  $\text{Sb}_2\text{O}_3$  can be removed by sulfuric acid washes in the isolation (expanded view Figure 4.7). The final product (100% excess thiourea and sulfuric acid washes) exhibits the tetrahedrite XRD pattern as the major crystalline product, although chalcostibite remains as a significant impurity (Figure 4.9). Expanded views of XRD patterns and corresponding metal compositions (determined by ICP-OES) for several repetitions of this synthesis are available in supporting information (Figure 4.8). The samples are combined in appropriate amounts to obtain a ratio of Sb : Cu of 3.98 : 12 (scaled to 12 copper) for a formula of  $\text{Cu}_{12}\text{Sb}_{3.98}\text{S}_{13}$  (assuming Cu:S is 12:13).

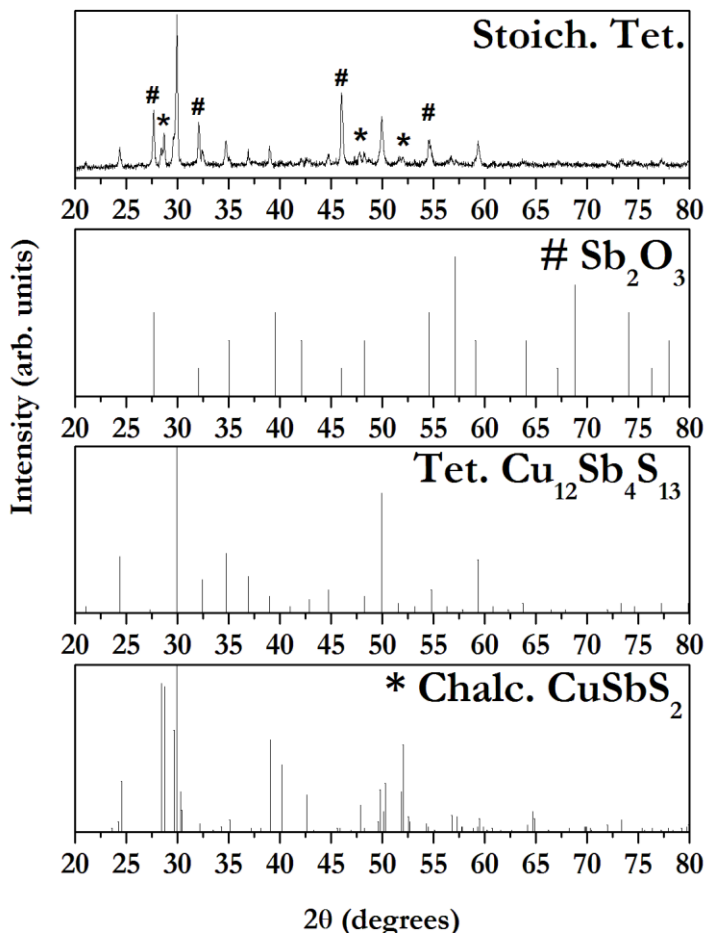


**Figure 4.5** XRD pattern of the solvothermal tetrahedrite product synthesized with a stoichiometric ratio of reagents is displayed. The reference patterns, PDF 05-0534, PDF 42-0561, and PDF 44-1417 are displayed for antimony(III) oxide ( $\text{Sb}_2\text{O}_3$ ), tetrahedrite ( $\text{Cu}_{12}\text{Sb}_4\text{S}_{13}$ ), and chalcostibite ( $\text{CuSbS}_2$ ), respectively. The \* marks the locations of prominent chalcostibite peaks, and the # marks locations of prominent  $\text{Sb}_2\text{O}_3$  peaks that do not overlap with peaks from tetrahedrite.

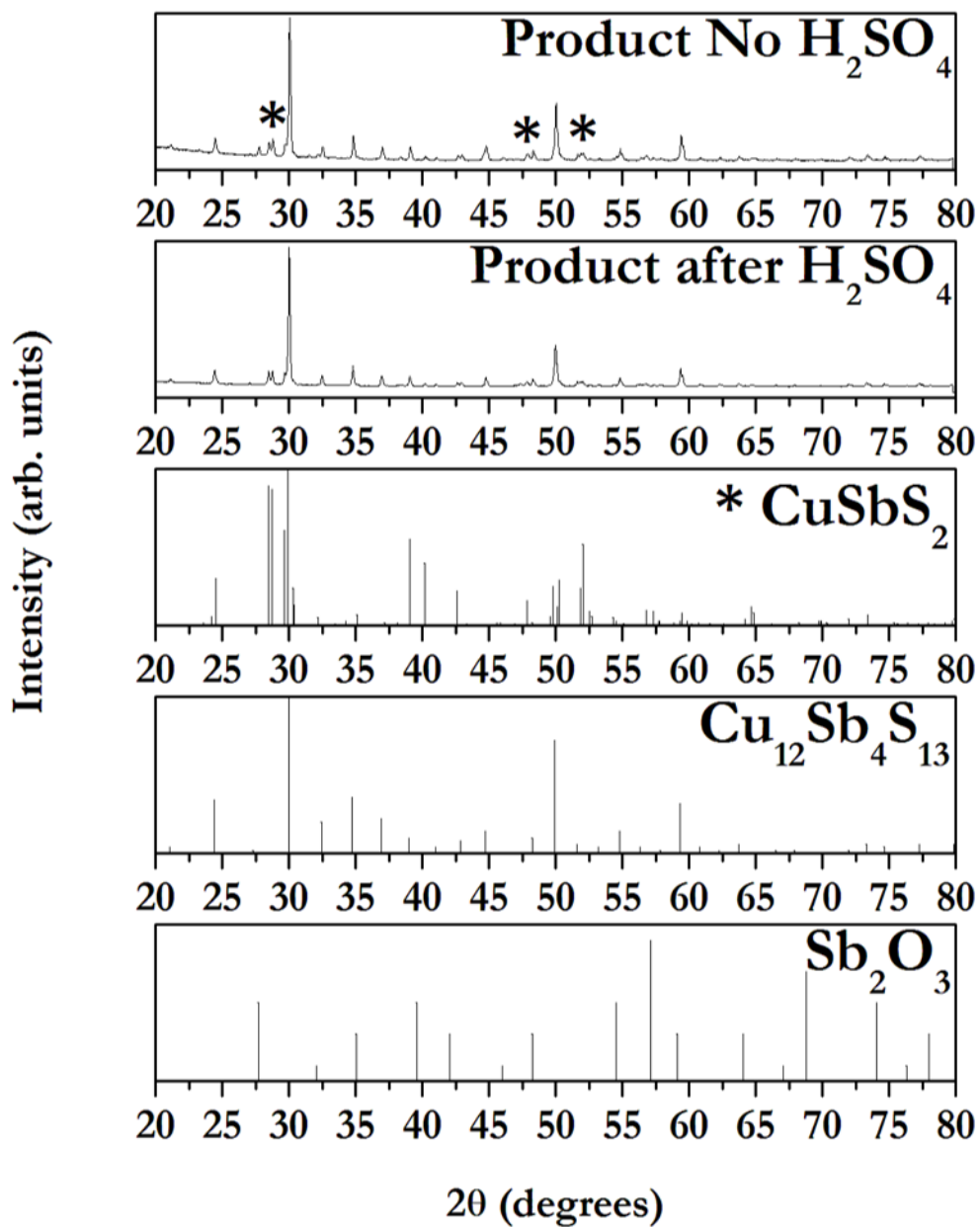


**Figure 4.6** XRD patterns of the solvothermal tetrahedrite product synthesized with 100% molar excess of thiourea before and after treatment with sulfuric acid. The reference patterns, PDF 05-0534, PDF 42-0561, and PDF 44-1417 are displayed for antimony(III) oxide ( $\text{Sb}_2\text{O}_3$ ), tetrahedrite ( $\text{Cu}_{12}\text{Sb}_4\text{S}_{13}$ ), and chalcostibite ( $\text{CuSbS}_2$ ). The \* marks locations of prominent  $\text{CuSbS}_2$  peaks that do not overlap with peaks from tetrahedrite.

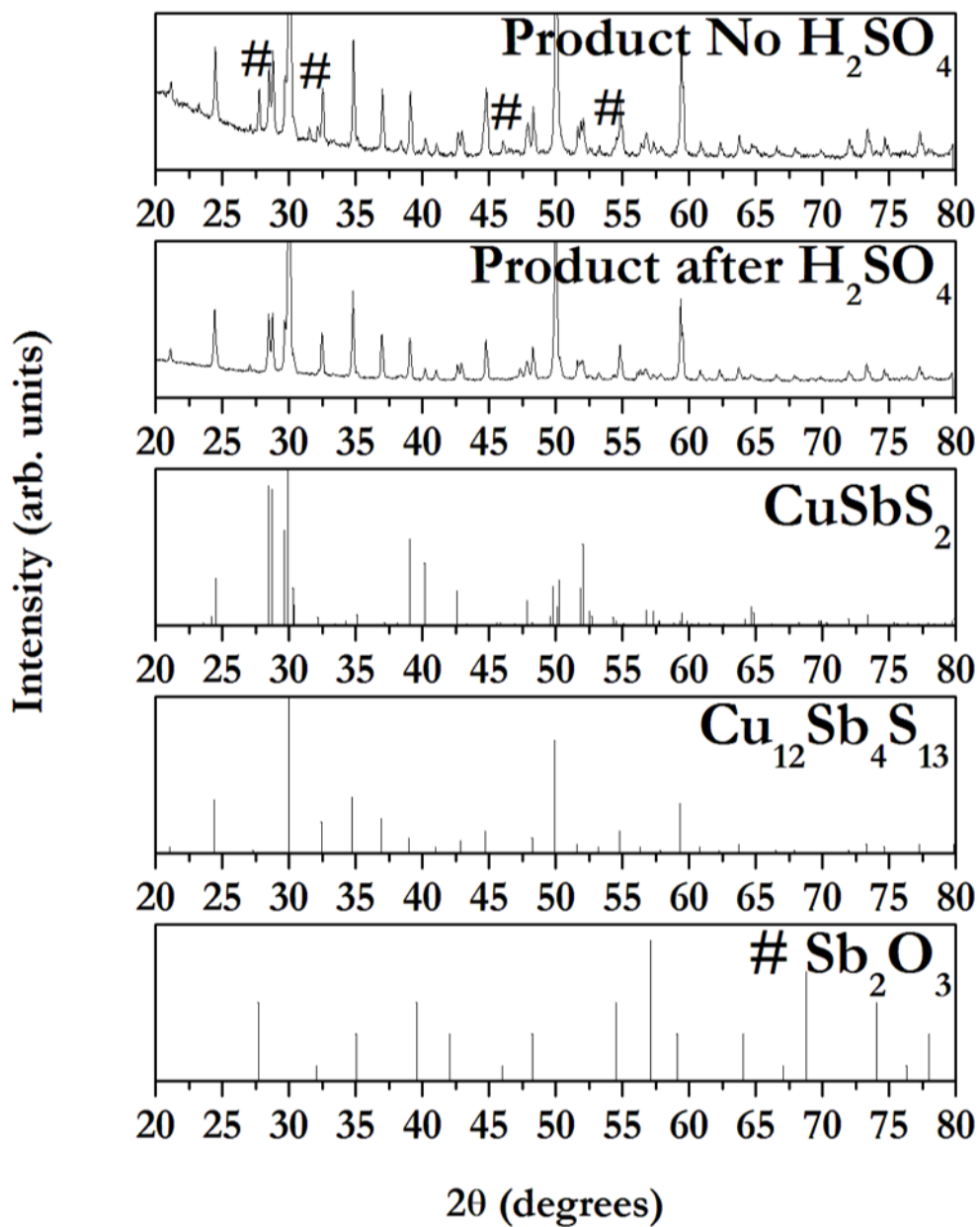


**Figure 4.7** XRD patterns of the solvothermal tetrahedrite product synthesized with 100% molar excess of thiourea before and after treatment with sulfuric acid. The reference patterns, PDF 05-0534, PDF 42-0561, and PDF 44-1417 are displayed for antimony(III) oxide ( $\text{Sb}_2\text{O}_3$ ), tetrahedrite ( $\text{Cu}_{12}\text{Sb}_4\text{S}_{13}$ ), and chalcostibite ( $\text{CuSbS}_2$ ). The # marks locations of prominent  $\text{Sb}_2\text{O}_3$  peaks that do not overlap with peaks from tetrahedrite.

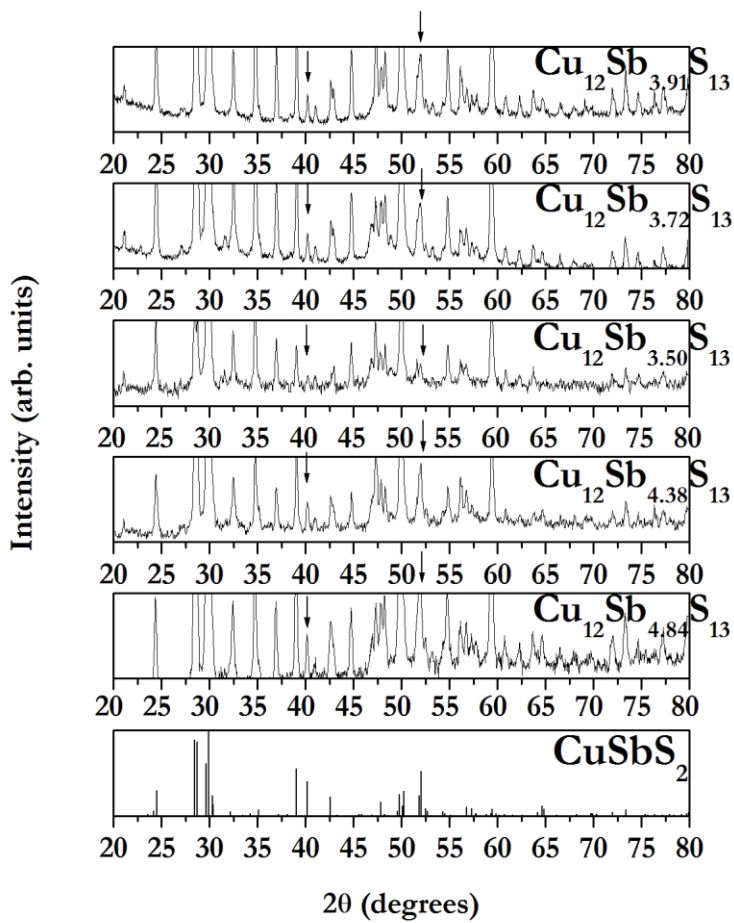


**Figure 4.8** XRD spectra of several solvothermal tetrahedrite products synthesized with 100% molar excess thiourea. The pattern PDF 44-1417 for chalcostibite ( $\text{CuSbS}_2$ ) is shown for reference. The arrows mark locations of prominent  $\text{CuSbS}_2$  peaks that do not overlap with peaks from tetrahedrite or famatinite.

The tetrahedrite peaks as well as the chalcostibite peaks are exhibited before and after hot-pressing the material alone as shown in Figure 4.9. However, the prevalence of the chalcostibite peaks is greatly decreased by ball-milling the material with the natural mineral before hot-pressing to form a solid solution, due to dilution.

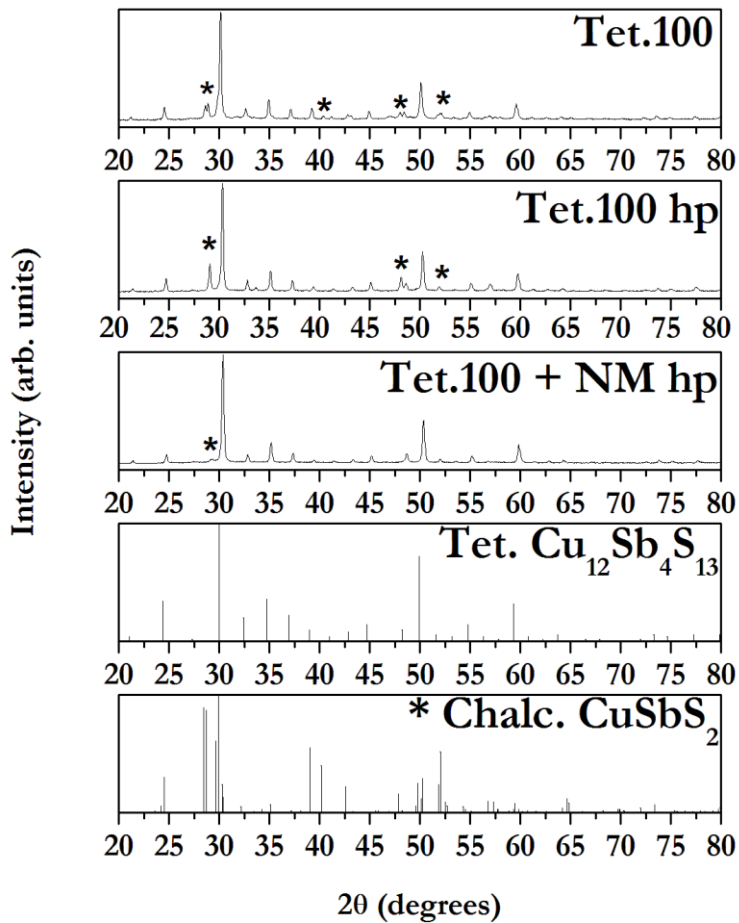


**Figure 4.9** XRD patterns from solvothermal tetrahedrite synthesized with 100% molar excess thiourea (Tet.100) before and after hot-pressing as well as after ball-milling with NM and hot-pressing. Reference patterns for tetrahedrite ( $\text{Cu}_{12}\text{Sb}_4\text{S}_{13}$ ), PDF 42–0561, and chalcostibite ( $\text{CuSbS}_2$ ), PDF 44-1417, are displayed below the data plots and \* marks observed peaks due to chalcostibite.

Low-temperature measurements of thermoelectric properties for the chalcostibite-containing samples (Tet.100 hp and Tet.100+NM hp) are displayed (Figure 4.10) and room temperature data comparing materials produced from hot-pressing (with and without NM) solid state, literature-prepared, and tetrahedrite synthesized with 100% molar excess thiourea are tabulated in Supporting Information (Table 4.1). Relative to the literature-prepared material, the resistivity of the Tet.100 hp sample is decreased by over 50%, but that is offset by a decrease in thermopower (20%) and increase in thermal conductivity (20%) resulting in no change in ZT

(~45% decreased from the solid state value). However, in contrast to the literature prepared material, combining Tet.100 with the NM and hot-pressing increases the ZT. The final value is twice that of the similarly processed literature prepared sample, but still only 30% of what is achieved when the solid state material is combined with tennantite.

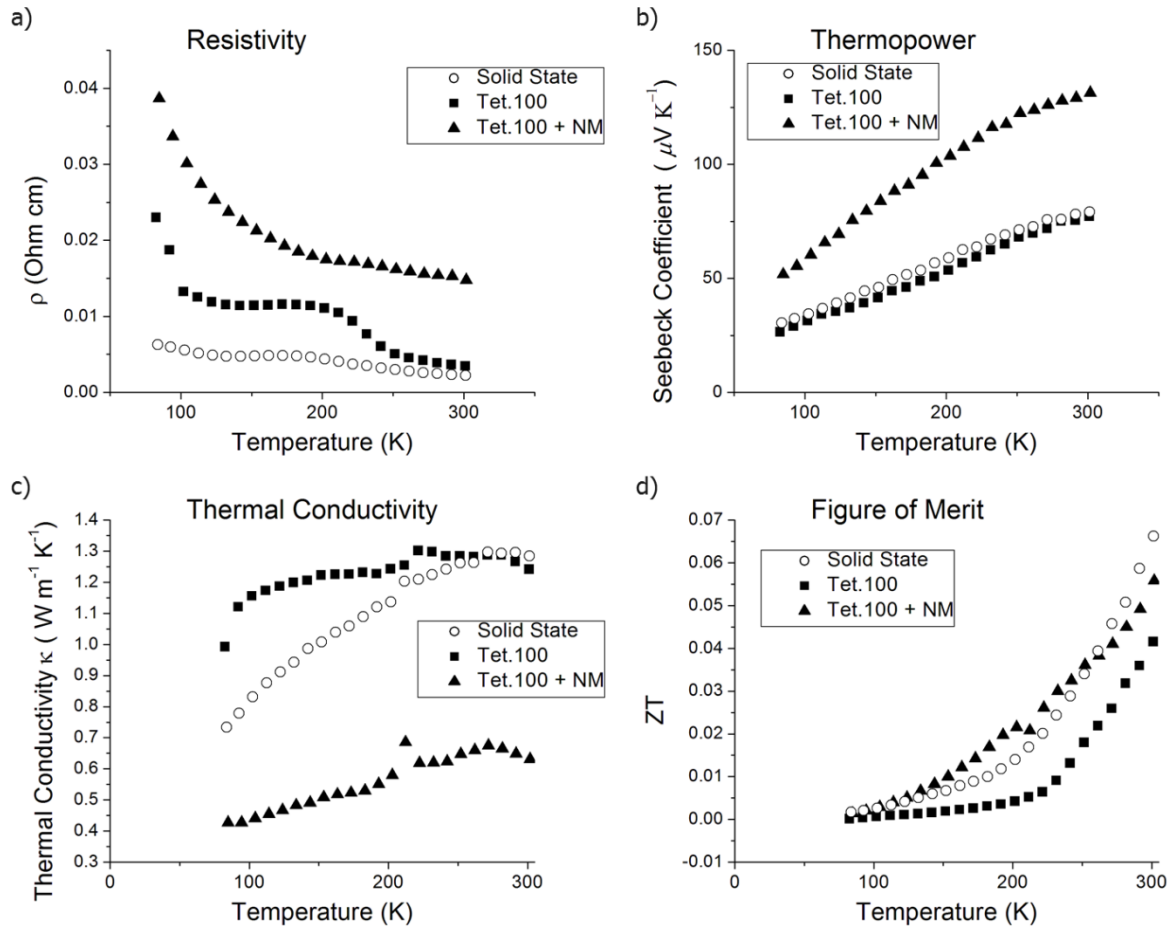


**Figure 4.10** Thermoelectric properties determined from 80 K to 300 K are displayed for solid state tetrahedrite (Solid State), solvothermal tetrahedrite synthesized with 100% molar excess thiourea (Tet.100), and the solvothermal tetrahedrite synthesized with 100% molar excess thiourea and mixed with NM (Tet.100 + NM). Properties displayed include a) Resistivity, b) Thermopower, c) Thermal Conductivity, and d) Figure of Merit.

**Table 4.1** Room temperature thermoelectric properties determined for solid state tetrahedrite (Solid State), the solid state tetrahedrite mixed with NM (Solid State + NM), the solvothermal tetrahedrite synthesized with 100% molar excess thiourea (Tet.100), the solvothermal tetrahedrite synthesized with 100% molar excess thiourea and mixed with NM (Tet.100 + NM), and the solvothermal tetrahedrite prepared by literature methods alone (Lit. Prep.) and mixed in a 1:1 molar ratio with NM (Lit. + NM) are displayed for comparison.

Sample (Room Temp)	$\rho$ (mohm•cm)	S ( $\mu\text{V K}^{-1}$ )	$\kappa$ ( $\text{W m}^{-1} \text{K}^{-1}$ )	ZT
Solid State (301 K)	2.2	79	1.3	0.07
Solid State +NM (300 K)	6.8	144	0.4	0.2
Lit. Prep. (303 K)	7.4	97	1.0	0.04
Lit. Prep. + NM (303 K)	69	179	0.5	0.03
Tet.100 (301 K)	3.5	77	1.2	0.04
Tet .100+ NM (302 K)	14.8	131	0.6	0.06

Since the chalcostibite containing tetrahedrite from the solvothermal synthesis performed more poorly than solid state tetrahedrite, we endeavored to prevent the formation of the  $\text{CuSbS}_2$  impurity by further increasing the ratio of sulfur to metal in the reagent mixture. Utilizing a 300% excess of thiourea relative to copper results in a fluctuating composition from batch to batch, as well as a famatinite ( $\text{Cu}_3\text{SbS}_4$ ) phase impurity, but suppresses the formation of chalcostibite,  $\text{CuSbS}_2$  (Figure 4.11). The compositions and XRD patterns from several repetitions of this synthesis are displayed in Figure 4.12. More example compositions of products obtained via this synthesis are displayed in (Table 4.2).

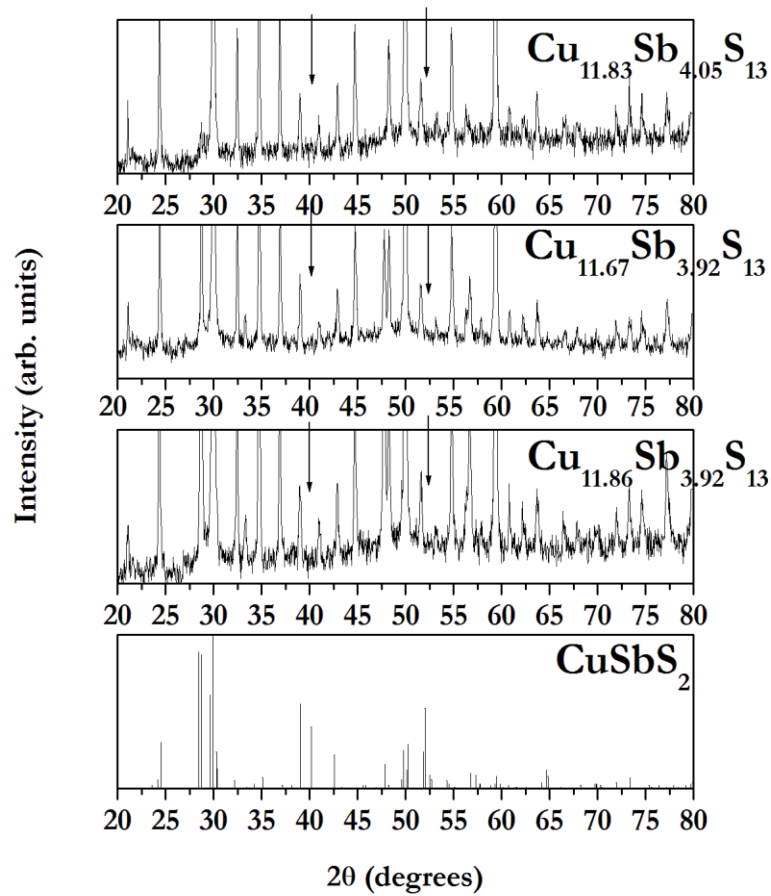


**Figure 4.11** Expanded views of the XRD patterns from several runs of the solvothermal synthesis with 300% molar excess sulfur source are displayed along with their compositions as determined by ICP-OES. The pattern for chalcostibite ( $\text{CuSbS}_2$ ) is shown for reference. The arrows mark locations of where the prominent  $\text{CuSbS}_2$  peaks that do not overlap with peaks from tetrahedrite or famatinite would be expected to be.

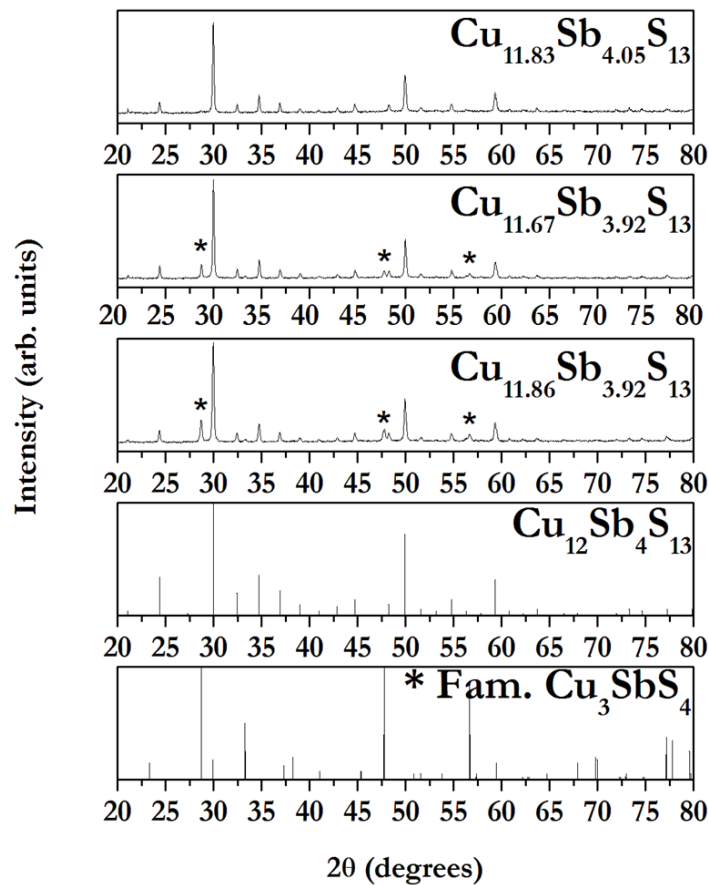


**Figure 4.12** XRD patterns for the tetrahedrite product from several runs of the solvothermal synthesis using 300% molar excess of sulfur precursor. Reference PDF patterns 42–0561 and 35–0581 are displayed for tetrahedrite ( $\text{Cu}_{12}\text{Sb}_4\text{S}_{13}$ ) and famatinite ( $\text{Cu}_3\text{SbS}_4$ ), respectively. The ICP-OES determined composition, normalized to S = 13, is displayed for each product. The \* marks observed peaks for famatinite.

**Table 4.2** Compositions of many tetrahedrite products from the solvothermal synthesis with 300% molar excess thiourea as determined by ICP-OES. Mole equivalents of Sb and Cu are scaled to 13 mole equivalents of sulfur. The tetrahedrite products are combined and the weighted average of Sb moles and Cu moles are listed below, along with the mass of the combined samples.

Sample	Sb	Cu	Sample	Sb	Cu
7-14-14 3	4.420	12.91	8-4-14 1	4.080	11.36
7-26-14 2	3.440	11.49	8-4-14 2	4.319	11.58
7-26-14 3	3.426	12.13	8-4-14 3	3.921	11.86
7-28-14 2	4.111	11.21	8-4-14 4	4.199	11.083
7-28-14 4	3.891	11.55	8-6-14 1	3.925	11.67
8-2-14 1	3.864	10.70	8-6-14 2	3.890	11.68
8-2-14 2	4.133	11.76	8-6-14 3	3.739	10.98
8-2-14 3	4.000	10.32	8-6-14 4	3.987	11.89
8-2-14 4	4.054	11.83			
Weighted Avg.	3.960	11.54			
Total grams	4.232				

The crystalline famatinite is the likely cause of the fluctuation in composition noticed in this work. To address this fluctuation, the solvothermal products are mixed in appropriate amounts before hot-pressing to achieve an Sb:S atomic ratio of about 4:13. These solvothermal products tend to be copper poor due to the lower Cu:S ratio in the famatinite impurity. The famatinite crystalline impurity remains after hot-pressing, but the peaks are far less prevalent if the tetrahedrite is mixed with the NM and hot-pressed, again due to dilution (Figure 4.13).

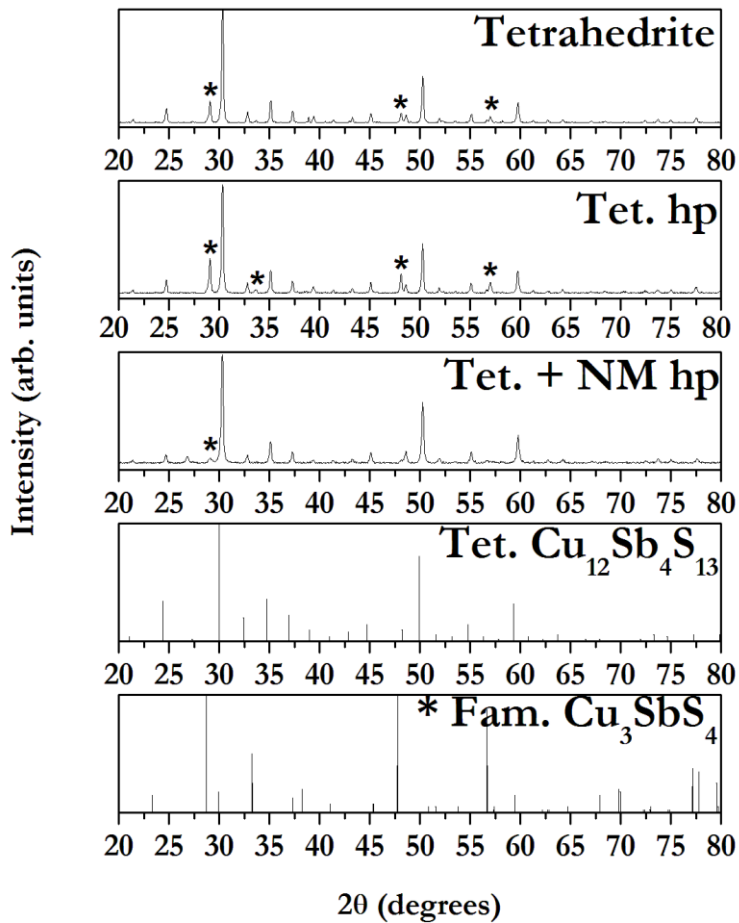


**Figure 4.13** XRD patterns from the solvothermal tetrahedrite synthesized with 300% molar excess thiourea before (Tetrahedrite) and after (Tet. hp) hot-pressing as well as the tetrahedrite ball-milled with NM and hot-pressed (Tet. + NM hp). Reference PDF patterns 42–0561 and 35–0581 are displayed for tetrahedrite ( $\text{Cu}_{12}\text{Sb}_4\text{S}_{13}$ ) and famatinitite ( $\text{Cu}_3\text{SbS}_4$ ), respectively. The \* marks observed peaks for famatinitite.

#### 4.3.3. Thermoelectric Characterization of Tetrahedrite Prepared with 300% Molar

**Excess Sulfur.** Based on previous data from Tet.100 and Tet.100 + NM, and the fact that ZT is maximized for tetrahedrite at high temperature, high temperature (310–730 K) thermoelectric properties were determined for hot-pressed solvothermal tetrahedrite from the 300% molar excess sulfur synthesis with and without mixing of NM. Thermopower values are displayed Figure 4.14 a. The thermopower curve for the solvothermal tetrahedrite largely overlaps that of the solid state tetrahedrite. They exhibit similar values at ~720 K of 130 and 140  $\mu\text{VK}^{-1}$ ,

respectively. Mixing either the solid state or solvothermal tetrahedrite with natural mineral tennantite to achieve 0.9 mol equivalents of Zn results in a large increase in thermopower across the temperature range. Mixing the solid state tetrahedrite with NM increases thermopower by ~40% to  $198 \mu\text{VK}^{-1}$  at ~720 K. Upon combination with NM, the solvothermal tetrahedrite behaves similarly, increasing thermopower by ~45% to  $202 \mu\text{VK}^{-1}$ .

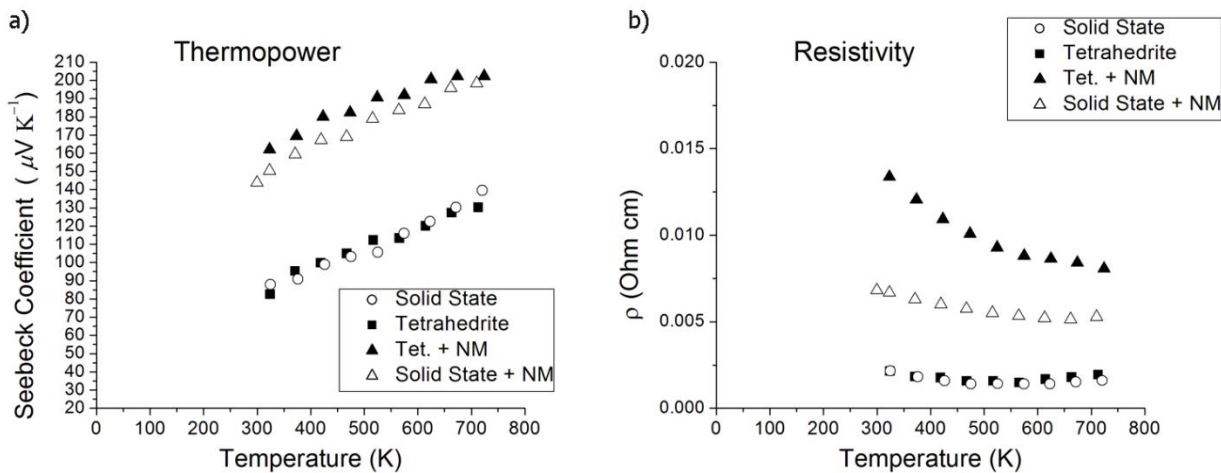


**Figure 4.14** Temperature-dependent Seebeck coefficient (a) and resistivity (b) values from room temperature to 720 K plotted as a function of temperature for the solid state tetrahedrite (Solid State), the solvothermal tetrahedrite synthesized with 300% molar excess thiourea (Tetrahedrite), the solvothermal tetrahedrite mixed with natural mineral (Tet. + NM), and the solid state tetrahedrite mixed with NM (Solid State + NM). All samples were hot-pressed

Resistivity data are displayed in Figure 4.14 b. The solvothermal tetrahedrite exhibits a similar resistivity curve to that recorded for the solid state tetrahedrite with a similar value near room temperature and a ca 20% higher value at ~720 K (1.9 vs. 1.6  $\text{m}\Omega\cdot\text{cm}$ ). Mixing NM with the solvothermal tetrahedrite results in a large (~540%) increase in resistivity at high temperature, over double that observed for the solid state material. The rise in resistivity is upon combining with NM is attributed to doping by Zn raising the Fermi Level towards the top of the valence band, and thus giving a more semiconductor flavor to the metal.<sup>2-3</sup> Thus, the excessive increase in resistivity in the solvothermal materials may be due to less than optimal Zn doping

quantities, as we have not compensated for the material's 4% copper deficiency (Table 4.2). Alternatively (or additionally), the famatinite impurities may be playing a role.

The thermal conductivity,  $\kappa_{\text{tot}}$ , data for the samples are displayed in Figure 4.15 a. The pure, solid state tetrahedrite exhibits the highest  $\kappa_{\text{tot}}$  across the temperature range. Thermal conductivity for the solvothermal tetrahedrite at the low end (324 K) is  $1.2 \text{ W m}^{-1} \text{ K}^{-1}$ , which is close to that of solid state tetrahedrite, whereas at the high end of the range ( $\sim 720 \text{ K}$ ), there is a ca 30% decrease in thermal conductivity to  $1.0 \text{ W m}^{-1} \text{ K}^{-1}$  from that observed for the solid state tetrahedrite ( $1.4 \text{ W m}^{-1} \text{ K}^{-1}$ ). Mixing the NM with the solid state or solvothermal tetrahedrite decreases the thermal conductivity significantly ( $\sim 70\%$ ) in both samples at the low temperature end (323 K), with a slight positive slope with increasing temperature.

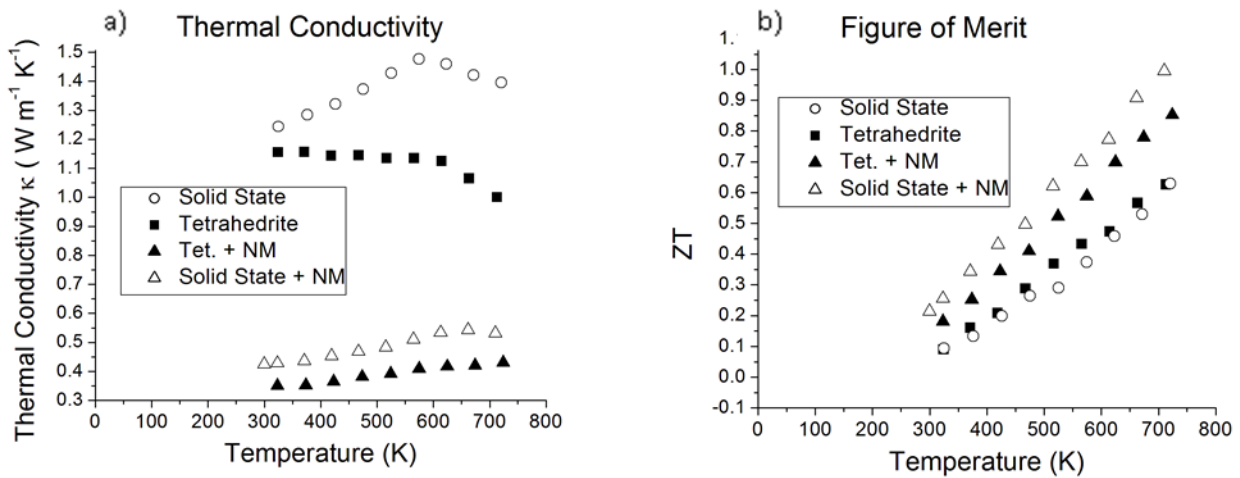


**Figure 4.15** Thermal conductivity (a) and ZT (b) values from room temperature to 720 K plotted as a function of temperature for the solid state tetrahedrite (Solid State), the solvothermal tetrahedrite synthesized with 300% molar excess thiourea (Tetrahedrite), the solvothermal tetrahedrite mixed with natural mineral (Tet. + NM), and the solid state tetrahedrite mixed with NM (Solid State + NM).

The ZT values as a function of temperature are displayed for each sample in Figure 4.15 b. The solvothermal tetrahedrite performs similarly to the solid state tetrahedrite over the temperature range studied. This is a large improvement compared to the literature prepared sample or the Tet.100 sample ( $ZT = 0.04$ ). Clearly, the higher resistivity and slightly lower

thermopower of the solvothermal tetrahedrite compared to solid state tetrahedrite is effectively compensated for by the decreased thermal conductivity, yielding similar ZT values in the two. Mixing either solvothermal or solid state tetrahedrite with NM increased ZT values across the temperature range. Near 720 K, the solid state tetrahedrite and NM mixture reaches unity, a 60% increase over the ZT for the solid state tetrahedrite alone, whereas the solvothermal tetrahedrite and NM mixture achieves ZT = 0.85 at ~720 K. We expect that the ZT of solvothermal tetrahedrite can be optimized by changing the proportion of NM to optimize the doping and neutralizing the effect of famatinite impurities and/or eliminating them entirely.

#### 4.4. CONCLUSIONS

A chloride-free, solvothermal synthesis of tetrahedrite is developed as a means of quickly and simultaneously producing multiple samples of tetrahedrite at relatively low temperatures (150 °C). The new solvothermal synthesis provides about 0.25 g of tetrahedrite per vessel in a single day and can easily be run in parallel with multiple vessels in an oven, in contrast to solid-state synthetic routes that require higher temperatures and processing that takes three days in a furnace, multiple re-grindings, and at least two weeks of annealing. The use of 100% excess sulfur in the solvothermal synthesis leads to chalcostibite impurities and an unacceptably high resistivity, whereas 300% excess sulfur leads to famatinite impurities that also increase resistivity relative to solid-state materials, but more modestly. Upon mixing the latter with the zinc-rich natural mineral, tennantite, ZT values of 0.85 can be achieved at 720 K, within reach of values obtained with the similarly doped solid-state material.

Current investigations are focused on optimizing the synthesis to further reduce contributions from minor impurity phases and developing in-situ doping strategies for inclusion of  $Zn^{2+}$  and  $Mn^{2+}$  in a single-pot strategy that obviates the need to mix with tennantite. We view

the rapid production of “tunable” tetrahedrite as a milestone towards commercialization of thermoelectric devices for widespread application.

## CHAPTER 5 : TUNING THE THERMOELECTRIC PROPERTIES OF SOLVOTHERMAL TETRAHEDRITE BY DOPING IN-SITU WITH ZINC

### 5.1. INTRODUCTION

In the present work, we modify our solvothermal synthesis of tetrahedrite to dope with zinc in-situ. As described in Chapter 4, pure tetrahedrite ( $\text{Cu}_{12}\text{Sb}_4\text{S}_{13}$ ) has low a ZT because of low thermopower and a moderate total thermal conductivity ( $\kappa_{\text{tot}} \sim 1.3 \text{ W m}^{-1}\text{K}^{-1}$ ).<sup>2-3, 77, 81-82, 84-85,</sup><sup>99</sup> However, the lattice thermal conductivity ( $\kappa_L = 0.4 \text{ W m}^{-1}\text{K}^{-1}$  at 700 K)<sup>2-3</sup> is low, and the substantial remaining thermal conductivity is due to carrier contribution ( $\kappa_C$ ). The ZT can be improved by doping with zinc to increase the thermopower and lower the thermal conductivity by increasing the resistivity (decreasing the  $\kappa_C$ ).<sup>2-3</sup> The  $\text{Zn}^{2+}$  substitutes for  $\text{Cu}^{2+}$  in  $\text{Cu}_{12-x}\text{Zn}_x\text{Sb}_4\text{S}_{13}$  to contribute one extra electron per ion, and raises the Fermi Level in the valence band towards the top. This adjusts the electronic properties from metallic to semiconducting as the mole contribution of zinc is increased from  $x = 0$  to 2.<sup>77, 81</sup> Zinc-rich tennantite ( $\text{Cu}_{10.0}\text{Zn}_{1.8}\text{Fe}_{0.2}\text{As}_{2.7}\text{Sb}_{1.3}\text{S}_{13}$ ) is available as a natural mineral and served as a source of zinc for doping solid state tetrahedrite by ball-milling in previous work.<sup>3</sup> This method achieves a ZT value of one with an optimal zinc mole contribution of  $x = 0.9$ . We exploited this approach to dope our solvothermal tetrahedrite with zinc by ball-milling it with the natural mineral, as described in Chapter 4, to achieve a ZT of 0.85 at  $x = 0.9$ .<sup>99</sup> In addition to zinc doping with tennantite, the solid state tetrahedrite can be doped with zinc in-situ, and ZT values of 1.0 and 0.8 have been reported for  $x = 0.5$  and 1.0, respectively.<sup>2</sup> We attempted to dope our solvothermal synthesis in-situ with zinc, with a target zinc mole contribution ( $x \sim 1$ ) near the optimal doping of the ball-milled samples for comparison with our previous work.

In order to study the properties of solvothermally-prepared  $\text{Cu}_{12-x}\text{Zn}_x\text{Sb}_4\text{S}_{13}$ , we prepared a range of compositions ( $x = 0.79, 1.15$ , and  $1.40$ ). The optimal zinc doping reported for solid state material is  $x = 0.9$  when the natural mineral is used as the zinc source and  $0.5$  when elemental zinc is used.<sup>2-3</sup> The difference in optimum doping level stems from the addition of available energy states (minority spin) near the top of the valence band from the magnetic moment of  $\text{Fe}^{3+}$  impurities in tennantite.<sup>77</sup> However, we wanted to compare our in-situ doped solvothermal tetrahedrite with our mix of tennantite with solvothermal tetrahedrite.<sup>99</sup> For the maximum amount of zinc, it has been reported that the tetrahedrite becomes insulating at  $x = 2$ ; therefore, we would like to explore how much zinc can be incorporated to improve the ZT before the material becomes insulating by testing tetrahedrite with close to one mole equivalent of zinc.<sup>81</sup>

Samples are prepared with a target zinc composition by modification of the solvothermal method discussed in Chapter 4. These are characterized for crystallinity and composition. The composition fluctuates; therefore, we found it necessary to combine multiple samples to achieve the desired composition as an average. Then, the product is hot-pressed to form a pellet and characterized for thermoelectric properties. We compare the thermoelectric properties of these samples with each other as well as the un-doped solvothermal tetrahedrite from our previous work, before and after ball-milling in a 1:1 mole to mole ratio with natural mineral (tennantite). We show that the electronic and thermal properties of tetrahedrite can be tuned by doping in-situ with zinc during our solvothermal synthesis.

## 5.2. EXPERIMENTAL: IN-SITU DOPING OF SOLVOTHERMAL TETRAHEDRITE

The solvothermal tetrahedrite is doped with zinc in-situ ( $\text{Cu}_{12-x}\text{Zn}_x\text{Sb}_4\text{S}_{13}$ ) by varying the ratio of zinc and copper precursors. For  $\text{Cu}_{12-x}\text{Zn}_x\text{Sb}_4\text{S}_{13}$  with  $x \sim 0.79$ , zinc nitrate hexahydrate (0.297 mmol) is combined with 1.412 mmol of basic copper nitrate ( $\text{Cu}_2(\text{OH})_3\text{NO}_3$ ), 0.4707 mmol of antimony sulfate, 12.88 mmol of thiourea, and 18.4 mL of ethylenediamine in a 23 mL Teflon vessel to prepare the reaction mixture. For  $\text{Cu}_{12-x}\text{Zn}_x\text{Sb}_4\text{S}_{13}$  with  $x \sim 1.15$ , zinc nitrate hexahydrate (0.4461 mmol) is combined in a 23 mL Teflon vessel with 1.338 mmol of basic copper nitrate ( $\text{Cu}_2(\text{OH})_3\text{NO}_3$ ) and the other reagents as described above. For  $\text{Cu}_{12-x}\text{Zn}_x\text{Sb}_4\text{S}_{13}$  with  $x \sim 1.40$ , zinc nitrate hexahydrate (1.19 mmol) is combined in a 23 mL Teflon vessel with 1.338 mmol of basic copper nitrate and the other reagents as described above.

The Teflon vessel is sealed and loaded into a stainless steel bomb and heated for 20–24 hours at 155 °C. The bomb is then allowed to cool naturally in the furnace with the door open and the power off. The product mixture is then transferred to a centrifuge tube, and isolation is carried out as described in Chapter 4 for the solvothermal tetrahedrite. This synthesis yields approximately 0.25 g per vessel (64% of theoretical yield of 0.3922 g). Multiple syntheses were carried out in parallel by heating up to four vessels at a time in one oven.

## 5.3. RESULTS AND DISCUSSION

**5.3.1. Synthesis and Characterization of Zinc-Doped Tetrahedrite: Optimizing the Solvothermal Procedure.** For our strategy to incorporate zinc into the solvothermal synthesis, we opted to avoid carbon containing ligands, like acetates, to avoid potential contamination with amorphous carbon that can arise due to hot-pressing. Further, we decided to avoid zinc chloride and other halogenide salts to prevent accidental doping of the product. This decision was based on the high resistivity and chloride contamination observed with the use of copper and antimony chloride precursors in our previous work, as described in Chapter 4. For our zinc source, zinc

nitrate hexahydrate is chosen because (1) leftover reagent would be water-soluble, (2) nitrate ions are already present in the synthesis from the basic copper nitrate reagent as a spectator ion, and (3) the zinc is already divalent as in the desired product,  $\text{Cu}_{12-x}\text{Zn}_x\text{Sb}_4\text{S}_{13}$ .

We adapted our solvothermal synthesis from Chapter 4 to incorporate zinc. The previously described synthesis utilized a reaction mixture of a stoichiometric ratio of basic copper nitrate ( $\text{Cu}_2(\text{OH})_3\text{NO}_3$ ) to antimony(III) sulfate along with a 300% molar excess of thiourea in ethylenediamine. The mixture was then placed in a 23 mL Teflon vessel that is sealed in a stainless steel bomb, and multiple bombs are heated in parallel for 20–24 hour at 155°C in a box furnace as described in Chapter 4.

We targeted  $\text{Cu}_{12-x}\text{Zn}_x\text{Sb}_4\text{S}_{13}$  with  $x \sim 1$  by in-situ doping in order to compare the performance of solvothermally prepared materials with the doped samples prepared by mixing solid state tetrahedrite with natural mineral or by doping the solid state tetrahedrite in-situ with zinc.<sup>2-3</sup> To favor zinc incorporation, we adjusted the ratio of zinc to copper to result in a reaction mixture with a stoichiometry of  $\text{Cu}_{10.9}\text{Zn}_{1.1}\text{Sb}_4\text{S}_{13}$  (instead of  $x = 1$ ) using 10.5 % as many zinc as copper moles. The synthesis was repeated several times (yield ~ 0.25 g per vessel), heating up to four vessels in parallel, to prepare several grams worth of tetrahedrite. The structural characteristics of each batch is investigated by XRD, and the composition is determined by ICP-MS. Diffraction patterns and elemental compositions are displayed for several repetitions of this synthesis (Figure 5.1).

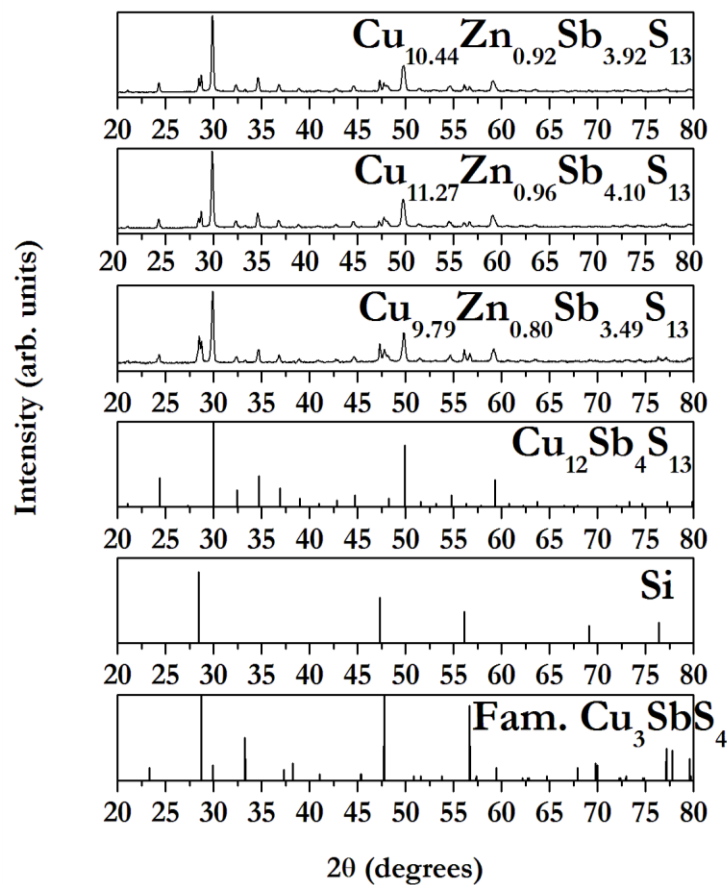


**Figure 5.1** XRD pattern for the tetrahedrite product from several runs of the solvothermal synthesis. Reference patterns 42–0561 and 35–0581 are displayed for tetrahedrite ( $\text{Cu}_{12}\text{Sb}_4\text{S}_{13}$ ) and famatinite ( $\text{Cu}_3\text{Sb}_4\text{S}_4$ ), respectively. The ICP-MS determined composition, normalized to  $\text{S} = 13$ , is displayed for each product.

In the XRD diffraction patterns (Figure 5.1), the product exhibits the tetrahedrite peaks as well as peaks from famatinite ( $\text{Cu}_3\text{Sb}_4\text{S}_4$ ) impurities giving rise to a composition that fluctuates around  $x = 0.8$  for zinc. Thus, less zinc is incorporated than what would be expected based on the composition of the initial reaction mixture ( $\text{Cu}_{10.9}\text{Zn}_{1.1}\text{Sb}_4\text{S}_{13}$ ). Averaging the products from this synthesis resulted in the composition  $\text{Cu}_{11.16}\text{Zn}_{0.79}\text{Sb}_{3.99}\text{S}_{13}$ . This is essentially  $\text{Cu}_{12-x}\text{Zn}_x\text{Sb}_4\text{S}_{13}$  with 0.79 mole equivalents of zinc. In spite of the presence of the smaller zinc ion, there is no noticeable shift in the major peak of tetrahedrite in the diffraction pattern. The

products tend to be slightly copper poor, likely due to lower Cu:S ratio in famatinite. This is consistent with our observations on the native tetrahedrite as discussed in Chapter 4.

For the  $x = 1.15$  sample, we wanted to prepare a stoichiometry with slightly more zinc than  $x = 1$ . Due to the fact that an excess of zinc is required to achieve a given stoichiometry, we adjust the ratio of copper to zinc to target a  $\text{Cu}_{10.3}\text{Zn}_{1.7}\text{Sb}_4\text{S}_{13}$  stoichiometry by using a 16.7% as many zinc moles as copper moles. Therefore, the reaction mixture contains an excess of zinc compared to the desired stoichiometry of  $\text{Cu}_{10.85}\text{Zn}_{1.15}\text{Sb}_4\text{S}_{13}$ .

The powder X-ray diffraction patterns of several products are displayed in Figure 5.2 along with their compositions (determined from ICP-MS). The XRD pattern matches that of tetrahedrite but contains additional peaks from famatinite ( $\text{Cu}_3\text{Sb}_4\text{S}_4$ ). Like the products from the synthesis with  $x=0.79$ , these also exhibit a fluctuating composition from run to run, and less zinc is incorporated ( $x \sim 1.15$ ) than what would be expected based on stoichiometry  $\text{Cu}_{10.3}\text{Zn}_{1.7}\text{Sb}_4\text{S}_{13}$ . Again, there is no obvious shift in the major peak of tetrahedrite in the diffraction pattern, and the products are copper-poor.

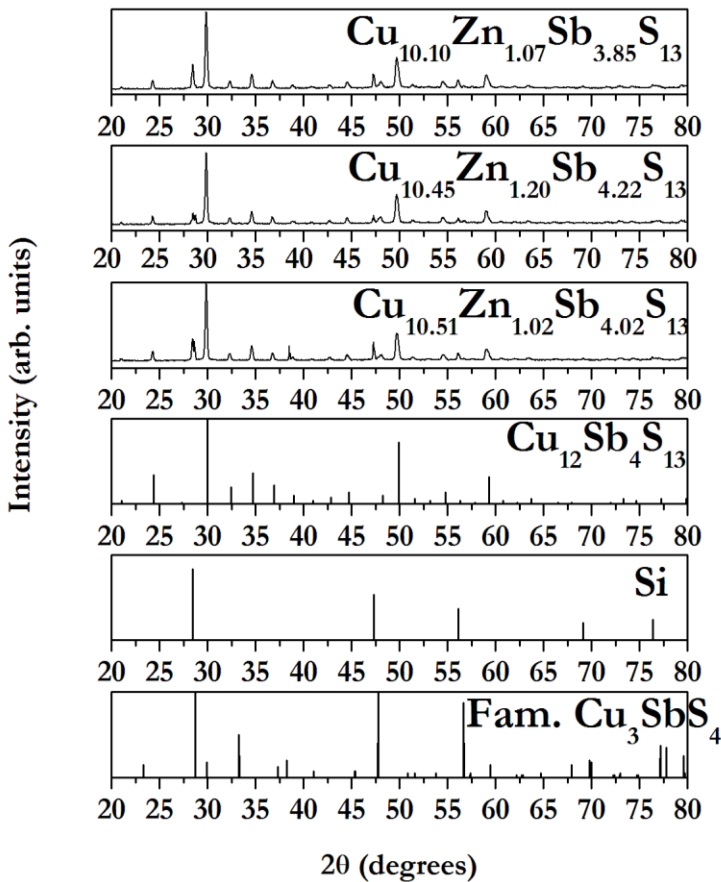


**Figure 5.2** XRD pattern for the tetrahedrite product from several runs of the solvothermal synthesis. Reference patterns 42–0561 and 35–0581 are displayed for tetrahedrite ( $\text{Cu}_{12}\text{Sb}_4\text{S}_{13}$ ) and famatinite ( $\text{Cu}_3\text{Sb}_4\text{S}_4$ ), respectively. The ICP-MS determined composition, normalized to  $\text{S} = 13$ , is displayed for each product.

For higher doping levels, we knew that a zinc mole contribution of  $x = 2$  would lead to insulating electrical properties, but we wanted to incorporate an intermediate amount of zinc to explore the properties of  $\text{Cu}_{12-x}\text{Zn}_x\text{Sb}_4\text{S}_{13}$  with  $x > 1$ . Therefore, the moles of zinc precursor are further increased. We employ a very large excess of zinc, 44.4 % as many zinc as copper moles, to target a composition of  $\text{Cu}_{8.3}\text{Zn}_{3.7}\text{Sb}_4\text{S}_{13}$ .

The powder X-ray diffraction patterns of the products from several repetitions of the synthesis are displayed in Figure 5.3 along with their compositions. The product still exhibits XRD peaks from both the tetrahedrite and famatinite ( $\text{Cu}_3\text{Sb}_4\text{S}_4$ ) diffraction patterns as well as

fluctuating compositions from run to run. In repeated syntheses, the zinc content fluctuates around x~1.4; therefore, we use these products later to prepare a material with an average stoichiometry of Cu<sub>10.99</sub>Zn<sub>1.40</sub>Sb<sub>4.01</sub>S<sub>13</sub>. Substitution of Zn<sup>2+</sup> for Cu<sup>2+</sup> would be expected to shift the tetrahedrite peaks towards lower 2-Theta, and a slight shift in the major peak of tetrahedrite is observed in the diffraction pattern. The shift to lower 2-Theta is indicative of zinc being incorporated into a solid solution with tetrahedrite. The product tends to be copper rich, as the sum of the mole equivalents from copper and zinc is greater than twelve. This suggests that some zinc could be either on the surface of the tetrahedrite as an amorphous phase or incorporated by interstitial doping. This is different than our previous samples, where the combined mole contribution from transition metals is generally decreased.

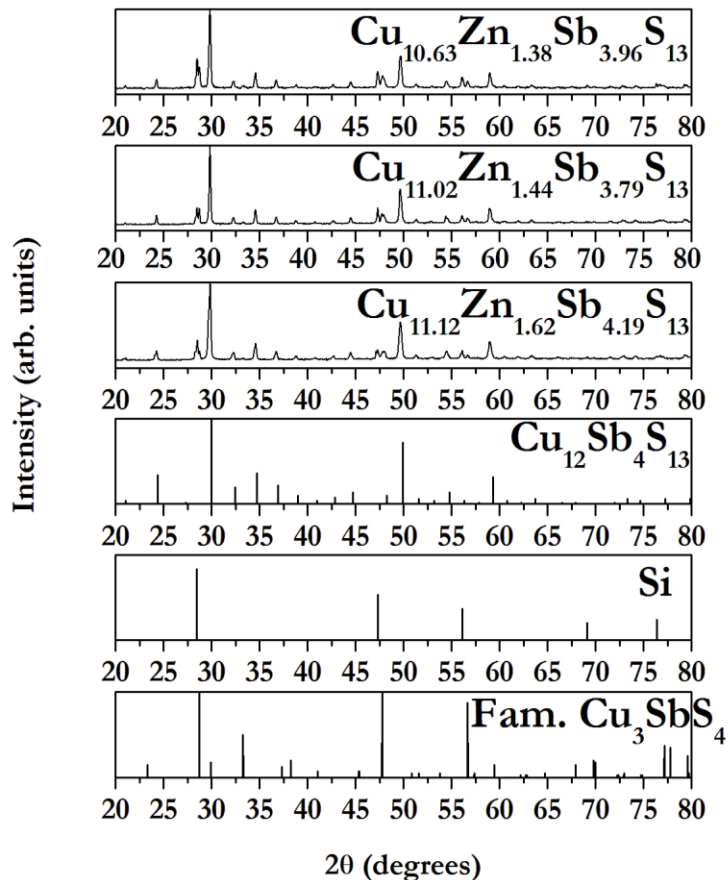


**Figure 5.3** XRD pattern for the tetrahedrite product from several runs of the solvothermal synthesis. Reference patterns 42–0561 and 35–0581 are displayed for tetrahedrite ( $\text{Cu}_{12}\text{Sb}_4\text{S}_{13}$ ) and famatinitite ( $\text{Cu}_3\text{Sb}_4\text{S}_4$ ), respectively. The ICP-MS determined composition, normalized to S = 13, is displayed for each product.

Syntheses for each target composition for solvothermal tetrahedrite result in fluctuating compositions. Therefore, samples are combined in appropriate amounts to obtain the composition of  $x = 0.79$ ,  $1.15$ , or  $1.40$ . For example, products from the synthesis used to prepare the  $x = 0.79$  composition are combined to obtain a ratio of Sb : S of  $3.99 : 13$  (scaled to 13 sulfur) for a formula of  $\text{Cu}_{11.16}\text{Zn}_{0.79}\text{Sb}_{3.99}\text{S}_{13}$  (Table 5.1) prior to hot-pressing. Likewise, to prepare the  $x = 1.15$  and  $x = 1.40$  samples, products from the  $x = 1.15$  or  $x = 1.40$  synthesis are similarly combined in appropriate amounts to result in average compositions of

$\text{Cu}_{10.46}\text{Zn}_{1.15}\text{Sb}_{4.09}\text{S}_{13}$  (Table 5.2) and  $\text{Cu}_{10.99}\text{Zn}_{1.40}\text{Sb}_{4.01}\text{S}_{13}$  (Table 5.3 ), respectively prior to hot-pressing.

**Table 5.1** Compositions for many products from the solvothermal synthesis for production of the  $x = 0.79$  zinc-doped tetrahedrite are determined by ICP-MS. Mole equivalents of Sb and Cu are scaled assuming 13 mole equivalents of sulfur. The tetrahedrite products are combined and the weighted average of Cu, Zn, and Sb moles are listed below along with the mass of the combined samples.

Sample	Cu	Zn	Sb	grams	
11-16-14 1	10.05	1.07	3.78	0.1878	
11-16-14 4	10.44	0.92	3.92	0.2007	
11-24-14 1	11.27	0.96	4.10	0.2511	
11-24-14 2	10.97	0.65	3.94	0.2411	
11-24-14 3	9.88	0.55	3.41	0.2399	
11-24-14 4	9.79	0.80	3.49	0.2603	
12-02-14 2	10.47	0.66	3.76	0.2618	
12-02-14 4	11.02	0.99	3.78	0.1984	
12-05-14 3	12.31	0.49	4.54	0.2188	
12-05-14 4	12.33	0.88	4.71	0.2370	
1-28-15 1	12.44	0.69	4.44	0.2317	
1-28-15 2	12.76	0.84	4.32	0.2293	
1-28-15 3	10.31	0.86	3.48	0.1802	
1-28-15 4	12.04	0.80	4.11	0.2511	
Weighted avg	11.16	0.79	3.99	Total grams	3.1892

**Table 5.2** Compositions for many products from the solvothermal synthesis for production of the  $x = 1.15$  zinc-doped tetrahedrite are determined by ICP-MS. Mole equivalents of Sb and Cu are scaled assuming 13 mole equivalents of sulfur. The tetrahedrite products are combined and the weighted average of Sb moles and Cu moles are listed below along with the mass of the combined samples.

Sample	Cu	Zn	Sb	grams	
9-19-14 1	10.10	1.07	3.85	0.2062	
9-19-14 2	10.35	1.11	3.96	0.2007	
9-19-14 3	10.73	1.25	4.26	0.2164	
9-19-14 4	10.46	1.04	4.04	0.1937	
10-06-14 2	10.45	1.20	4.22	0.209	
10-06-14 3	10.05	1.22	4.00	0.2187	
10-06-14 4	10.71	1.25	4.16	0.22	
10-11-14 2	10.64	1.13	4.25	0.21	
10-11-14 3	10.27	1.28	3.99	0.2063	
10-11-14 4	10.46	1.18	4.17	0.206	
10-16-14 1	10.88	1.08	4.14	0.167	
10-16-14 2	10.71	1.17	4.11	0.1682	
10-16-14 3	10.51	1.02	4.02	0.1696	
10-16-14 4	10.26	1.06	4.09	0.1877	
Weighted avg	10.46	1.15	4.09	Total grams	2.7795

**Table 5.3** Compositions for many products from the solvothermal synthesis for production of the  $x = 1.40$  zinc-doped tetrahedrite are determined by ICP-MS. Mole equivalents of Sb and Cu are scaled assuming 13 mole equivalents of sulfur. The tetrahedrite products are combined and the weighted average of Sb moles and Cu moles are listed below along with the mass of the combined samples.

Sample	Cu	Zn	Sb	grams	
7-30-14 1	10.63	1.38	3.96	0.2422	
7-30-14 2	10.90	1.39	3.98	0.2374	
7-30-14 3	11.23	1.28	4.06	0.2353	
7-30-14 4	11.03	1.36	4.04	0.2294	
8-27-14 1	11.07	1.33	3.74	0.2705	
8-27-14 2	11.02	1.44	3.79	0.2501	
8-27-14 3	11.02	1.20	3.79	0.286	
8-27-14 4	10.99	1.50	4.19	0.2282	
9-1-14 1	10.63	1.67	4.14	0.1048	
9-1-14 2	10.86	1.58	4.23	0.2235	
9-1-14 3	11.12	1.62	4.19	0.0967	
9-1-14 4	11.23	1.38	4.29	0.2231	
Weighted avg	10.99	1.40	4.01	Total grams	2.6272

Powder XRD patterns taken before and after hot-pressing are displayed below for  $\text{Cu}_{11.16}\text{Zn}_{0.79}\text{Sb}_{3.99}\text{S}_{13}$  (Figure 5.4),  $\text{Cu}_{10.46}\text{Zn}_{1.15}\text{Sb}_{4.09}\text{S}_{13}$  (Figure 5.5), and  $\text{Cu}_{10.99}\text{Zn}_{1.40}\text{Sb}_{4.01}\text{S}_{13}$  (Figure 5.6). In all cases, the pattern for each sample contains peaks from tetrahedrite and the famatinitite impurity. None of the three hot-pressed samples exhibit any obvious shift in the main tetrahedrite peak from the PDF pattern after hot-pressing despite the observation of a shift to low  $2\theta$  in samples used to prepare  $\text{Cu}_{10.99}\text{Zn}_{1.40}\text{Sb}_{4.01}\text{S}_{13}$ . Expanded views of the  $\text{Cu}_{10.99}\text{Zn}_{1.40}\text{Sb}_{4.01}\text{S}_{13}$  before and after hot-pressing are displayed in Figure 5.7. Once the samples for  $\text{Cu}_{10.99}\text{Zn}_{1.40}\text{Sb}_{4.01}\text{S}_{13}$  are mixed, there is a very slight shift (0.19) in the main peak ( $29.96 = 2\theta$ ) to higher  $2\theta$  (30.15). Hot-pressing increases the shift (0.23) to higher  $2\theta$  (30.19).

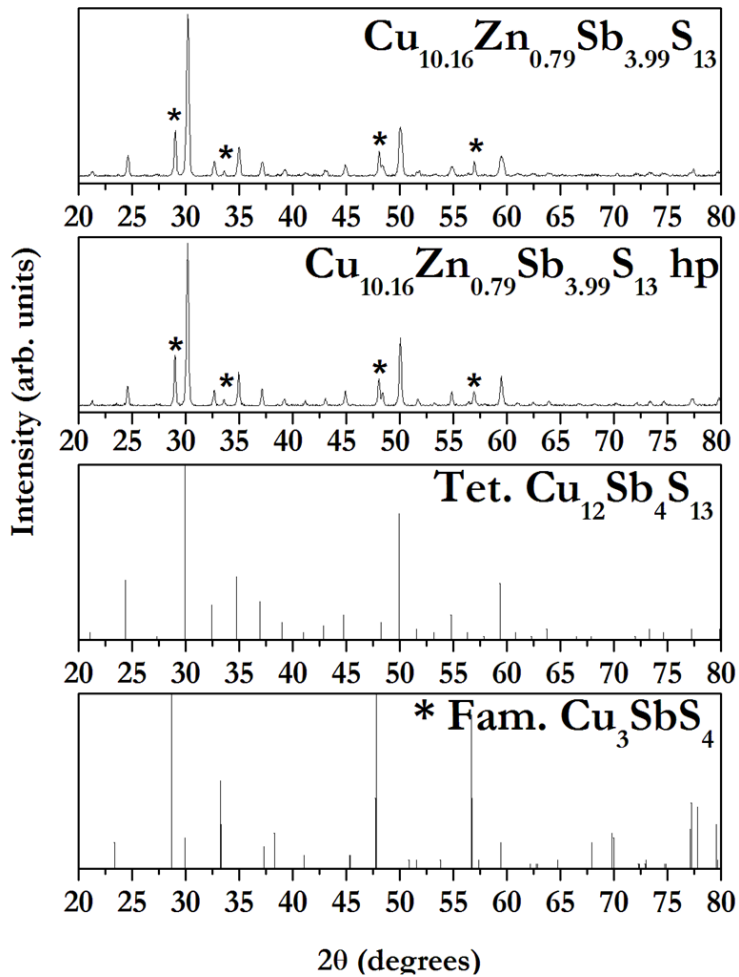


**Figure 5.4** XRD patterns for zinc-doped solvothermal tetrahedrite with composition  $\text{Cu}_{10.16}\text{Zn}_{0.79}\text{Sb}_{3.99}\text{S}_{13}$  (from mass averaging the samples with compositions determined by ICP-MS and normalized to S=13) before and after hot-pressing. Reference patterns 42-0561 and 35-0581 are displayed for tetrahedrite ( $\text{Cu}_{12}\text{Sb}_4\text{S}_{13}$ ), and famatinite, respectively. The \* marks prominent famatinite peaks.

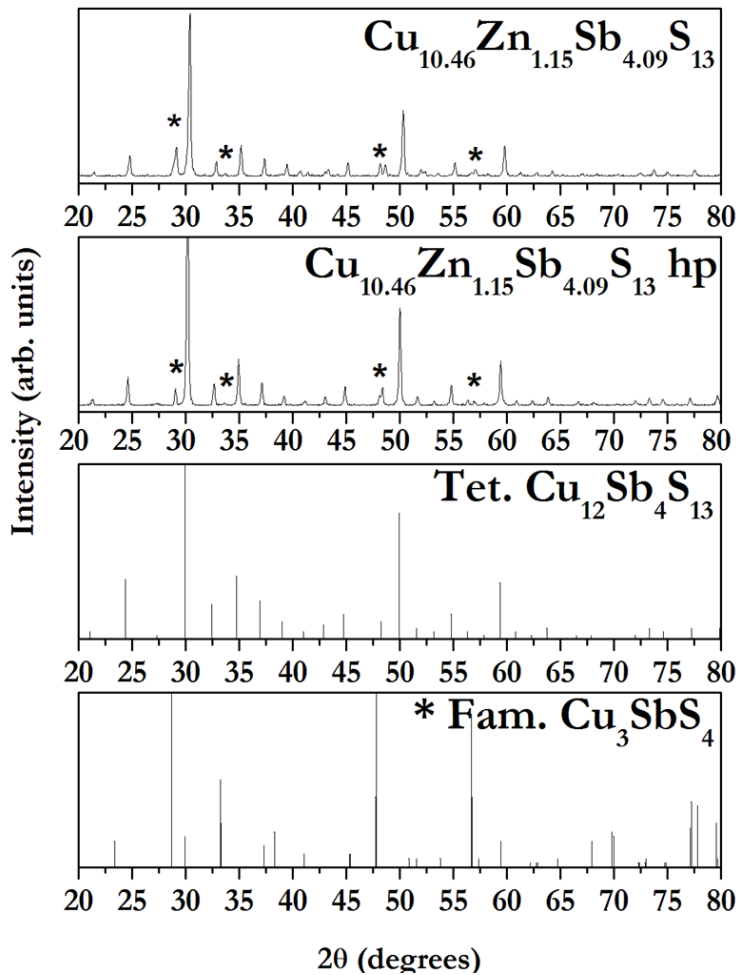


**Figure 5.5** XRD patterns for zinc-doped solvothermal tetrahedrite with composition  $\text{Cu}_{10.46}\text{Zn}_{1.15}\text{Sb}_{4.09}\text{S}_{13}$  (from mass averaging the samples with compositions determined by ICP-MS and normalized to S=13) before and after hot-pressing. Reference patterns 42-0561 and 35-0581 are displayed for tetrahedrite ( $\text{Cu}_{12}\text{Sb}_4\text{S}_{13}$ ), and famatinite, respectively. The \* marks prominent famatinite peaks.

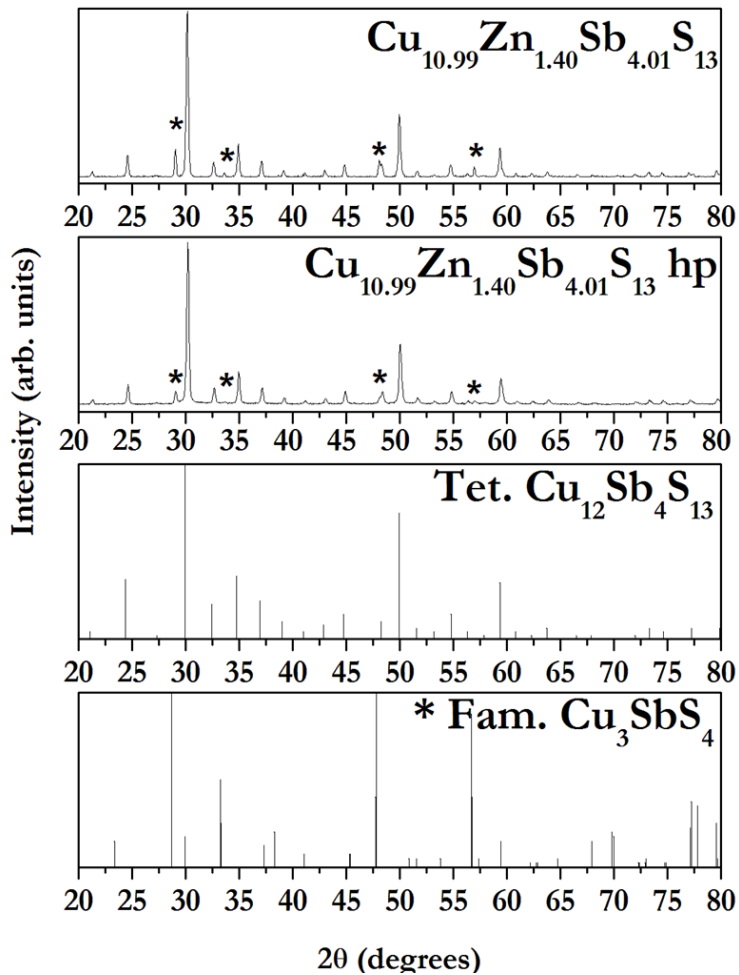


**Figure 5.6** XRD patterns for zinc-doped solvothermal tetrahedrite with composition  $\text{Cu}_{10.99}\text{Zn}_{1.40}\text{Sb}_{4.01}\text{S}_{13}$  (from mass averaging the samples with compositions determined by ICP-MS and normalized to S=13) before and after hot-pressing. Reference patterns 42-0561 and 35-0581 are displayed for tetrahedrite ( $\text{Cu}_{12}\text{Sb}_4\text{S}_{13}$ ), and famatinite, respectively. The \* marks prominent famatinite peaks.

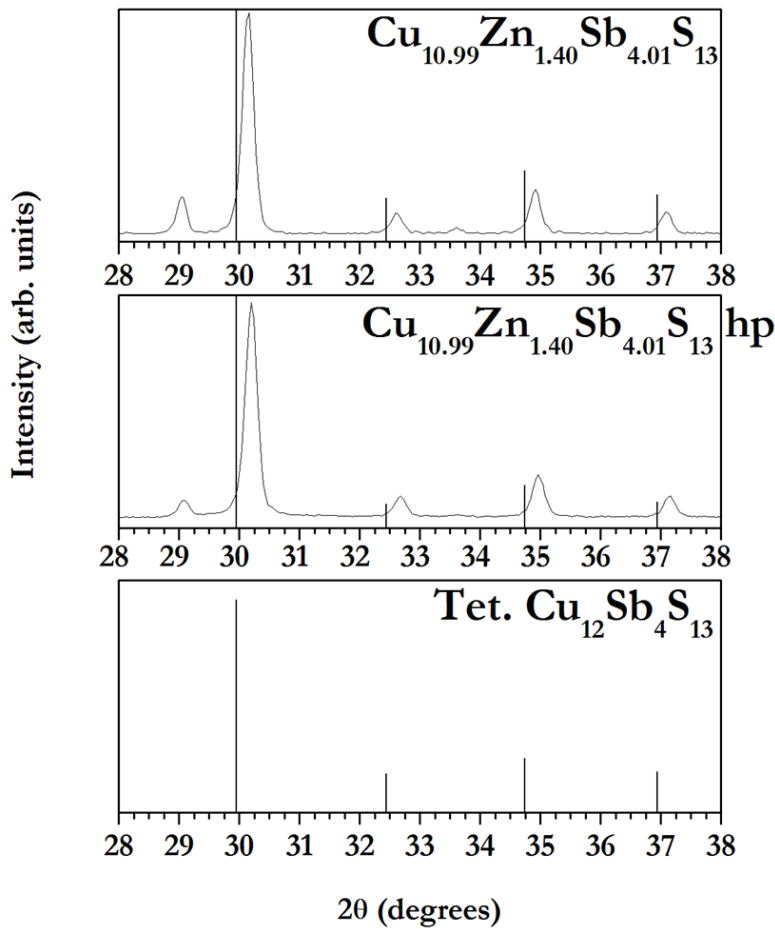


**Figure 5.7** Expanded views are displayed for the XRD patterns for zinc-doped solvothermal tetrahedrite with composition  $\text{Cu}_{10.99}\text{Zn}_{1.40}\text{Sb}_{4.01}\text{S}_{13}$  (from mass averaging the samples with compositions determined by ICP-MS and normalized to S=13) before and after hot-pressing. The reference pattern 42–0561 for tetrahedrite ( $\text{Cu}_{12}\text{Sb}_4\text{S}_{13}$ ) is overlaid on each pattern.

### 5.3.2. Thermoelectric Characterization of Tetrahedrite Prepared with Zinc-Doping.

Thermoelectric properties were determined from 300 to 720 K for the zinc-doped samples ( $\text{Cu}_{12-x}\text{Zn}_x\text{Sb}_4\text{S}_{13}$ ) after hot-pressing. Data from the solvothermal synthesis of tetrahedrite, prepared with 300% molar excess sulfur source in our previous work, alone and mixed in a 1:1 mole ratio with tennantite are displayed for comparison along with data from the solid state tetrahedrite. Thermopower values for the in-situ doped solvothermal samples from near room temperature to 720 K are displayed Figure 5.8 a. Our approach to dope in-situ by zinc increases the *p*-type

thermopower of the solvothermal tetrahedrite ( $130 \mu\text{VK}^{-1}$ ) with increasing mole contribution of zinc, demonstrating that the zinc is indeed functioning as a dopant. Thermopower increases with increasing Zn-doping, but the thermopower at high temperature (ca.720 K) is increased by 38% for  $x = 0.79$ , 48% for  $x = 1.15$ , and 72% for  $x = 1.40$  to values of 179, 192, and  $224 \mu\text{VK}^{-1}$ , respectively. Interestingly, the thermopower achieved for the  $x = 1.15$  sample is lower over most of the temperature range than that achieved for the 1:1 mole ratio mixture of either solvothermal or solid state tetrahedrite with tennantite from our previous work (Chapter 4). The zinc mole contribution in the tennantite mixed samples is lower at  $x = 0.9$ , which would lead one to expect lower thermopower values. However, the solvothermal tetrahedrite mixed with NM and the solid state tetrahedrite mixed with NM demonstrated higher thermopower values of  $202 \mu\text{VK}^{-1}$  and  $198 \mu\text{VK}^{-1}$ , respectively. Thus, the zinc from in-situ doping is less effective in raising the thermopower than zinc from the natural mineral. This may be due to the addition of molecular orbitals at the top of the valence band from minority spin states due to iron impurities in the natural mineral.<sup>77</sup>

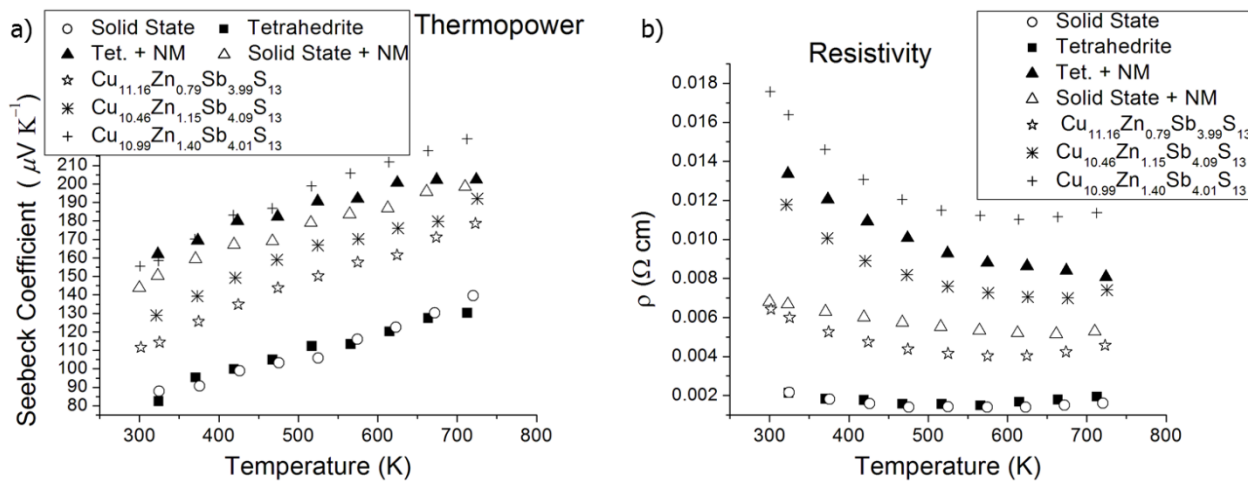


**Figure 5.8** Temperature-dependent Seebeck coefficient (a) and resistivity (b) values from room temperature to 720 K plotted as a function of temperature for the solid state tetrahedrite (Solid State), the solvothermal tetrahedrite (Tetrahedrite), the solvothermal tetrahedrite mixed with natural mineral (Tet. + NM), the solid state tetrahedrite mixed with NM (Solid State + NM), and the zinc doped solvothermal tetrahedrite samples (compositions calculated from determinations by ICP-MS). All samples were hot-pressed.

Resistivity data are displayed in Figure 5.8 b. Doping in-situ by zinc greatly increases the resistivity of the solvothermal tetrahedrite ( $1.9 \text{ m}\Omega\bullet\text{cm}$ ) with increasing mole contribution of zinc, as the Fermi Level rises towards the top of the valence band. The high temperature resistivity (at ca.720 K) is increased by 142% for  $x = 0.79$ , 289% for  $x = 1.15$ , and 500% for  $x = 1.40$  to values of 4.6, 7.4, and  $11.4 \text{ m}\Omega\bullet\text{cm}$ , respectively. Thus, at  $x = 1.40$  the Fermi Level has risen enough for the tetrahedrite metal to behave like a semiconductor.<sup>2-3</sup> These values are high in comparison to solid state tetrahedrite doped in-situ with zinc ( $\sim 2 \text{ m}\Omega\bullet\text{cm}$  for  $x = 0.5$  and nearly  $4 \text{ m}\Omega\bullet\text{cm}$  for  $x = 1.0$ ).<sup>2</sup> The resistivity of the  $x = 1.15$  sample is lower than that of the solvothermal tetrahedrite mixed in a 1:1 mole ratio with NM ( $8.1 \text{ m}\Omega\bullet\text{cm}$ ), demonstrating once again that more zinc is required for in-situ doping to achieve the same effect as using tennantite to dope. However, the solvothermal tetrahedrite doped in-situ to  $x = 1.15$  demonstrates a higher resistivity than the solid state sample doped by mixing with tennantite ( $5.3 \text{ m}\Omega\bullet\text{cm}$ ).

The electrical properties of thermopower and resistivity determine the power factor,  $\alpha^2/\rho$ , displayed in Figure 5.9. Doping with zinc decreases the power factor in spite of the higher thermopower by increasing the resistivity. The power factor is decreased at high temperature (at ca.720 K) from that of the solvothermal tetrahedrite ( $8.8 \mu\text{Wcm}^{-1}\text{K}^{-2}$ ) by 20% for  $x = 0.79$ , 43% for  $x = 1.15$ , and 50% for  $x = 1.40$  to values of 7.0, 5.0, and  $4.4 \mu\text{Wcm}^{-1}\text{K}^{-2}$ , respectively. The power factors for  $x = 1.15$  and  $x = 1.40$  are quite close because the gain in thermopower for the  $x = 1.40$  sample is more than countered by the rise in resistivity. Interestingly, the high temperature power factor for the  $x = 0.79$  sample is very close to that of the high performing 1:1 mixture of solid state tetrahedrite with tennantite ( $7.4 \mu\text{Wcm}^{-1}\text{K}^{-2}$ ). However, this is achieved with a lower thermopower and slightly lower resistivity. For tetrahedrite, doping with zinc lowers the power factor, but does so by increasing the resistivity. While both of these changes

are detrimental to ZT, the higher resistivity translates to a lower electrical conductivity, leading to a lower thermal conductivity.

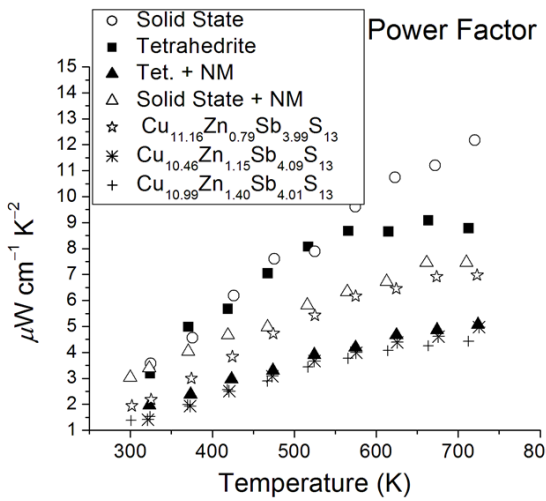


**Figure 5.9** Temperature-dependent Power Factor ( $\alpha^2/\rho$ ) values from room temperature to 720 K plotted as a function of temperature for the solid state tetrahedrite (Solid State), the solvothermal tetrahedrite (Tetrahedrite), the solvothermal tetrahedrite mixed with natural mineral (Tet. + NM), the solid state tetrahedrite mixed with NM (Solid State + NM), and the zinc doped solvothermal tetrahedrite samples (compositions calculated from determinations by ICP-MS).

The thermal conductivity,  $\kappa_{\text{tot}}$ , data for the samples are displayed in Figure 5.10. Due to the insulating nature of the  $x = 1.40$  sample, we did not determine its thermal conductivity. The  $\kappa_C$  is expected to make up a substantial portion of the thermal conductivity considering that the  $\kappa_L$  is only  $0.4 \text{ W m}^{-1} \text{ K}^{-1}$  in pure tetrahedrite.<sup>2-3</sup> Therefore, the thermal conductivity is expected to decrease with increasing zinc content and resistivity. The  $\kappa_{\text{tot}}$  decreases by 20% (to  $0.8 \text{ W m}^{-1} \text{ K}^{-1}$ ) for the  $x = 0.79$  and  $1.15$  samples at  $\sim 720 \text{ K}$ . The similarity of these values is unexpected considering the 61% increase in resistivity from the  $x = 0.79$  sample to the  $1.15$  sample. These values match the  $0.8 \text{ W m}^{-1} \text{ K}^{-1}$  reported for solid state tetrahedrite doped in-situ with zinc at  $x = 1.0$ .<sup>2</sup>

Whether grown solvothermally or by solid state, the  $\kappa_{\text{tot}}$  values of the comparatively zinc-doped samples are much higher than the  $0.53$  or  $0.43 \text{ W m}^{-1} \text{ K}^{-1}$  for a mix of natural mineral with the solid state or solvothermal tetrahedrite (reported in Chapter 4). This difference is not

explained by resistivity, as the resistivity of the  $x = 0.79$  sample ( $4.6 \text{ m}\Omega\bullet\text{cm}$ ) is only 13% lower than that reported for the mix of solid state tetrahedrite with NM ( $5.3 \text{ m}\Omega\bullet\text{cm}$ ). A similar phenomenon appears in the  $x = 1.15$  sample versus the previously reported mixture of solvothermal tetrahedrite with NM. The  $x = 1.15$  sample contains more zinc, and exhibits slightly lower resistivity ( $7.4 \text{ m}\Omega\bullet\text{cm}$ ) than that of the mix of solvothermal tetrahedrite with NM ( $8.1 \text{ m}\Omega\bullet\text{cm}$ ), but demonstrates nearly twice the thermal conductivity.

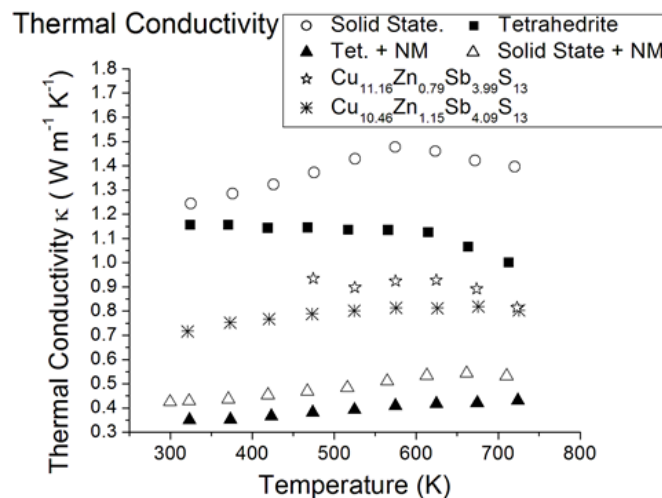


**Figure 5.10** Temperature-dependent thermal conductivity values from room temperature to 720 K plotted as a function of temperature for the solid state tetrahedrite (Solid State), the solvothermal tetrahedrite (Tetrahedrite), the solvothermal tetrahedrite mixed with natural mineral (Tet. + NM), the solid state tetrahedrite mixed with NM (Solid State + NM), and the zinc doped solvothermal tetrahedrite samples (compositions calculated from determinations by ICP-MS).

While about  $\sim 0.1$  mol equivalents of  $\text{Fe}^{3+}$  would be substituted for copper in these mixed materials, the similar resistivity values for the  $x = 0.79$  sample and the mix of solid state tetrahedrite with NM suggest that electronics are not responsible for the lower thermal conductivity. Likewise, the similar resistivity values of the  $x = 1.15$  sample and the mix of solvothermal tetrahedrite with NM leads to the same conclusion. The largest difference in composition between the NM ( $\text{Cu}_{10.0}\text{Zn}_{1.8}\text{Fe}_{0.2}\text{As}_{2.7}\text{Sb}_{1.3}\text{S}_{13}$ ) and synthetic tetrahedrite ( $\text{Cu}_{12}\text{Sb}_4\text{S}_{13}$ ) is the large amount of arsenic substituted for antimony. Rather than upset the unique mechanism responsible for the low  $\kappa_L$  of tetrahedrite, like substitution of antimony<sup>76</sup> by

tellurium, the arsenic may be lowering the thermal conductivity by acting as a mass impurity. Arsenic only contains 62% as much mass as antimony, so the frequency of phonons from vibrations in unit cells containing arsenic would be different, and may interfere with those already present in tetrahedrite. Destructive interference of phonons would be expected to lower thermal conductivity.<sup>34</sup>

We observed that zinc from in-situ doping is less effective at raising the thermopower for our solvothermal tetrahedrite than zinc from the natural mineral. This is likely due to the contributions to the Fermi Level and the band diagram by iron when tennantite is used as the source of zinc.<sup>79</sup> The iron plays the dual roles of adding electronic states at the top of the valence band where the density of states is very low, and also contributing one more electron to the Fermi Level than zinc. This would help zinc raise the Fermi Level towards the narrow peak at the top of the valence band, increasing thermopower.

In contrast to the behavior of the thermopower, in-situ doping of the solvothermal tetrahedrite results in higher resistivity values than solid state tetrahedrite doped by mixing with tennantite. However, the in-situ doping of solvothermal tetrahedrite leads to lower resistivity than doping solvothermal tetrahedrite by mixing it with tennantite. The common denominator here is that doping solvothermal tetrahedrite in-situ results in higher resistivity than solid state materials doped to similar levels (even with tennantite) and doping solvothermal tetrahedrite with tennantite increases the resistivity even further. Therefore, the use of solvothermal tetrahedrite in place of solid state leads to increased resistivity. This suggests that the crystalline famatinitite impurities in the solvothermal tetrahedrite play a role, as they are absent in the solid state material.

The temperature dependent ZT values are plotted for each sample in Figure 5.11. The incorporation of too much zinc in the  $x = 1.15$  sample decreases the ZT (0.45) at high temperature (720 K) by 29% from that of the solvothermal tetrahedrite ( $ZT = 0.63$ ) due to greatly increased resistivity and a decreased power factor combined with a relatively moderate decrease in thermal conductivity. The  $x = 0.79$  sample possesses nearly the same zinc composition ( $x = 0.9$ )<sup>3</sup> as the best performing mixture of zinc-rich natural mineral and solid state tetrahedrite, yet the ZT is virtually unchanged at 0.62 from that of the solvothermal tetrahedrite (0.63). Thus, the moderately decreased thermal conductivity is only sufficient to compensate for the increased resistivity and lower power factor without increasing ZT. This performance is low in comparison to solid state tetrahedrite doped in-situ with zinc. For the solid state material,  $x = 0.5$  results in a ZT of 1, due mostly to lower resistivity than that demonstrated by either of the solvothermal tetrahedrites with in-situ doping.<sup>2</sup> For the in-situ, zinc-doped solid state tetrahedrite with  $x = 1$ , a relatively large ZT of 0.8 was reported due to slightly lower thermal conductivity and resistivity values than that determined for our  $x = 0.79$  sample.

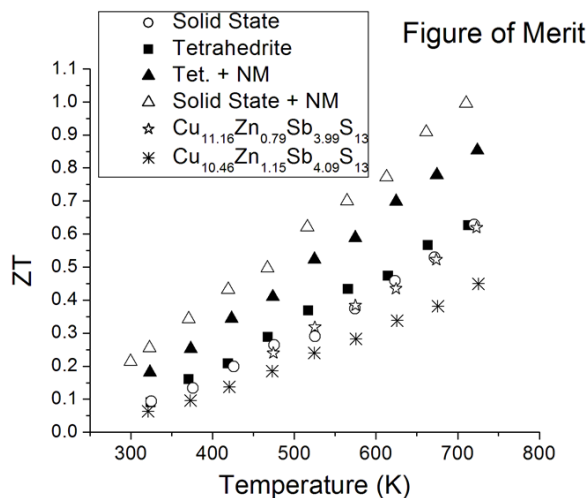


**Figure 5.11** Temperature-dependent thermoelectric figure of merit, ZT, values from room temperature to 720 K plotted as a function of temperature for the solid state tetrahedrite (Solid State), the solvothermal tetrahedrite (Tetrahedrite), the solvothermal tetrahedrite mixed with natural mineral (Tet. + NM), the solid state tetrahedrite mixed with NM (Solid State + NM), and the zinc doped solvothermal tetrahedrite samples (compositions calculated from determinations by ICP-MS).

## 5.4. CONCLUSIONS

We adapted our solvothermal synthesis of tetrahedrite for in-situ Zn-doping to prepare a range of  $\text{Cu}_{12-x}\text{Zn}_x\text{Sb}_4\text{S}_{13}$  with  $x=0.79-1.4$ . These doped tetrahedrites are characterized for phase, composition, and thermoelectric properties for comparison to solid state and solvothermal tetrahedrite doped with zinc by mixing with the natural mineral tennantite. The in-situ doped solvothermal tetrahedrites contain famatinite crystalline impurities and exhibit fluctuating compositions from batch to batch similarly to those discussed in our previous work (Chapter 4).

The in-situ zinc doping modulates the electrical properties, increasing the resistivity and thermopower with increased zinc content as predicted. However, the incorporated zinc is less effective at increasing the thermopower than zinc incorporated through ball-milling with the natural mineral. The reason that use of tennantite as a zinc source more effectively increases the thermopower may be the addition of electrons to the Fermi Level by Fe-doping in tennantite.

Thermal conductivity is decreased for our in-situ doped solvothermal tetrahedrite ( $x=0.79$  and 1.15) to the same level as that reported for solid state tetrahedrite doped with zinc in-situ to  $x = 1$ . We note that neither method of zinc doping is as effective at decreasing the thermal conductivity as doping by mixing with tennantite, and that differences in resistivity do not account for this. We suggest that the  $\text{As}^{3+}$  substituting for  $\text{Sb}^{3+}$  lowers the thermal conductivity by acting as a mass impurity to scatter phonons.

Although we demonstrate that in-situ Zn-doping of solvothermal tetrahedrite adjusts the thermoelectric properties, we do not see an increase in ZT. This is due to disproportionate increases in resistivity. In-situ doping with zinc for  $x = 0.79$  leads to our best performing doped solvothermal tetrahedrite, but the ZT is limited to that of pure solid state tetrahedrite. For this sample, we note a similar power factor to that of the best performing mixture of solid state

tetrahedrite and tennantite. However, our sample does not exhibit the low thermal conductivity of the mixture of tennantite with solid state tetrahedrite, despite a higher resistivity. We attribute this to the unique decreases in thermal conductivity that occur when using tennantite as the zinc source due to As<sup>3+</sup> substituting for Sb<sup>3+</sup>.

## CHAPTER 6 : CONCLUSIONS AND PROSPECTUS

### 6.1. CONCLUSIONS

Thermoelectric materials hold promise as a green technology for energy generation, capable of converting waste heat without moving parts from a variety of sources from manufacturing plants, to vehicles' exhaust systems, to space station generators.<sup>1, 19, 31-33</sup> In addition to power generation, thermoelectric materials are applicable for portable cooling through the Peltier effect.<sup>37, 39</sup> Thermoelectric properties are quantified with a ZT value according to the equation  $ZT = T\alpha^2\sigma/\kappa_{tot}$ . The ZT consists of the Seebeck coefficient (a.k.a. thermopower),  $\alpha = -\Delta V/\Delta T$ , the electrical conductivity,  $\sigma$ , and the total thermal conductivity,  $\kappa_{tot}$ . The  $\kappa_{tot}$  is the sum of the lattice ( $\kappa_L$ ) and electronic carrier ( $\kappa_C$ ) contributions to thermal conductivity. Traditional thermoelectric materials rely on the toxic and expensive element tellurium.<sup>19, 31-33, 22, 24-25, 27-29</sup> Materials containing heavy elements like tellurium have historically been used to favor low thermal conductivity by increasing the mean atomic mass ( $A$ ) due to the proportionality of lattice thermal conductivity ( $\kappa_L$ ) to  $\frac{1}{A^{7/6}}$ .<sup>21</sup> This approach targets high figure of merit due to the proportionality of ZT to  $\frac{1}{\kappa_{tot}}$ . Despite the incorporation of toxic heavy elements and complex syntheses<sup>2-9</sup> to lower thermal conductivity, including nanostructuring strategies like superlattices,<sup>35-36, 37-39</sup> ball-milling and hot-pressing previously prepared materials,<sup>43-45</sup> and precipitation of endotaxially embedded nanocrystals from a melt of the elements,<sup>10, 49-52</sup> the highest ZT values for state-of-the-art materials range from 1.1 for mixed nanocrystals of  $Bi_2Te_3$  and  $Sb_2Te_3$ , 1.4 for ball-milled  $BiSbTe$  alloy, 2.2 for  $PbTe$  with  $SrTe$  inclusions to 2.6 for the newly explored  $SnSe$  (single crystals).<sup>15, 44, 103-104</sup> To put this into perspective, most state-of-the-art thermoelectric materials have a ZT ~0.8–1.0, and materials

with a ZT of 0.8 are capable of converting heat to electricity at ~6% efficiency.<sup>19</sup> The increase in ZT for PbTe at high temperatures (915 K) to 2.2 is estimated to increase this efficiency to 16–20%.<sup>103</sup> A ZT of 4 would be required in order to compete with the efficiency of alternative energy sources like geothermal or solar power; meanwhile, a ZT of 20 is required to compete with coal.<sup>1</sup>

After many decades of research, the field of thermoelectric materials is shifting toward less toxic, more plentiful elements and cheaper processes to make thermoelectric technology more accessible, even at lower performances. Copper sulfides and selenides like CuInSe<sub>2</sub>, CuInS<sub>2</sub>, and CuAgSe<sub>2</sub> show promise as alternative thermoelectrics, but so far exhibit maximum ZT values up to 0.55 at 700 K.<sup>70-72</sup> The tetrahedrite mineral, Cu<sub>12</sub>Sb<sub>4</sub>S<sub>13</sub>, has shown particular promise as a new thermoelectric material, achieving low lattice thermal conductivity ( $\kappa_L=0.4\text{Wm}^{-1}\text{K}^{-1}$  at 700 K) while consisting of Earth abundant elements.<sup>2-3</sup> This low lattice thermal conductivity occurs due to a changing vibration frequency with cell volume caused by a dynamic interaction between the partially inert lone pair on Sb<sup>3+</sup> and a trigonal planar Cu<sup>+</sup>.<sup>74-76</sup> This leads to destructive interference of phonons to reduce the thermal conductivity, for a maximum ZT of 0.6 at 720 K. The ZT can be improved by doping in-situ with a variety of transition metals as Cu<sub>1-x</sub>M<sub>x</sub>Sb<sub>4</sub>S<sub>13</sub>. For example, the Keszler group demonstrated that Mn<sup>2+</sup> can be substituted for copper to result in ZT values of 1.13 or 0.8 at 575 K for x = 1 or 2, respectively.<sup>81</sup> In addition, doping with Co<sup>2+</sup> (x = 2) increased ZT to 0.5 at 575 K. The ZT can also be increased by doping with Fe<sup>3+</sup> for a maximum of 0.8 at x = 0.5.<sup>2</sup> Doping in-situ with Zn<sup>2+</sup> leads to ZT values of 1 and 0.8 for x = 0.5 and x = 1, respectively.<sup>2</sup> In addition to doping in-situ with zinc, zinc-rich tennantite (Cu<sub>10.0</sub>Zn<sub>1.8</sub>Fe<sub>0.2</sub>As<sub>2.7</sub>Sb<sub>1.3</sub>S<sub>13</sub>) can be ball-milled with tetrahedrite to a doping level of x = 0.9 to achieve a maximum ZT~1 (700 K).<sup>3</sup> The problem

with use of tetrahedrite as a cost effective thermoelectric material is the high temperature, complicated, and time consuming synthesis that requires several days in a tube furnace (923 K) followed by two weeks of annealing (723 K) and multiple stages of ball-milling.<sup>2-3</sup>

This dissertation research sought to improve applicability of thermoelectric materials with a two prong approach: (1) Develop and employ a multi-gram synthesis of dispersible PbTe NCs to efficiently nanostructure PbTe from the bottom up and lower lattice thermal conductivity for improved ZT. Nanostructuring is pursued with the PbTe NCs themselves as well as incorporation of dispersible PbS NCs (pre-grown). Ligand stripping methods are adapted from nanocrystal-based thin-films with the goal of increasing electrical conductivity in our bottom-up nanostructured PbTe. (2) Develop a rapid, scalable, moderate temperature alternative to the solid state route of producing tetrahedrite with state of the art performance. To this end, we completely redesigned a solvothermal synthesis<sup>100</sup> of tetrahedrite with different metal precursors and solvent to avoid detrimental chloride doping. We further optimize the synthesis by adjustment of precursor ratios to modulate an impurity phase. Zinc doping, both by mixing with the natural mineral tennantite and in-situ, is explored to maximize ZT via increased thermopower and decreased carrier contribution to thermal conductivity ( $\kappa_C$ ).

In Chapter 3, we hypothesized that nanostructuring PbTe with pre-grown NCs would result in low lattice thermal conductivity ( $\kappa_L$ ), and that  $\kappa_L$  would be further lowered by incorporation of nanocrystalline PbS. We further hypothesized that the electrical conductivity of our nanostructured PbTe would be increased by removal of the insulating ligands (from hot-injection synthesis) via ligand stripping.<sup>5, 53, 55, 67-68</sup> To increase the practicality of such bottom-up nanostructured devices, we developed a gram-scale synthesis of dispersible PbTe NCs (25-50 nm) with a Scherrer size of 30 nm. The phase and Scherrer size were determined using powder

XRD, the composition was determined by EDS, and the size and morphology were observed using TEM.

To test the effect of nanostructuring on  $\kappa_L$ , our PbTe NCs were treated with methanol to remove excess ligand, annealed to remove solvent, and hot-pressed into pellets for thermoelectric characterization. We found that the crystallite size in the hot-pressed sample had increased to 60 nm. The thermal conductivity at room temperature was approximately equal to the  $\kappa_L$  due to low electrical conductivity, and, in spite of the limited crystallite growth, these values were significantly decreased to  $1.4 \text{ W m}^{-1} \text{ K}^{-1}$  (300 K) from that of bulk PbTe ( $\kappa_L = 2.0 \text{ W}\cdot\text{m}^{-1}\text{K}^{-1}$ )<sup>10</sup> but are high relative to the  $\kappa_L$  of  $0.75 \text{ W}\cdot\text{m}^{-1}\text{K}^{-1}$  reported previously for hot-pressed pellets of PbTe NCs (200 nm).<sup>13</sup> Our nanostructured PbTe is *n*-type with a thermopower of  $-210 \mu\text{V}\cdot\text{K}^{-1}$ , on par with a nanostructured pellet of PbTe,<sup>13</sup> but greatly increased from the optimally doped *n*-type solid state PbTe ( $-100 \mu\text{V}\cdot\text{K}^{-1}$ ).<sup>10, 24</sup> The electrical conductivity ( $3.2 \text{ S}\cdot\text{cm}^{-1}$ ) was at the low end for bulk PbTe because of the nanocrystalline nature and the lack of doping for optimal electronic properties<sup>12</sup> which can yield electrical conductivities up to  $\sim 2000 \text{ S cm}^{-1}$ .<sup>10</sup> Electrical conductivity values on the order of  $1 \text{ S}\cdot\text{cm}^{-1}$  are consistent with those reported for films of hydrazine treated PbTe NCs<sup>5, 55</sup> or nanowires,<sup>53</sup> but notably lower than the  $\sim 210 \text{ S}\cdot\text{cm}^{-1}$  reported for a pellet of PbTe NCs from a ligand free synthesis.<sup>13</sup> Low electrical conductivity leads to low ZT (0.003) in our nanostructured PbTe compared to bulk (ZT = 0.4 at 300 K).<sup>25</sup>

Although we had expected incorporation of PbS NCs to further lower the thermal conductivity, mixing PbTe and PbS NCs by incipient wetness before hot-pressing did not lead to a significant decrease in  $\kappa_L$  ( $1.3 \text{ W m}^{-1} \text{ K}^{-1}$ ). This is likely due to sintering of the PbS NCs to large sizes (40 nm Scherrer size), and a similar growth of PbTe crystallite size to that observed for our methanol washed PbTe NCs. The incorporation of PbS NCs seems to dope, decreasing

the magnitude of the thermopower ( $-160 \mu\text{V}\cdot\text{K}^{-1}$ ) while increasing the electrical conductivity (42 S cm $^{-1}$  at 300 K) toward more optimal values. This increase in electrical conductivity (and smaller *n*-type thermopower) with incorporation of PbS is consistent with previous work.<sup>10</sup> Despite the improved electrical conductivity versus our PbTe sample, the value is still quite low, leading to a low ZT (0.03 at 300 K). This illustrates the problem with nanostructuring thermoelectrics from the bottom-up in that electrical conductivities tend to be low when starting with ligand-capped NCs.

We hypothesized that ligand stripping would increase the electrical conductivity of our bottom-up nanostructured PbTe; however, this was not the case due to complications arising from uncontrolled doping and in-situ growth of PbS when ammonium sulfide is employed as the ligand stripping agent. The in-situ growth of PbS after ligand stripping PbTe with ammonium sulfide was unexpected. Sulfide-stripping or sulfide-stripping followed by iodide-stripping lead to PbS crystallite sizes of 60 nm or 70 nm, respectively. The 60 nm PbS lead to a very modest decrease in  $\kappa_L$  to 1.2 W m $^{-1}$  K $^{-1}$  compared to the 1.4 W m $^{-1}$  K $^{-1}$  determined for the methanol washed PbTe NCs, whereas the 70 nm PbS in the consecutively sulfide and iodide-stripped sample resulted in higher  $\kappa_L$  (1.7 W m $^{-1}$  K $^{-1}$ ) which coincided with a large PbTe crystallite size. Therefore, this in-situ growth of PbS does not lower the  $\kappa_L$  values due to the large size of the PbS crystallites formed. The doping is apparent from the large increases in *n*-type thermopower for the iodide-stripped sample ( $-540 \mu\text{V}\cdot\text{K}^{-1}$  at 300 K) and *p*-type thermopower for the sulfide-stripped sample ( $520 \mu\text{V}\cdot\text{K}^{-1}$ ). This indicates that iodide-stripping results in doping with excited electrons, while the sulfide-stripping dopes with holes. This uncontrolled doping lead to high thermopower values but further lowered the electrical conductivity, resulting in low ZT values.

Thus, this type of ligand stripping to passivate the surface Pb<sup>2+</sup> with an anion is not suitable for treatment of thermoelectric materials.

In Chapter 4, we developed a fast and scalable synthesis for a thermoelectric material consisting of Earth abundant elements, tetrahedrite (Cu<sub>12</sub>Sb<sub>4</sub>S<sub>13</sub>). The purpose in researching tetrahedrite is to improve the accessibility of a cost effective thermoelectric material by developing a synthesis suited for industrial production. We began with a solvothermal synthesis from the literature for which the thermoelectric properties of the product had not been reported. The benefits of the solvothermal method are moderate temperatures, decreased synthesis time, and scalability in comparison to solid state methods. Our strategy to improve the thermoelectric properties was to dope with zinc by ball-milling the solvothermal tetrahedrite with the zinc-rich natural mineral tennantite (Cu<sub>10.0</sub>Zn<sub>1.8</sub>Fe<sub>0.2</sub>As<sub>2.7</sub>Sb<sub>1.3</sub>S<sub>13</sub>) in a 1:1 molar ratio because this has been reported to achieve comparable ZT (~1) to optimally doped lead telluride.<sup>3, 24</sup> Before hot-pressing, the product from the literature solvothermal synthesis exhibited a complex powder XRD pattern due to multiple possible phase impurities. The material is sulfur-poor (Cu<sub>15.8</sub>Sb<sub>7.8</sub>S<sub>13</sub>) but contains micron-sized features with compositions of Cu<sub>13.2</sub>Sb<sub>4.6</sub>S<sub>13</sub>Cl<sub>0.8</sub> and Cu<sub>2.0</sub>S<sub>0.8</sub>. This suggests that one of the phase impurities could be a variation of Copper (I) sulfide and that the product is contaminated by chlorine in some form. This could be leftover reagent or doping. This material was hot-pressed alone and after mixing in a 1:1 molar ratio with the natural mineral to dope with zinc. Thermoelectric characterization near room temperature determined the ZT of the literature tetrahedrite to be low due to high resistivity. The sample of ball-milled literature tetrahedrite with the natural mineral exhibited even lower ZT due to very high resistivity. We suspected that the chloride may serve as an uncontrolled *n*-type dopant to raise the Fermi Level and fill the valence band. This would result in a semiconductor with high

resistivity. These results necessitated the design of a new solvothermal synthesis to avoid chloride contamination and improve stoichiometry.

We reasoned that chloride contamination could be completely avoided by using halogenide-free precursors. Based on our work with lead telluride, we endeavored to also avoid metal salts containing carbon-based counter-ions that could act as ligands and form amorphous carbon upon hot-pressing. We chose nitrate and sulfate as acceptable counter-ions because they are inorganic and do not form insoluble salts with antimony or copper cations. This lead us to antimony(III) sulfate and copper(II) nitrate hemi(pentahydrate). We desired a stoichiometric copper nitrate precursor; so, we changed this to the basic copper nitrate ( $\text{Cu}_2(\text{OH})_3\text{NO}_3$ ). These precursors were employed under the same conditions as the literature synthesis, but did not yield the tetrahedrite phase. Since the copper in tetrahedrite is primarily  $\text{Cu}^+$  we hypothesized that replacement of the  $\text{Cu}^+$  precursor in the literature synthesis with a  $\text{Cu}^{2+}$  precursor like basic copper nitrate might prevent the phase from forming. Therefore, the ethanol solvent in the literature synthesis was replaced with a reducing solvent, ethylendiamine.

These conditions lead to formation of the tetrahedrite phase and the impurity phase chalcostibite. We first employed 100 % excess thiourea, and then 300 % excess thiourea (based on the copper precursor) and found that the 300 % excess thiourea resulted in a different impurity phase, famatinite. To provide enough material for thermoelectric testing, we repeated the 100 % excess thiourea synthesis many times, heating our four solvothermal vessels in parallel for fast production. We found that the composition fluctuated. Therefore, we fine-tuned the overall composition by combining products from multiple repetitions of the synthesis for a mass average. This material was hot-pressed alone and after ball-milling with the natural mineral in a 1:1 molar ratio, and the resulting pellets were characterized near room temperature

for thermoelectric properties. We found that the ZT of the solvothermal tetrahedrite alone was low, but that ball-milling it with the natural mineral increased the ZT to near that of the solid state tetrahedrite.

These promising results encouraged us to produce enough of the next test sample for high temperature thermoelectric characterization, and we desired to see if there was any advantage to replacing the chalcostibite impurity with famatinite. Therefore, we repeated the 300 % excess thiourea synthesis numerous times, again heating multiple vessels in parallel to produce enough solvothermal tetrahedrite for thermoelectric testing at high temperature. Similarly to above, the composition fluctuated from product to product; therefore, multiple products were combined to result in a mass averaged composition consistent with tetrahedrite. This material is hot-pressed alone and after mixing in a 1:1 molar ratio with the natural mineral. The solvothermal tetrahedrite by itself demonstrated essentially the same ZT curve as that of solid state tetrahedrite over the temperature range measured, resulting in a ZT of 0.63 (720 K). Therefore, our approach of using the solvothermal method to quickly produce tetrahedrite with comparable ZT to that of solid state tetrahedrite was successful. We found that, like the solid state tetrahedrite, this solvothermal version could also be improved by mixing with the natural mineral, which increased the ZT to 0.85 (720 K).

Zinc doping of tetrahedrite is further explored in Chapter 5. We hypothesized that the solvothermal synthesis discussed in Chapter 4 could allow in-situ doping with zinc to tune the thermoelectric properties. We chose zinc nitrate hydrate as a source of  $Zn^{2+}$  for doping because it avoids halogenides that could lead to unintentional doping (as discussed in Chapter 4), lacks carbon-based ligands that can lead to amorphous carbon during hot-pressing, and leftover zinc precursor would be water soluble for easy removal.

Our goal was to produce Zn-doped tetrahedrite with  $x \sim 1$  for comparison to the mix of tetrahedrite with tennantite ( $x = 0.9$ ) discussed in Chapter 4 for solvothermal tetrahedrite and reported by Morelli *et al.* for solid state tetrahedrite.<sup>3</sup> To favor incorporation of zinc we adjusted the ratio of copper and zinc precursors to target a stoichiometry of  $\text{Cu}_{10.9}\text{Zn}_{1.1}\text{Sb}_4\text{S}_{13}$ . The synthesis was repeated many times (yield  $\sim 0.25$  g per synthesis) heating four vessels in parallel to produce enough material for high temperature thermoelectric testing. The product was determined to be zinc-doped tetrahedrite with a famatinite impurity. The compositions fluctuated from run to run, but less zinc is incorporated than the  $\text{Cu}_{10.9}\text{Zn}_{1.1}\text{Sb}_4\text{S}_{13}$  target. Products from multiple repetitions of the same synthesis were combined to achieve sufficient quantities for thermoelectric characterization at high temperature, resulting in an overall composition of  $\text{Cu}_{11.16}\text{Zn}_{0.79}\text{Sb}_{3.99}\text{S}_{13}$  by mass averaging. This is referred to as the  $x = 0.79$  sample. To achieve higher Zn-doping levels, we adjusted the ratio of copper to zinc to target stoichiometries of  $\text{Cu}_9\text{Zn}_3\text{Sb}_4\text{S}_{13}$  and  $\text{Cu}_{6.36}\text{Zn}_{5.64}\text{Sb}_4\text{S}_{13}$ . These syntheses were each repeated multiple times and products from the same synthesis were combined similarly to above to obtain mass-averaged compositions of  $\text{Cu}_{10.46}\text{Zn}_{1.15}\text{Sb}_{4.09}\text{S}_{13}$  ( $x = 1.15$ ) and  $\text{Cu}_{10.99}\text{Zn}_{1.40}\text{Sb}_{4.01}\text{S}_{13}$  ( $x = 1.40$ ). Thus, we prepared a series of samples for thermoelectric testing with a range of doping levels in the vicinity of  $x = 1$  for comparison to the mix of tetrahedrite with tennantite ( $x = 0.9$ ).<sup>3</sup>

The incorporated zinc serves as a dopant to modulate the thermoelectric properties as we hypothesized. The thermopower of the solvothermal tetrahedrite ( $130 \mu\text{VK}^{-1}$ ) is increased at high temperature (720 K) with increasing zinc for doping levels of  $x = 0.79$  ( $179 \mu\text{VK}^{-1}$ ),  $x = 1.15$  ( $192 \mu\text{VK}^{-1}$ ), and  $x = 1.40$  ( $224 \mu\text{VK}^{-1}$ ). The increased thermopower is accompanied by an increase in resistivity at high temperature (720 K) from that of solvothermal tetrahedrite (1.9 m $\Omega$ •cm) to 4.6 m $\Omega$ •cm, 7.4 m $\Omega$ •cm, and 11.4 m $\Omega$ •cm for  $x = 0.79$ , 1.15, and 1.40,

respectively. The increasing thermopower and resistivity with zinc content is consistent with doping behavior as the zinc contributes extra electrons to raise the Fermi Level towards the top of the valence band. However, doping in-situ with zinc does not increase the thermopower or resistivity as effectively as Zn-doping via ball-milling with tennantite. We attribute this to the fact that  $\text{Fe}^{3+}$  in the tennantite also adds extra electrons to raise the Fermi Level.

The thermal conductivity for the in-situ doped solvothermal tetrahedrite decreases at high temperature (720 K) with increased zinc content from that of solvothermal tetrahedrite ( $1.0 \text{ W m}^{-1} \text{ K}^{-1}$ ) to  $0.8 \text{ W m}^{-1} \text{ K}^{-1}$  for  $x = 0.79$  or  $x = 1.15$  (data not acquired for  $x = 1.40$  due to high resistivity). However, we found that zinc doping with tennantite more effectively decreases the thermal conductivity than in-situ doping of either the solid state or solvothermal tetrahedrites, and we suggest that the added decrease in thermal conductivity from mixing with tennantite may be due to the incorporated  $\text{As}^{3+}$  acting as a mass impurity to scatter phonons. The ZT of the  $x = 0.79$  sample (0.62) is approximately the same as the solvothermal tetrahedrite (0.63). The mixture of solid state tetrahedrite ball-milled in a 1:1 molar ratio with tennantite achieves a much higher ZT (unity) due to the lower thermal conductivity ( $0.5 \text{ W m}^{-1} \text{ K}^{-1}$ ). The higher level of in-situ Zn-doping of  $x = 1.15$  exhibits a lower ZT due to higher resistivity. Therefore, in spite of the ability to dope with zinc in-situ to adjust the thermoelectric properties, the ZT is not increased in these samples.

## 6.2. PROSPECTUS

Our investigation of bottom-up PbTe nanocomposites underscores the problem of low electrical conductivity (high resistivity) when starting with ligand-capped NCs. The ligands themselves, as well as the amorphous carbon they can form during hot-pressing, decrease the electrical conductivity.<sup>5, 53, 55, 67</sup> Ligand stripping of thin films of ligand-capped NCs with

hydrazine can improve very low electrical conductivities by orders of magnitude to values (at 300 K) such as  $0.4 \text{ S}\cdot\text{cm}^{-1}$  for iodine-doped PbTe NCs,<sup>5</sup>  $\sim 5 \text{ S}\cdot\text{cm}^{-1}$  for PbTe nanowires,<sup>53</sup> or  $4.8 \text{ S}\cdot\text{cm}^{-1}$  for a composite film of hydrazine treated PbTe and Ag<sub>2</sub>Te NCs.<sup>55</sup> In addition, similarly low electrical conductivities are reported for an ethanol treated thin film of PbTe nanowires ( $1.3 \text{ S}\cdot\text{cm}^{-1}$ )<sup>54</sup> and a pellet of phosphonic acid stripped PbTe NCs ( $1.3 \text{ S}\cdot\text{cm}^{-1}$ ).<sup>6</sup> The ZT values of the thin films are not reported, but the room temperature ZT of the pellet of phosphonic acid stripped PbTe NCs is quite low at 0.02 in comparison to bulk lead telluride at room temperature (ZT = 0.4).<sup>24-25</sup> These electrical conductivities are orders of magnitude lower compared to bulk lead telluride ( $300 \text{ S}\cdot\text{cm}^{-1}$ )<sup>12</sup> that can be optimally doped for much higher values ( $\sim 2000 \text{ S}\cdot\text{cm}^{-1}$ ).<sup>10</sup>

Thus, in comparison to other methods of nanostructuring PbTe, use of ligand-capped NCs is handicapped by low electrical conductivity. Higher ZT values are demonstrated for PbTe by starting with ligand-free NCs by attaining higher electrical conductivity while still lowering  $\kappa_L$ . For example, hot-pressing relatively large (200–400 nm) PbTe NCs from solution phase synthesis without ligands decreases  $\kappa_{\text{tot}}$  to  $0.75 \text{ W m}^{-1} \text{ K}^{-1}$  while maintaining an electrical conductivity of  $\sim 210 \text{ S}\cdot\text{cm}^{-1}$  for a ZT of 0.8 at 580 K.<sup>13</sup> Alternatively, a variation of LAST (Ag<sub>0.8</sub>Pb<sub>18+x</sub>SbTe<sub>20</sub>) synthesized by mechanical alloying decreased  $\kappa_L$  to 30% of that of PbTe due to micron sized crystallites containing 20 nm diameter precipitates inside for a ZT of 1.5 (673 K).<sup>46</sup>

Precipitation from a melt for endotaxial growth of nanocrystalline features leads to the highest ZT values in PbTe via lowering  $\kappa_L$  while retaining high electrical conductivity and further optimizing electrical properties through controlled doping. For example, LAST-*m* with nanocrystalline AgSbTe<sub>2</sub> in PbTe achieves ZT~1.7 at 700 K ( $\kappa_L \sim 0.4 \text{ W m}^{-1} \text{ K}^{-1}$ )<sup>49-50</sup> and SALT-*m* with nanocrystalline NaSbTe<sub>2</sub> in PbTe achieves ZT = 1.6 at 675 K ( $\kappa_L = 0.5 \text{ W m}^{-1} \text{ K}^{-1}$ ).<sup>51</sup>

Recent nanostructuring of PbTe by precipitation of SrTe nanocrystal inclusions leads to the highest ZT for PbTe of 2.2 (915 K) via maintaining reasonable electrical conductivity (~230 S·cm<sup>-1</sup>) and very low  $\kappa_L$  (~0.4 W m<sup>-1</sup> K<sup>-1</sup>) through incorporation of both nanocrystalline impurities and mesoscale grain boundaries.<sup>103</sup> The mesoscale grain boundaries are incorporated by mechanically processing the ingot into powder (<10 micron grains) followed by densification into a pellet by spark plasma sintering. Thus, nanostructuring via endotaxial growth of NCs in PbTe is the most effective route to high ZT in PbTe, and can be improved by processing the material into a powder followed by densification by SPS. However, the maximum ZT achieved for the PbTe system after decades of research is still well short of the target ZT of 4 for competition with alternative energy sources like geothermal technology or solar materials.

Widespread application of thermoelectric materials in the near future is not likely to be from very high ZT (> 4) materials, but rather, materials consisting of abundant elements that can be efficiently produced industrially. The harbinger of this shift is the Si/Ge alloy (Si<sub>0.8</sub>Ge<sub>0.2</sub>). Consisting of light elements and silicon-based, this nontraditional thermoelectric exhibits a maximum ZT of 0.6 (1000 K) with a very high  $\kappa_L$  (~5 W m<sup>-1</sup> K<sup>-1</sup>).<sup>37-39</sup> This is increased further to 0.72 at high temperature (1000 K) via ball-milling to greatly decrease the  $\kappa_L$ .<sup>45</sup> Growing a superlattice of SiGeC/Si on silicon wafer by molecular beam epitaxy can reduce the thermal conductivity down to (~3 W m<sup>-1</sup> K<sup>-1</sup> at 300 K).<sup>37-39</sup> The decrease in  $\kappa_L$  is due to lattice strain from the lattice mismatch of the layers of Si<sub>0.89</sub>Ge<sub>0.10</sub>Si<sub>0.01</sub> and Si.<sup>40</sup> This material is now being used for its Peltier Effect and applied in miniature cooling systems currently available for the public to order online.

With a focus on using Earth abundant elements to prepare thermoelectric materials for energy generation in a manner that can be adapted for industry, we developed a new

solvothermal synthesis for tetrahedrite. The advantageous qualities of tetrahedrite have led to several licensed patents as a thermoelectric,<sup>87-88</sup> and commercial manufacturing was recently begun by Alphabet Energy, Incorporated using solid state and ball-milling methods.

The new process reported in this dissertation could be viewed as an improvement on the literature solvothermal synthesis of tetrahedrite, for which thermoelectric properties had not been reported, but we have prepared and characterized this previously reported material and found the thermoelectric properties to be poor. Therefore, we replaced the metal precursors to improve the thermoelectric properties by avoiding chloride contamination, and this necessitated replacement of the solvent in order to obtain the tetrahedrite product.

The new synthesis that we designed serves as a rapid and scalable alternative to the state of the art solid state route of producing tetrahedrite, producing material that, while impure, still exhibits the same Figure of Merit (ZT) at operating temperatures (600-720 K). As an alternative to solid state routes to tetrahedrite, our process is superior because it does not require the use of a high temperature tube furnace and weeks of annealing. The yield of current solid state methods is restricted to about 4 g per tube furnace after several days of heating, followed by several weeks of annealing in a standard laboratory oven. Using our solvothermal process, we can heat multiple solvothermal vessels simultaneously in a box furnace or simple lab oven, requiring temperatures of only 155 °C for 24 hours. In addition to allowing parallel synthesis of multiple vessels, our process requires no stirring and is expected to be scalable to larger vessels. As an added advantage over solid state methods, our process uses metal salts as precursors rather than high purity elemental metals.

Like the solid state material, the ZT of tetrahedrite from our solvothermal process can be improved by ball-milling with the natural mineral tennantite in a 1:1 molar ratio to dope with

zinc for improved properties. This means that the moles of material synthesized by heating in the lab are ball-milled with the cheap, plentiful natural mineral to essentially double the moles of thermoelectric material. Thus prepared, our material exhibits a ZT of 0.85 at 724 K, which is slightly less than the ZT of 1.00 at 710 K exhibited by the similarly mixed solid state tetrahedrite. Further, our synthesis can be doped in-situ with zinc. Our goal with this approach was to be able to skip the ball-milling process altogether, eliminating the need for expensive high energy ball-milling equipment with limited capacities that could serve as a bottleneck in production. In-situ zinc doping would allow a true one-pot synthesis that could be scaled or heated in parallel. However, the zinc compositions that we tested for in-situ doping did not lead to better thermoelectric properties. This is likely due to the fact that we targeted the optimum zinc composition for tetrahedrite doped by ball-milling with tennantite ( $x = 0.9$ ). This is nearly twice the mole contribution of zinc for optimum in-situ doping ( $x = 0.5$ ). Therefore, further adjustment of the doping may be required. However, in the absence of a beneficial in-situ doping process, the solvothermal tetrahedrite could be ball-milled with the tennantite to increase the yield and ZT as described above for cost effective production. If the adaptation of Si/Ge systems for public use as microcoolers is any indication, then cost effective production of tetrahedrite could result in widely available thermoelectric devices for power generation.

## REFERENCES

1. Shakouri, A., Recent Developments in Semiconductor Thermoelectric Physics and Materials. *Annu. Rev. Mater. Res.* **2011**, *41*, 399-431.
2. Lu, X.; Morelli, D. T.; Xia, Y.; Zhou, F.; Ozolins, V.; Chi, H.; Zhou, X.; Uher, C., High Performance Thermoelectricity in Earth-Abundant Compounds Based on Natural Mineral Tetrahedrites. *Adv. Energy Mater.* **2013**, *3*, 342-348.
3. Morelli, D. T.; Lu, X., Natural Mineral Tetrahedrite as a Direct Source of Thermoelectric Materials. *Phys. Chem. Chem. Phys.* **2013**, *15*, 5762-5766.
4. Ibanez, M.; Zamani, R.; Gorsse, S.; Fan, J.; Ortega, S.; Cadavid, D.; Morante, J. R.; Arbiol, J.; Cabot, A., Core-Shell Nanoparticles as Building Blocks for the Bottom-Up Production of Functional Nanocomposites: PbTe-PbS Thermoelectric Properties. *ACS Nano* **2013**, *7*, 2573-2586.
5. Fang, H.; Luo, Z.; Yang, H.; Wu, Y., The Effects of the Size and Doping Concentration on the Power Factor of n-Type Lead Telluride Nanocrystals for Thermoelectric Energy Conversion. *Nano Lett.* **2014**, *14*, 1153-1157.
6. Scheele, M.; Oeschler, N.; Veremchuk, I.; Peters, S.; Littig, A.; Kornowski, A.; Klinke, C.; Weller, H., Thermoelectric Properties of Lead Chalcogenide Core-Shell Nanostructures. *ACS Nano* **2011**, *5*, 8541-8551.
7. Kovalenko, M. V.; Spokoyny, B.; Lee, J.; Sheele, M.; Weber, A.; Perera, S.; Landry, D.; Talapin, D. V., Semiconductor Nanocrystals Functionalized with Antimony Telluride Zintl Ions for Nanostructured Thermoelectric. *J. Am. Chem. Soc.* **2010**, *132*, 6686-6695.

8. Ganguly, S.; Zhou, C.; Morelli, D.; Sakamoto, J.; Brock, S. L., Synthesis and Characterization of Telluride Aerogels: Effect of Gelation on Thermoelectric Performance of  $\text{Bi}_2\text{Te}_3$  and  $\text{Bi}_{2-x}\text{Sb}_x\text{Te}_3$  Nanostructures. *J. Phys. Chem. C* **2012**, *116*, 17431-17439.
9. Liang, D.; Yang, H.; Finefrock, S. W.; Wu, Y., Flexible Nanocrystal-Coated Glass Fibers for High-Performance Thermoelectric Energy Harvesting. *Nano Lett.* **2012**, *12*, 2140-2145.
10. Androulakis, J.; Lin, C. H.; Kong, H. J.; Uher, C.; Wu, C. I.; Hogan, T.; Cook, B. A.; Caillat, T.; Paraskevopoulos, K. M.; Kanatzidis, M. G., Spinodal Decomposition and Nucleation and Growth as a Means to Bulk Nanostructured Thermoelectrics: Enhanced Performance in  $\text{Pb}_{(1-x)}\text{Sn}_{(x)}\text{Te}$ - $\text{PbS}$ . *J. Am. Chem. Soc.* **2007**, *129*, 9780-9788.
11. Kishimoto, K.; Koyanagi, T., Preparation of Sintered Degenerate n-Type PbTe with a Small Grain Size and its Thermoelectric Properties. *J. Appl. Phys.* **2002**, *92*, 2544-2549.
12. Heremans, J.; Thrush, C.; Morelli, D., Thermopower Enhancement in Lead Telluride Nanostructures. *Phys. Rev. B* **2004**, *70*, 5-12.
13. Cao, Y. Q.; Zhu, T. J.; Zhao, X. B., Low Thermal Conductivity and Improved Figure of Merit in Fine-Grained Binary PbTe Thermoelectric Alloys. *J. Phys. D: Appl. Phys.* **2009**, *42*, 015406-015406-6.
14. Jin, R.; Chen, G.; Pei, J., PbS/PbSe Hollow Spheres: Solvothermal Synthesis, Growth Mechanism, and Thermoelectric Transport Properties. *J. Phys. Chem. C* **2012**, *116*, 16207-16216.
15. Mehta, R. J.; Zhang, Y.; Karthik, C.; Singh, B.; Siegel, R. W.; Borca-Tasciuc, T.; Ramanath, G., A New Class of Doped Nanobulk High-Figure-of-Merit Thermoelectrics by Scalable Bottom-Up Assembly. *Nat. Mater.* **2012**, *11*, 233-240.

16. Sumithra, S.; Takas, N.; Nolting, W.; Sapkota, S.; Poudeu, P. P.; Stokes, K., Effect of NiTe Nanoinclusions on Thermoelectric Properties of  $\text{Bi}_2\text{Te}_3$ . *J. Electron. Mater.* **2012**, *41* (6), 1401-1407.
17. Santhanam, S.; Takas, N. J.; Nolting, W. M.; Poudeu, P. F. P.; Stokes, K. L., Effect of Sn Substitution on the Thermoelectric Properties of Nanostructured Bulk  $\text{Bi}_{2-x}\text{Sb}_x\text{Te}_3$  Alloy. In *Symposium I – Nanoscale Heat Transfer–Thermoelectrics, Thermophotovoltaics and Emerging Thermal Devices*, 2011; Vol. 1329.
18. Sumithra, S.; Takas, N. J.; Misra, D. K.; Nolting, W. M.; Poudeu, P. F. P.; Stokes, K. L., Enhancement in Thermoelectric Figure of Merit in Nanostructured  $\text{Bi}_2\text{Te}_3$  with Semimetal Nanoinclusions. *Adv. Energy Mater.* **2011**, *1* (6), 1141-1147.
19. Sootsman, J. R.; Chung, D. Y.; Kanatzidis, M. G., New and Old Concepts in Thermoelectric Materials. *Angew. Chem. Int. Ed.* **2009**, *48* (46), 8616-8639.
20. Kumar, G. S.; Prasad, G.; Pohl, R. O., Experimental Determinations of the Lorenz Number. *J. Mater. Sci.* **1993**, *28* (16), 4261-4272.
21. Keyes, R. W., High-Temperature Thermal Conductivity of Insulating Crystals: Relationship to the Melting Point. *Phys. Rev.* **1959**, *115* (3), 564-567.
22. Rowe, D. M., *CRC Handbook of Thermoelectrics*. CRC: Boca Raton, FL, 1995.
23. Chung, D.-Y.; Hogan, T. P.; Rocci-Lane, M.; Brazis, P.; Ireland, J. R.; Kannewurf, C. R.; Bastea, M.; Uher, C.; Kanatzidis, M. G., A New Thermoelectric Material:  $\text{CsBi}_4\text{Te}_6$ . *J. Am. Chem. Soc.* **2004**, *126* (20), 6414-6428.
24. Dughaish, Z. H., Lead Telluride as a Thermoelectric Material for Thermoelectric Power Generation. *Phys. B* **2002**, *322* (1–2), 205-223.

25. Ravich, Y. I.; Efimova, B. A.; Smirnov, I. A., *Semiconducting Lead Chalcogenides*. Plenum, New York, 1970; Vol. 5.
26. Heremans, J. P.; Jovovic, V.; Toberer, E. S.; Saramat, A.; Kurosaki, K.; Charoenphakdee, A.; Yamanaka, S.; Snyder, G. J., Enhancement of Thermoelectric Efficiency in PbTe by Distortion of the Electronic Density of States. *Science* **2008**, *321* (5888), 554-557.
27. Wood, C., Materials for Thermoelectric Energy Conversion. *Rep. Prog. Phys.* **1988**, *51* (4), 459-539.
28. Wolfe, R.; Wernick, J. H.; Haszko, S. E., Anomalous Hall Effect in AgSbTe<sub>2</sub>. *J. Appl. Phys.* **1960**, *31* (11), 1959-1964.
29. Irie, T., Thermoelectric Properties of the Single-Phase of AgSbTe<sub>2</sub>. *J. Phys. Soc. Jap.* **1962**, *17* (11), 1810-1811.
30. Ye, L.-H.; Hoang, K.; Freeman, A. J.; Mahanti, S. D.; He, J.; Tritt, T. M.; Kanatzidis, M. G., First-Principles Study of the Electronic, Optical, and Lattice Vibrational Properties of AgSbTe<sub>2</sub>. *Phys. Rev. B* **2008**, *77* (24), 245203-245203-6.
31. Placheova, S. K., Thermoelectric Figure of Merit of the System (GeTe)<sub>1-x</sub>(AgSbTe<sub>2</sub>)<sub>x</sub>. *Phys. Status Solidi A* **1984**, *83* (1), 349-355.
32. Cook, B. A.; Kramer, M. J.; Wei, X.; Harringa, J. L.; Levin, E. M., Nature of the Cubic to Rhombohedral Structural Transformation in (AgSbTe<sub>2</sub>)<sub>15</sub>(GeTe)<sub>85</sub> Thermoelectric Material. *J. Appl. Phys.* **2007**, *101* (5), 053715.
33. Cook, B.; Wei, X.; Harringa, J.; Kramer, M., In-Situ Elevated-Temperature TEM Study of (AgSbTe<sub>2</sub>)<sub>15</sub>(GeTe)<sub>85</sub>. *J. Mater. Sci.* **2007**, *42* (18), 7643-7646.

34. Vineis, C. J.; Shakouri, A.; Majumdar, A.; Kanatzidis, M. G., Nanostructured Thermoelectrics: Big Efficiency Gains from Small Features. *Adv. Mater.* **2010**, *22* (36), 3970-3980.
35. Venkatasubramanian, R.; Siivola, E.; Colpitts, T.; O'Quinn, B., Thin-Film Thermoelectric Devices with High Room-Temperature Figures of Merit. *Nature* **2001**, *413* (6856), 597-602.
36. Caylor, J.; Coonley, K.; Stuart, J.; Colpitts, T.; Venkatasubramanian, R., Enhanced Thermoelectric Performance in PbTe-Based Superlattice Structures from Reduction of Lattice Thermal Conductivity. *Appl. Phys. Lett.* **2005**, *87*, 023105-023105-3.
37. Fan, X.; Zeng, G.; Croke, E.; LaBounty, C.; Ahn, C.; Vashaee, D.; Shakouri, A.; Bowers, J., High Cooling Power Density SiGe/Si Micro-Coolers. *Electron. Lett.* **2001**, *37* (2), 126-127.
38. Vashaee, D.; Shakouri, A., Thermionic Power Generation at High Temperatures Using SiGe/Si Superlattices. *J. Appl. Phys.* **2007**, *101* (5), 053719.
39. Fan, X.; Zeng, G.; LaBounty, C.; Bowers, J. E.; Croke, E.; Ahn, C. C.; Huxtable, S.; Majumdar, A.; Shakouri, A., SiGeC/Si Superlattice Microcoolers. *Appl. Phys. Lett.* **2001**, *78* (11), 1580-1582.
40. Lee, S.; Cahill, D. G.; Venkatasubramanian, R., Thermal Conductivity of Si-Ge Superlattices. *Appl. Phys. Lett.* **1997**, *70* (22), 2957-2959.
41. Capinski, W. S.; Maris, H. J., Thermal Conductivity of GaAs/AlAs Superlattices. *Physica B: Cond. Matt.* **1996**, *219–220*, 699-701.
42. Koga, T.; Sun, X.; Cronin, S. B.; Dresselhaus, M. S., Carrier Pocket Engineering to Design Superior Thermoelectric Materials Using GaAs/AlAs Superlattices. *Appl. Phys. Lett.* **1998**, *73* (20), 2950-2952.

43. Zhao, X. B.; Ji, X. H.; Zhang, Y. H.; Zhu, T. J.; Tu, J. P.; Zhang, X. B., Bismuth Telluride Nanotubes and the Effects on the Thermoelectric Properties of Nanotube-Containing Nanocomposites. *Appl. Phys. Lett.* **2005**, *86* (6), 062111.
44. Poudel, B.; Hao, Q.; Ma, Y.; Lan, Y.; Minnich, A.; Yu, B.; Yan, X.; Wang, D.; Muto, A.; Vashaee, D.; Chen, X.; Liu, J.; Dresselhaus, M. S.; Chen, G.; Ren, Z., High-Thermoelectric Performance of Nanostructured Bismuth Antimony Telluride Bulk Alloys. *Science* **2008**, *320* (5876), 634-638.
45. Dresselhaus, M. S.; Chen, G.; Tang, M. Y.; Yang, R. G.; Lee, H.; Wang, D. Z.; Ren, Z. F.; Fleuriol, J. P.; Gogna, P., New Directions for Low-Dimensional Thermoelectric Materials. *Adv. Mater.* **2007**, *19* (8), 1043-1053.
46. Zhou, M.; Li, J.-F.; Kita, T., Nanostructured AgPb<sub>m</sub>SbTe<sub>m+2</sub> System Bulk Materials with Enhanced Thermoelectric Performance. *J. Am. Chem. Soc.* **2008**, *130* (13), 4527-4532.
47. Harman, T. C.; Taylor, P. J.; Walsh, M. P.; LaForge, B. E., Quantum Dot Superlattice Thermoelectric Materials and Devices. *Science* **2002**, *297* (5590), 2229-2232.
48. Koh, Y. K.; Vineis, C. J.; Calawa, S. D.; Walsh, M. P.; Cahill, D. G., Lattice Thermal Conductivity of Nanostructured Thermoelectric Materials Based on PbTe. *Appl. Phys. Lett.* **2009**, *94* (15), 153101.
49. Hsu, K. F.; Loo, S.; Guo, F.; Chen, W.; Dyck, J. S.; Uher, C.; Hogan, T.; Polychroniadis, E. K.; Kanatzidis, M. G., Cubic AgPb<sub>m</sub>SbTe<sub>2+m</sub>: Bulk Thermoelectric Materials with High Figure of Merit. *Science* **2004**, *303* (5659), 818-821.
50. Wang, H.; Li, J.-F.; Nan, C.-W.; Zhou, M.; Liu, W.; Zhang, B.-P.; Kita, T., High-Performance Ag<sub>0.8</sub>Pb<sub>18+x</sub>SbTe<sub>20</sub> Thermoelectric Bulk Materials Fabricated by Mechanical Alloying and Spark Plasma Sintering. *Appl. Phys. Lett.* **2006**, *88* (9), 092104.

51. Poudeu, P. F. P.; D'Angelo, J.; Downey, A. D.; Short, J. L.; Hogan, T. P.; Kanatzidis, M. G., High Thermoelectric Figure of Merit and Nanostructuring in Bulk p-type  $\text{Na}_{1-x}\text{Pb}_m\text{Sb}_y\text{Te}_{m+2}$ . *Angew. Chem. Int. Ed.* **2006**, *45* (23), 3835-3839.
52. Kim, W.; Singer, S. L.; Majumdar, A.; Vashaee, D.; Bian, Z.; Shakouri, A.; Zeng, G.; Bowers, J. E.; Zide, J. M. O.; Gossard, A. C., Cross-Plane Lattice and Electronic Thermal Conductivities of ErAs:InGaAs/InGaAlAs Superlattices. *Appl. Phys. Lett.* **2006**, *88* (24), 242107.
53. Yan, Q.; Chen, H.; Zhou, W.; Hng, H. H.; Boey, Y. C.; Ma, J., A Simple Chemical Approach for PbTe Nanowires with Enhanced Thermoelectric Properties. *Chem. Mater.* **2008**, *20*, 6298-6300.
54. Tai, G.; Zhou, B.; Guo, W., Structural Characterization of Thermoelectric Transport Properties of Uniform Single-Crystalline Lead Telluride Nanowires. *J. Phys. Chem. C* **2008**, *112*, 11314-11318.
55. Urban, J. J.; Talapin, D. V.; Shevchenko, E. V.; Kagan, C. R.; Murray, C. B., Synergism in Binary Nanocrystal Superlattices Leads to Enhanced p-Type Conductivity in Self-Assembled PbTe/Ag<sub>2</sub>Te Thin Films. *Nat. Mater.* **2007**, *6*, 115-121.
56. Donega, C. d. M., Synthesis and Properties of Colloidal Heteronanocrystals. *Chemical Society Reviews* **2011**, *40* (3), 1512-1546.
57. Finney, E. E.; Finke, R. G., Nanocluster Nucleation and Growth Kinetic and Mechanistic Studies: A Review Emphasizing Transition-Metal Nanoclusters. *Journal of Colloid and Interface Science* **2008**, *317* (2), 351-374.
58. Bullen, C. R.; Mulvaney, P., Nucleation and Growth Kinetics of CdSe Nanocrystals in Octadecene. *Nano Letters* **2004**, *4* (12), 2303-2307.

59. Sowers, K. L.; Swartz, B.; Krauss, T. D., Chemical Mechanisms of Semiconductor Nanocrystal Synthesis. *Chem. Mater.* **2013**, *25* (8), 1351-1362.
60. Houtepen, A. J.; Koole, R.; Vanmaekelbergh, D.; Meeldijk, J.; Hickey, S. G., The Hidden Role of Acetate in the PbSe Nanocrystal Synthesis. *J. Am. Chem. Soc.* **2006**, *128*, 6792-6793.
61. Steckel, J. S.; Yen, B. K. H.; Oertel, D. C.; Bawendi, M. G., On the Mechanism of Lead Chalcogenide Nanocrystal Formation. *Journal of the American Chemical Society* **2006**, *128* (40), 13032-13033.
62. García-Rodríguez, R.; Liu, H., Mechanistic Study of the Synthesis of CdSe Nanocrystals: Release of Selenium. *Journal of the American Chemical Society* **2012**, *134* (3), 1400-1403.
63. Rawat, P. K.; Banerji, P., The Effect of Microstructure and Metal-Oxide Barriers on Carrier Transport in Top-Down Processed, Low Density Nanograined n-Type PbTe. *RSC Adv.* **2014**, *4*, 29818-29825.
64. Martin, J.; Nolas, G. S.; Zhang, W.; Chen, L., PbTe Nanocomposites Synthesized from PbTe Nanocrystals. *Appl. Phys. Lett.* **2007**, *90*, 222112-222112-3.
65. Faleev, S.; Léonard, F., Theory of Enhancement of Thermoelectric Properties of Materials with Nanoinclusions. *Phys. Rev. B* **2008**, *77*, 214304-214304-9.
66. Martin, J.; Wang, L.; Chen, L.; Nolas, G. S., Enhanced Seebeck Coefficient through Energy-Barrier Scattering in PbTe Nanocomposites. *Phys. Rev. B* **2009**, *79*, 115311-115311-5.
67. Zhang, H.; Hu, B.; Sun, L.; Hovden, R.; Wise, F. W.; Muller, D. A.; Robinson, R. D., Surfactant Ligand Removal and Rational Fabrication of Inorganically Connected Quantum Dots. *Nano Lett.* **2011**, *11*, 5356-5361.

68. Ning, Z.; Ren, Y.; Hoogland, S.; Voznyy, O.; Levina, L.; Stadler, P.; Lan, X.; Zhitomirsky, D.; Sargent, E. H., All-Inorganic Colloidal Quantum Dot Photovoltaics Employing Solution-Phase Halide Passivation. *Adv. Mater.* **2012**, *24*, 6295-6299.
69. Talapin, D. V.; Murray, C. B., PbSe Nanocrystal Solids for n- and p-Channel Thin Film Field-Effect Transistors. *Science* **2005**, *310*, 86-89.
70. Yao, J.; Takas, N. J.; Schliefert, M. L.; Paprocki, D. S.; Blanchard, P. E. R.; Gou, H.; Mar, A.; Exstrom, C. L.; Darveau, S. A.; Poudeu, P. F. P.; Aitken, J. A., Thermoelectric Properties of *p*-Type CuInSe<sub>2</sub> Chalcopyrites Enhanced by Introduction of Manganese. *Phys. Rev. B* **2011**, *84* (7), 075203-075203-10.
71. Burnett, J. D.; Gourdon, O.; Ranmohotti, K. G. S.; Takas, N. J.; Djieutedjeu, H.; Poudeu, P. F. P.; Aitken, J. A., Structure–Property Relationships along the Fe-Substituted CuInS<sub>2</sub> Series: Tuning of Thermoelectric and Magnetic Properties. *Mater. Chem. Phys.* **2014**, *147* (1–2), 17-27.
72. Moroz, N. A.; Olvera, A.; Willis, G. M.; Poudeu, P. F. P., Rapid Direct Conversion of Cu<sub>2-x</sub>Se to CuAgSe Nanoplatelets via Ion Exchange Reactions at Room Temperature. *Nanoscale* **2015**, *7* (21), 9452-9456.
73. Momma, K.; Izumi, F., VESTA 3 for Three-Dimensional Visualization of Crystal, Volumetric and Morphology Data. *J. Appl. Crystallogr.* **2011**, *44* (6), 1272-1276.
74. Lai, W.; Wang, Y.; Morelli, D. T.; Lu, X., From Bonding Asymmetry to Anharmonic Rattling in Cu<sub>12</sub>Sb<sub>4</sub>S<sub>13</sub> Tetrahedrites: When Lone-Pair Electrons Are Not So Lonely. *Adv. Funct. Mater.* **2015**, DOI: 10.1002/adfm.201500766.
75. Nielson, M. D.; Ozolins, V.; Heremans, J. P., Lone Pair Electrons Minimize Thermal Conductivity. *Energy Environ. Sci.* **2013**, *6*, 570-578.

76. Bouyrie, Y.; Candolfi, C.; Pailhes, S.; Koza, M. M.; Malaman, B.; Dauscher, A.; Tobola, J.; Boisron, O.; Saviot, L.; Lenoir, B., From Crystal to Glass-Like Thermal Conductivity in Crystalline Minerals. *Phys. Chem. Chem. Phys.* **2015**, *17* (30), 19751-19758.
77. Suekuni, K.; Tomizawa, Y.; Ozaki, T.; Koyano, M., Systematic Study of Electronic and Magnetic Properties for  $\text{Cu}_{12-x}\text{TM}_x\text{Sb}_4\text{S}_{13}$  ( $\text{TM} = \text{Mn, Fe, Co, Ni, and Zn}$ ) Tetrahedrite. *J. Appl. Phys.* **2014**, *115* (14), 143702-143702-5.
78. Bullett, D. W.; Dawson, W. G., Bonding Relationships in Some Ternary and Quaternary Phosphide and Tetrahedrite Structures:  $(\text{Ag}_6\text{M}_4\text{P}_{12})\text{M}_6'$ ,  $\text{Cu}_{12+x}\text{Sb}_4\text{S}_{13}$  and  $\text{Cu}_{14-x}\text{Sb}_4\text{S}_{13}$ ,  $\text{Ln}_6\text{Ni}_6\text{P}_{17}$ . *Journal of Physics C: Solid State Physics* **1986**, *19* (29), 5837.
79. Suekuni, K.; Tsuruta, K.; Ariga, T.; Koyano, M., Thermoelectric Properties of Mineral Tetrahedrites  $\text{Cu}_{10}\text{Tr}_2\text{Sb}_4\text{S}_{13}$  with Low Thermal Conductivity. *Appl. Phys. Express* **2012**, *5*, 051201-051201-3.
80. van Embden, J.; Latham, K.; Duffy, N. W.; Tachibana, Y., Near-Infrared Absorbing  $\text{Cu}_{12}\text{Sb}_4\text{S}_{13}$  and  $\text{Cu}_3\text{Sb}_4\text{S}_4$  Nanocrystals: Synthesis, Characterization, and Photoelectrochemistry. *Journal of the American Chemical Society* **2013**, *135* (31), 11562-11571.
81. Heo, J.; Laurita, G.; Muir, S.; Subramanian, M. A.; Keszler, D. A., Enhanced Thermoelectric Performance of Synthetic Tetrahedrites. *Chem. Mater.* **2014**, *26*, 2047-2051.
82. Lu, X.; Morelli, D. T.; Xia, Y.; Ozolins, V., Increasing the Thermoelectric Figure of Merit of Tetrahedrites by Co-Doping with Nickel and Zinc. *Chem. Mater.* **2015**, *27* (2), 408-413.
83. Lara-Curzio, E.; May, A. F.; Delaire, O.; McGuire, M. A.; Lu, X.; Liu, C.-Y.; Case, E. D.; Morelli, D. T., Low-temperature Heat Capacity and Localized Vibrational Modes in Natural and Synthetic Tetrahedrites. *J. Appl. Phys.* **2014**, *115* (19), 193515.

84. Barbier, T.; Lemoine, P.; Gascoin, S.; Lebedev, O. I.; Kaltzoglou, A.; Vaqueiro, P.; Powell, A. V.; Smith, R. I.; Guilmeau, E., Structural Stability of the Synthetic Thermoelectric Ternary and Nickel-Substituted Tetrahedrite Phases. *J. Alloys Compd.* **2015**, *634*, 253-262.
85. Chetty, R.; D. S, P. K.; Rogl, G.; Rogl, P.; Bauer, E.; Michor, H.; Suwas, S.; Puchegger, S.; Giester, G.; Mallik, R. C., Thermoelectric Properties of a Mn Substituted Synthetic Tetrahedrite. *Phys. Chem. Chem. Phys.* **2015**, *17* (3), 1716-1727.
86. Makovicky, E.; Forcher, K.; Lottermoser, W.; Amthauer, G., The Role of Fe<sup>2+</sup> and Fe<sup>3+</sup> in Synthetic Fe-Substituted Tetrahedrite. *Mineralogy and Petrology* **1990**, *43* (1), 73-81.
87. Morelli, D. T.; Lu, X.; Ozolins, V. Thermoelectric Materials Based on Tetrahedrite Structure for Thermoelectric Devices. WO2014008414A1, Jan 9, 2014.
88. Morelli, D. T.; Lu, X. Thermoelectric Materials Based on Tetrahedrite Structure for Thermoelectric Devices. WO2015003157A1, Jan 8, 2015.
89. Ramasamy, K.; Sims, H.; Butler, W. H.; Gupta, A., Selective Nanocrystal Synthesis and Calculated Electronic Structure of All Four Phases of Copper–Antimony–Sulfide. *Chem. Mater.* **2014**, *26*, 2891-2899.
90. Liu, Y.; Sahoo, P.; Makongo, J. P. A.; Zhou, X.; Kim, S.-J.; Chi, H.; Uher, C.; Pan, X.; Poudeu, P. F. P., Large Enhancements of Thermopower and Carrier Mobility in Quantum Dot Engineered Bulk Semiconductors. *J. Am. Chem. Soc.* **2013**, *135* (20), 7486-7495.
91. Lu, X.; Morelli, D. T., Rapid Synthesis of High-Performance Thermoelectric Materials Directly from Natural Mineral Tetrahedrite. *MRS Commun.* **2013**, *3*, 129-133.
92. Rowe, D. M., *Thermoelectric Handbook, Macro to Nano*. CRC Press: 2008.
93. West, A. R., *Basic Solid State Chemistry*. 2nd ed.; John Wiley & Sons Ltd.: New York, 1999.

94. Fultz, B.; Howe, J. M., *Transmission Electron Microscopy and Diffractometry of Materials*. Springer: 2002.
95. James, D.; Lu, X.; Nguyen, A. C.; Morelli, D.; Brock, S. L., Design of Lead Telluride Based Thermoelectric Materials through Incorporation of Lead Sulfide Inclusions or Ligand Stripping of Nanosized Building Blocks. *J. Phys. Chem. C* **2015**, *119* (9), 4635-4644.
96. Hines, M. A.; Scholes, G. D., Colloidal PbS Nanocrystals with Size-Tunable Near-Infrared Emission: Observation of Post-Synthesis Self-Narrowing of the Particle Size Distribution. *Adv. Mater.* **2003**, *15*, 1844-1849.
97. Cao, H.; Gong, Q.; Qian, X.; Wang, H.; Zai, J.; Zhu, Z., Synthesis of 3-D Hierarchical Dendrites of Lead Chalcogenides in Large Scale via Microwave-Assistant Method. *Cryst. Growth Des.* **2007**, *7*, 425-429.
98. Dong, G. H.; Zhu, Y. J., One-Step Microwave-Solvothermal Rapid Synthesis of Sb Doped PbTe/Ag<sub>2</sub>Te Core/Shell Composite Nanocubes. *Chem. Eng. J.* **2012**, *193-194*, 227-233.
99. James, D. J.; Lu, X.; Morelli, D. T.; Brock, S. L., Solvothermal Synthesis of Tetrahedrite: Speeding Up the Process of Thermoelectric Material Generation. *ACS Appl. Mater. Interfaces* **2015**, DOI: 10.1021/acsami.5b07141.
100. An, C.; Jin, Y.; Tang, K.; Qian, Y., Selective Synthesis and Characterization of Famatinite Nanofibers and Tetrahedrite Nanoflakes. *J. Mater. Chem.* **2003**, *13*, 301-303.
101. Inada, Y.; Ozutsumi, K.; Funahashi, S.; Soyama, S.; Kawashima, T.; Tanaka, M., Structure of Copper(II) Ethylenediamine Complexes in Aqueous and Neat Ethylenediamine Solutions and Solvent-Exchange Kinetics of the Copper(II) Ion in Ethylenediamine as Studied by EXAFS and NMR Methods. *Inorg. Chem.* **1993**, *32*, 3010-3014.

102. Wang, Z. D.; Yoshida, M.; George, B., Theoretical Study on the Thermal Decomposition of Thiourea. *Comput. Theor. Chem.* **2013**, *1017*, 91-98.
103. Biswas, K.; He, J.; Blum, I. D.; Wu, C.-I.; Hogan, T. P.; Seidman, D. N.; Dravid, V. P.; Kanatzidis, M. G., High-Performance Bulk Thermoelectrics with All-Scale Hierarchical Architectures. *Nature* **2012**, *489* (7416), 414-418.
104. Zhao, L.-D.; Lo, S.-H.; Zhang, Y.; Sun, H.; Tan, G.; Uher, C.; Wolverton, C.; Dravid, V. P.; Kanatzidis, M. G., Ultralow Thermal Conductivity and High Thermoelectric Figure of Merit in SnSe Crystals. *Nature* **2014**, *508* (7496), 373-377.

## ABSTRACT

### **NEW APPROACHES TO CHALCOGENIDE MATERIALS FOR THERMOELECTRICS: LEAD TELLURIDE-BASED NANOSTRUCTURES AND FACILE SYNTHESIS OF TETRAHEDRITE AND DOPED DERIVATIVES**

by

**DERAK JAMES**

**December 2015**

**Advisor:** Dr. Stephanie L. Brock

**Major:** Chemistry (Inorganic)

**Degree:** Doctor of Philosophy

The overall purpose of this work is to address several of the roadblocks to use of thermoelectric materials for generation of electricity, namely inefficient processing of materials and low performance, commonly rated by the figure of merit,  $ZT = T\alpha^2\sigma/\kappa_{tot}$ . The ZT includes  $\alpha$  as the Seebeck coefficient,  $\sigma$  as electrical resistivity,  $T$  as the average temperature, and  $\kappa_{tot}$  as total thermal conductivity.  $\kappa_{tot}$  is the sum of electronic charge carrier ( $\kappa_C$ ) and lattice ( $\kappa_L$ ) contributions to thermal conductivity. Attempts to increase ZT in the literature to values  $>1$  have focused on decreasing the thermal conductivity via nanostructuring or optimizing the electrical conductivity and Seebeck coefficient by doping. In this work, two separate approaches are taken toward improved thermoelectric materials: (1) Target higher ZT by assembling lead telluride (PbTe) nanoparticles from a multi-gram synthesis utilizing ligand stripping techniques or deliberately including discrete lead sulfide (PbS) NCs; (2) Develop a rapid, convenient synthesis of tetrahedrite ( $Cu_{12}Sb_4S_{13}$ ) and doped derivatives.

Approach (1): Nanostructuring of PbTe and PbTe–PbS. Nanostructured PbTe and nanocomposites of PbTe–PbS are hypothesized to increase ZT by lowering thermal conductivity,

while ligand stripping of PbTe NCs by sulfide or iodide is expected to increase ZT because it has been demonstrated to increase electrical conductivity in thin films of PbS. A new synthesis is in demand because mixing PbTe and PbS NCs requires that the PbTe be dispersible, and literature syntheses of such NCs suffer from small yields (<200 mg). Thus, applications of dispersible PbTe NCs are largely limited to thin films. The ZT values of these thin films are not reported due to difficulty in quantifying thermal conductivity. In the dissertation research, nanostructured PbTe pellets are prepared by hot-pressing PbTe NCs after either mixing with PbS NCs by incipient wetness, or ligand stripping with sulfide salt, iodide salt, or both. The PbTe NCs themselves are prepared in multi-gram quantities by hot-injection methods in solution. The NCs are characterized for crystallinity by powder X-ray Diffraction (XRD). The size and morphology of the NCs are probed via Transmission Electron Microscopy (TEM), and their composition is determined by Energy Dispersive Spectroscopy (EDS). The thermoelectric properties are studied on hot-pressed pellets of each sample. Samples demonstrate low thermal conductivity relative to the bulk due to the nanostructured PbTe, and sulfide-stripping resulted in in-situ growth of PbS. Incorporation of PbS results in a further decrease in thermal conductivity in both the mixture of pre-grown PbS and PbTe NCs and the sample of PbTe NCs that is ligand stripped with ammonium sulfide. However, ligand stripping with sulfide or iodide sources resulted in uncontrolled doping, leading to insulating behavior and low ZT values.

Approach (2): Developing a facile route to tetrahedrite and doped derivatives. Tetrahedrite is exciting the thermoelectric community due to its lack of rare or toxic elements, the tunability of its electronic properties by doping, the ability to dope by ball-milling with the plentiful natural mineral, and the ability to achieve a ZT of unity. However, the natural mineral is unsuitable on its own due to an excess of natural dopant, and reported tetrahedrite syntheses

require heating at high temperature (650 °C) in a three day process followed by two weeks of heating at 450 °C. This work establishes a new synthesis amenable to industrial production that reduces the heating time from over 2 weeks to 2 days for simultaneous batch production at moderate temperature (155 °C for one day and 430 °C for 30 min, cooling naturally). The tetrahedrite powder is prepared from chloride-free metal salts and thiourea by solvothermal methods and characterized by XRD for crystallinity. The composition is determined by Inductively Coupled Plasma analysis. Products from multiple batches are mixed by ball-milling alone or combined with the natural mineral as a means to dope with Zn<sup>2+</sup> as a solid solution. The resulting powder is then hot-pressed to pellet form for thermoelectric characterization. The tetrahedrite is also doped in-situ by zinc over a range of 0.79 to 1.40 mol equivalents using chloride-free metal salts. The in-situ doping, as opposed to doping by ball-milling, did not improve the ZT. However, the ZT of the new solvothermal tetrahedrite before doping mirrors that of the solid state material at high temperatures, and is improved by incorporation of zinc via ball-milling with the natural mineral. Thus, this project develops a rapid synthesis of tetrahedrite that could serve as an alternative to much slower solid state methods.

## AUTOBIOGRAPHICAL STATEMENT

DERAK JAMES

### **Education**

- **2010–2015 Ph.D.**, Chemistry, Wayne State University, Detroit, MI  
Thesis: “New Approaches to Chalcogenide Materials for Thermoelectrics: Lead Telluride-Based Nanostructures and Facile Synthesis of Tetrahedrite and Doped Derivatives.”  
Advisor: Dr. Stephanie L. Brock
- **2007–2009 M.S.**, Chemistry, Ball State University, Muncie, IN  
Thesis: “Synthesis and Photocatalytic Activity of the MoS<sub>2</sub> and WS<sub>2</sub> Nanoparticles in Degradation of Organic Compounds.”  
Advisor: Dr. Tykhon Zubkov
- **2002–2006 B.S.**, Chemistry, Minor in Physics, Purdue University, W. Lafayette, IN

### **Research and Teaching Experience**

- **8/2010-10/2015** Graduate Research/Teaching Assistant, Department of Chemistry, Wayne State University, Detroit, MI
- **8/2007-7/2009** Graduate Research Assistant, Department of Chemistry, Ball State University, Muncie, IN

### **Publications**

- “Solvothermal synthesis of tetrahedrite: speeding up the process of thermoelectric material generation.” James, D.; Lu, X.; Morelli, D.; Brock, S. L., *ACS Appl. Mater. Interfaces* **2015**, DOI: 10.1021/acsami.5b07141.
- “Design of lead telluride based thermoelectric materials through incorporation of lead sulfide inclusions or ligand stripping of nanosized building blocks.” James, D.; Lu, X.; Nguyen, A. C.; Brock, S. L.; Morelli, D., *J. Phys. Chem. C* **2015**, *119*, 4635–4644.
- “Photocatalytic properties of free and oxide-supported MoS<sub>2</sub> and WS<sub>2</sub> nanoparticles synthesized without surfactants.” James, D.; Zubkov, T., *J. Photochem. Photobiol. A* **2013**, *262*, 45–51.